

Ludwig-Maximilians-Universität München



FROM FAULTS
TO PLATE BOUNDARIES:
INSIGHTS FROM COMPUTER MODELS

Dissertation
zur Erlangung des Doktorgrades
der Fakultät für Geowissenschaften der
Ludwig-Maximilians-Universität München

vorgelegt von
Christoph Moder

am
7. 12. 2010

1. Gutachter: Prof. Dr. Hans-Peter Bunge

2. Gutachter: Prof. Dr. Anke Friedrich

Tag der mündlichen Prüfung: 18. 2. 2011

Contents

Contents	iii
List of Figures	v
Acknowledgments	vii
Introduction and Overview	1
1 Fault Physics and Computer Modeling	3
1.1 Theory of Fault Strength Versus Observations	3
1.2 Challenges for Experiments	6
1.3 Rheology of Non-Faulted Rock	7
1.3.1 Viscoelasticity	7
1.3.2 Nonlinear Mechanisms of Viscous Deformation	8
1.3.3 The Navier–Stokes Equation	13
1.3.4 Simplifications for High Viscosity	14
1.4 Rheology of Faults	15
2 SHELLS, a Neotectonic Fault Simulation Program	17
2.1 Technical Aspects	18
2.2 Computation of Fault Strength	21
2.3 Assumptions and Simplifications	22
2.4 Input Parameters	24
2.5 Output and Comparison with Observations	25
3 Case Studies	27
3.1 California: The Strength of Faults in the Crust in the Western United States	27
3.1.1 Abstract	27
3.1.2 Introduction	27
3.1.3 Models	29
3.1.4 Results	34
3.1.5 Implications for Fault Strength in California	39

3.1.6	Conclusions	42
3.2	Taiwan	54
3.2.1	Tectonic Setting	54
3.2.2	Model Setup	56
3.2.3	Heat Flow	57
3.2.4	Fault Strength	60
4	Plate Boundaries for Mantle Circulation Simulations	67
4.1	From Linear Features to Grid Point Velocities	68
4.1.1	Plate Reconstruction	68
4.1.2	The TERRA Grid	71
4.1.3	Plate Polygons and Grid Points	73
4.1.4	Performance Issues	76
4.2	Application: Mantle Circulation Model	78
4.2.1	Introduction	78
4.2.2	Computational Methods, Boundary and Initial Conditions	81
4.2.3	Results	85
4.2.4	Discussion	91
4.2.5	Conclusions	92
4.3	Effects of Plate Reconstructions on Mantle Circulation Simulations	96
A	Bibliography	99
B	Schematic Program Flow of SHELLS	117
C	Program Listings	129
C.1	Plate Polygons to TERRA Plate Maps	129
C.2	Wrapper Script	136

List of Figures

1.1	The San Andreas fault in the Carrizo plain	3
1.2	Faults and horizontal compressional stress directions in California	4
1.3	Calaveras Fault in Hollister, CA	5
1.4	Schematic sketch of Maxwell solid	8
1.5	Newtonian fluid: stress vs. strain rate	9
1.6	Creep regimes depending on stress and grain size	10
1.7	Dislocation creep in a 2D crystal lattice	11
1.8	Typical geotherm	12
1.9	Strength profile of crust and lithosphere	16
2.1	Global FEM grid, with local refinement in California.	19
2.2	FEM grid: continuum and fault elements	20
2.3	Upper limits for fault strength	22
3.1	Global grid with mantle convection velocities	30
3.2	Global grid with refinement in California	31
3.3	Local grid of California	33
3.4	Perspective view of SCEC Community Fault Model	34
3.5	Comparison of simulations	36
3.6	Effect of slip-dependent weakening on prediction errors	37
3.7	BDT depth for different fault strengths	40
3.8	Error tradeoff for different simulations	41
3.9	Map of individual fault slip-rates for two simulations	43
3.10	Diagram of observed fault slip-rates and simulations	44
3.11	Regional map of Taiwan	55
3.12	Schematic map of the Taiwanese detachment	56
3.13	Tectonic provinces of Taiwan	57
3.14	Grid of the Taiwan study area	58
3.15	Heat flow and crustal thickness in Taiwan	59
3.16	Plate boundary friction and global plate velocities	61
3.17	Maps of fault slip-rates for different simulations	63
3.18	Depths of the BDT for different simulations	64
3.19	Continuum strain rates for two models of Taiwan	66

4.1	Plate reconstruction tree	69
4.2	Reconstructed plate boundaries over 250 million years	70
4.3	GPlates screenshot	71
4.4	Icosahedral grid	72
4.5	Point-in-polygon algorithms	75
4.6	Plate polygons and TERRA grid	76
4.7	Comparison of S wave tomography models	79
4.8	3D temperature variations in mantle circulation model M2	86
4.9	S wave velocities of two mantle circulation models	88
4.10	Spectral power of heterogeneity in temperature and S wave velocity	90
4.11	Histograms of temperature variations in models M1–M4	93
4.12	Histograms of variations of S wave velocity in tomographic models	94
4.13	Comparison of two plate reconstructions	97

Acknowledgments

I would like to thank:

- My advisors Sara Carena and Hans-Peter Bunge, from whom I have learned a lot. Especially the importance of intuition and judging something for plausibility was new to me; they saw something in seconds that I did not notice in endless hours looking at the details. I'm also grateful for their patience and for encouraging me to know things deeply, instead of being "productive" in a merely superficial way.
- Deutsche Forschungsgemeinschaft (DFG) for funding this thesis with grant CA 691/1-1.
- The geophysics section for providing the computing infrastructure used in this thesis. Special thanks go to the administrator Jens Oeser; the reliability and convenience of the hardware and the Linux installation is outstanding. Furthermore, thanks to the people of Geocomputing and ObsPy for being an environment that supports the Unix philosophy and encourages the use of open source software.
- Bernhard Schuberth; working with him was sometimes quite magic, we complemented one another, and the result was more than the sum of our individual abilities.
- Dietmar Müller and his group (Grace Shephard, Aedon Talsma, Christian Heine) for the intensive and fruitful cooperation about plate reconstruction.
- All the other nice colleagues and guests at our institute.
- My roommates over the last years: Kerstin Reimer, Michael Wack, Sebastian Mühlbauer, Oliver Schlotterer and Niko Gorjup. It has been a very pleasant time with many interesting discussions, cooperation, meeting nice people, common activities, mutual tolerance . . . I don't remember any conflict at all during this time.
- Last but not least, all my friends (including the folks from the Liegeradstammtisch), and my family.

Introduction and Overview

The lithosphere is the mechanically rigid outer layer of the Earth that forms tectonic plates. Strain is largely concentrated at the faults, which are the most prominent surface evidence of the dynamic processes in the interior and thus one of the primary sources for observational data. Below, the lithosphere is coupled by viscous drag to the asthenosphere and hence to the large scale convective structures of the mantle.

The quantitative understanding of fault behavior at different scales is relevant for several reasons. At the scale of regional fault networks, a better knowledge of fault behavior and of actual values of parameters like fault friction translates into better evaluation of earthquake potential. At the global scale, where fault networks have fully developed into plate boundaries, the study of how these boundaries change over time can reveal important details about the physics of the mantle.

As more data become available, computer models are an effective way of handling these large amounts of information in order to test different hypotheses in an efficient manner. In this thesis, computer models are used to assess fault strength and crustal strength, and to study how models of mantle circulation are controlled by the geometry of the plate boundaries on the surface.

The strength of faults has been discussed for years, because there are several observations indicating a frictional strength one or two magnitudes lower than the canonical values of friction experiments in the laboratory ($\mu = 0.6 \dots 0.85$). However, faults are not isolated, but form interacting fault networks and depend also on the plastic deformation of the surrounding material; this has to be taken into account by the model. Chapter 1 gives a general introduction on the issue of fault strength and of the strength of the lithosphere, including limits for experiments and requirements for computer models. In chapter 2 the neotectonic simulation code SHELLS, which we used in our models, is illustrated.

Chapter 3 describes the investigation of fault strength in two study areas: California, as an example for a strike-slip environment, and Taiwan, as an example for a convergent setting. In both cases, we could use new high-resolution fault geometries derived from relocated earthquake hypocenters. This allows to represent the fault

interaction on a regional scale. The models of both study areas confirm the general weakness of faults, and that large faults (i.e. with large total slip) are presumably weaker than small ones. Another important result is that major faults must cross the whole lithosphere, in order to maintain a reasonable brittle–ductile transition depth.

A different aspect of faults is treated in chapter 4. Since the existence of faults is the consequence of plate motion and eventually the result of mantle convection, it is possible to link simulations of mantle circulation to tomography by imposing the plate motion history on the mantle velocity field. On this large scale, the evolution of the plate boundaries can be reconstructed over more than 200 Ma back in time.

The plate reconstructions that have been available in the past are coarse in time (with spacing in time between plate stages on the order of 10 Ma and more). This means, they had to be interpolated in order to get a smooth transition of the boundaries, which involved often laborious manual corrections.

Instead, the recent reconstructions are done with the software GPlates, so the boundaries can be output in arbitrary time steps. A mantle circulation model requires a surface velocity field that is derived from such a set of plate boundaries. Its computation is a technical challenge; the technique is described in detail in section 4.1. I have written a program that can efficiently convert plate boundaries into surface velocity fields that are ready to use with the mantle circulation software TERRA. This allows to run circulation models with different plate reconstructions and reference frames at any desired resolution, without requiring additional manual work. Section 4.2 shows an example of such a mantle circulation model with imposed plate boundaries.

Finally, chapter B in the appendix offers a verbal description of the operating mode of SHELLS, complementing the conceptual explanations in chapter 2, and chapter C contains the listings described in section 4.1.

1 Fault Physics and Computer Modeling

1.1 Theory of Fault Strength Versus Observations

The fundamental tenet of plate tectonics is the existence of a moving lithosphere. The lithosphere consists of rigid plates with the plastic deformation limited to plate boundaries, which are zones of strain localization. This allows crust to be preserved as coherent plates, in the case of buoyant continents for billions of years, and the preservation of the pattern of geomagnetic reversals in oceanic crust for more than a hundred million years.



Figure 1.1: The San Andreas fault in the Carrizo plain. (Photo by Moder, 2008)

Often, faults are clearly visible surface expressions of such localized deformation (fig. 1.1). Even their aseismic motion can sometimes be observed over human time scales. Yet, the exact mechanisms that govern fault strength remain elusive. An empirical estimate of rock strength is given by the work of *Byerlee* (1978), which determined a relationship between shear and normal stress based on a compilation

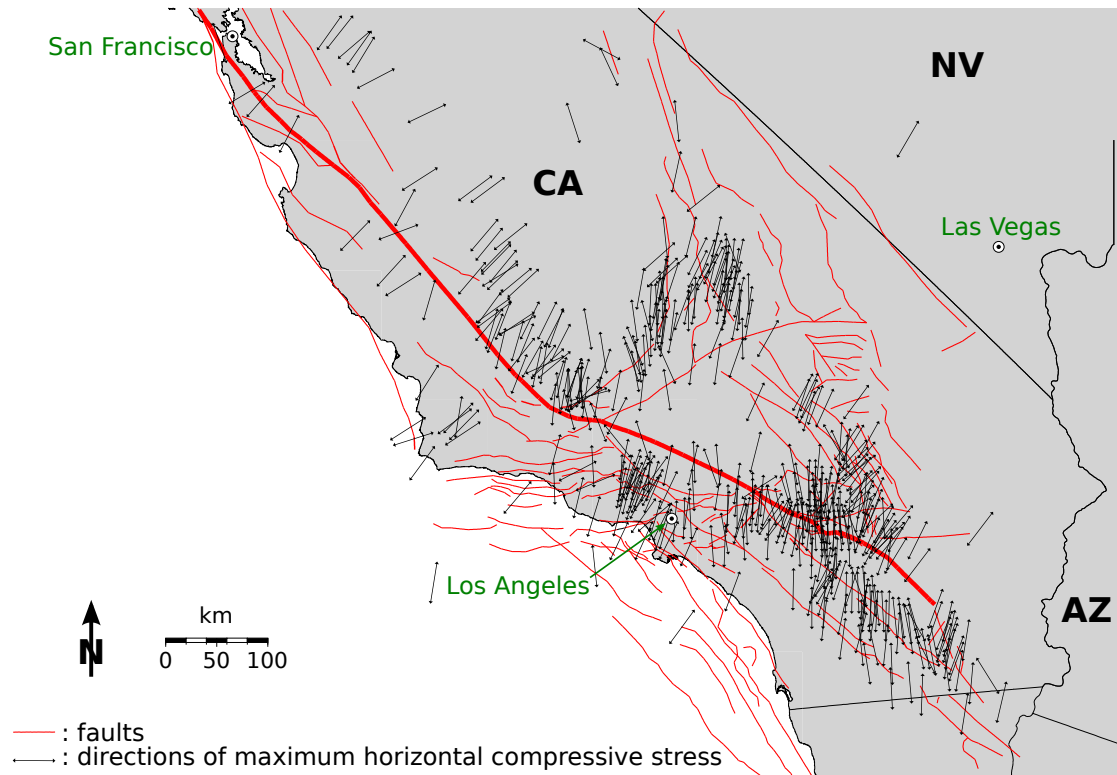


Figure 1.2: Southern California: The red lines are the active faults from the SCEC Community Fault Model (Plesch *et al.*, 2007), the San Andreas Fault is highlighted as a thick line. The black lines show the direction of the maximum horizontal compressive stress, from the World Stress Map 2008 (Heidbach *et al.*, 2008).

of data from civil engineering, mining engineering and geophysical literature. In these friction experiments, pairs of rock samples are pressed together, and the shear stress versus the compressive normal stress is measured. Whereas the data contain a high variability for small normal stresses (below 5 MPa, corresponding to depths of less than 150 m), Byerlee (1978) notes that for greater depths the ratio of rock shear strength to normal force is nearly independent of the rock type, surface roughness, and pressure, and can thus be described by two regression lines:

$$\tau = 0.85 \sigma_n \text{ for } \sigma_n \leq 200 \text{ MPa} \quad (1.1)$$

$$\tau = 0.5 + 0.6 \sigma_n \text{ for } \sigma_n > 200 \text{ MPa} \quad (1.2)$$

Byerlee's law seems convincing under laboratory conditions and explains the fact that faults cut through stratified rock units as if they were a homogeneous medium. But several observations contradict high friction in the brittle crust, at least for

major faults. First, the only sinks for the mechanical work done on the fault surfaces are seismic radiation and heat generation. The former can be estimated using the shear modulus of rock: the result is that the radiation of seismic energy can only consume a small part of the energy available during coseismic fault motion. The rest, one order of magnitude larger, must be dissipated as heat and would increase the surface heat flow significantly, once a state of equilibrium is reached. However, several studies on the San Andreas Fault (*Henye*, 1968; *Lachenbruch and Sass*, 1973), which is one of the most studied faults worldwide, could not find any significant heat flow anomaly around the fault.



Figure 1.3: The Calaveras fault in Hollister, CA; with a slip-rate of 15 ± 3 mm/a (*Working Group on California Earthquake Probabilities*, 1999), it is one of the major branches of the San Andreas fault system. (Photos by Moder, 2007)

Studies of the azimuths of the maximum horizontal principal compressive stress (S_{Hmax}) lead to a similar result. For the San Andreas Fault, investigations from *Mount and Suppe* (1987) and *Zoback et al.* (1987) show that the maximum horizontal principal stress is oriented nearly perpendicular to the San Andreas fault (fig. 1.2). High friction means strong coupling between the two sides of the fault. With S_{Hmax} at high angle to the fault itself, a strong coupling would prevent the fault from moving — which does not happen, as the San Andreas fault slips at a rate of several centimeters per year (fig. 1.3). A similar observation on a larger scale gives

the work of *Iaffaldano et al.* (2006) which relates the growth of the Andes with the velocity of the Nazca plate; any motion of this plate is only possible if the friction is very low (fig. 3.16). There are thus several questions that need to be answered:

- How strong is a fault, in absolute terms?
- What is an appropriate friction coefficient for faults?
- How strong are faults compared to their surroundings?
- How deep do faults reach?

1.2 Challenges for Experiments

In principle, these questions could be answered by different laboratory experiments. However, there are some issues that must be addressed. Faults interact with the adjacent rock, so the slip rate of a fault depends also on the plastic deformation of the surrounding crust. The question is not only whether isolated faults are weak or strong, but actually whether there are weak or strong faults in a weak or strong crust. Furthermore, plate boundaries are simple faults only to first-order. In reality, the deformation is much more diffuse, there are often several second-order faults next to the main plate boundary fault, especially where the latter is not straight (example: San Andreas Fault north of Los Angeles; fig. 1.2). Thus, for a self-consistent investigation, the complete fault system with its internal interactions must be modeled.

Moreover, a lab experiment suffers from inherent tradeoffs. An experiment with a viable duration (i.e. over human, not over geologic timescale) features strain rates that are much higher than the ones observed in nature. At the same time, experiments, due to their small scale, rapidly achieve a thermal equilibrium, whereas heat conduction in nature is much slower. The need of a realistic temperature profile forbids low strain rates in lab experiments. Thus, experiments may describe some aspects of lithospheric deformation correctly, but activate very different strain mechanisms (fig. 1.6).

A third problem arises from the inevitable model boundaries. Boundary conditions may act as driving forces; they influence the equilibrium of forces in the whole model domain, so appropriate boundary conditions are essential for any lithospheric model. However, the state of stress in the lithosphere cannot be examined directly. This means that there are significant uncertainties in the boundary forces and hence in the internal force balance.

These problems can be overcome by using computer simulations. Forward models of lithosphere motion allow arbitrary physical conditions such as realistic strain rates and heat profiles. It is also possible to implement a spherical geometry, which represents the curved geometry of large areas on Earth more accurately than planar box models. But the fundamental benefit of global spherical models is the closed surface. As the dominant deformation in the lithosphere occurs in the horizontal direction, and without any side boundary conditions thanks to the spherical geometry, a self-consistent model of the lithosphere is possible.

1.3 Rheology of Non-Faulted Rock

1.3.1 Viscoelasticity

Rock exhibits both elastic and plastic behavior. In a purely elastic body, the restoring force depends only on the amount of deflection from the position of rest, not on its rate. Thus, the body can always return to its previous shape, and the attainable deflection is independent of time. This allows abrupt deformations to propagate as seismic waves. On the other hand, the resisting force of a purely viscous body increases with the rate of deformation. This means that there is no position of rest, hence deformation is permanent. This allows material to be transported in a convective system through the whole mantle of the Earth, albeit very slowly. These two mechanisms may coexist, discriminated by deformation rate and magnitude of total deformation. If the deformation is small, there is little elastic resistance; and if the deformation occurs slowly, the viscous resistance is small. So, each of these two mechanisms dominates under the relevant conditions (fig. 1.4).

In general, elasticity and viscosity are nonlinear properties. But for small ranges of strain and strain rates, they can be approximated as piecewise linear and expressed by constants. A linearly elastic body is then described by *Hooke's law*, the elasticity is expressed by the stiffness tensor or, in the isotropic case, by bulk and shear modulus. Linearly viscous behavior is described by a so-called *Newtonian fluid* (fig. 1.5).

The characteristic duration that discriminates between elastic and viscous behavior is called *Maxwell time*; it is defined as the ratio of viscosity η and shear modulus G , and denotes the duration of the decay of an elastic deformation to $1/e$:

$$t = \frac{\eta}{G} \quad (1.3)$$

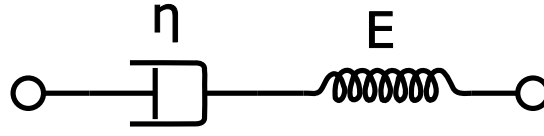


Figure 1.4: Maxwell solid as an example for viscoelastic behavior. Fast deflections are taken up by the elastic spring, whereas the slow viscous dashpot can accommodate larger deformations. (From *Pekaje, 2007.*)

The shear modulus of rock is on the order of 10 GPa; laboratory experiments of dry Westerly granite yield $G = 18$ GPa (*Heard et al., 1974*). In contrast, viscosity is heavily temperature-dependent and thus more variable. For the upper mantle, it can be inferred from models of post-glacial rebound; the canonical value of *Mitrovica (1996)* is 10^{21} Pa s. These two values would result in a Maxwell time of 2000 years. The upper crust is stiffer: for example, *Bird et al. (2008)* assume 8×10^{24} Pa s as an upper limit for viscosity (which corresponds to a Maxwell time on the order of 10 Ma). However, due to the nonlinear temperature dependence of ductile deformation processes, most of the lithosphere has a much lower viscosity, and its ductile character renders the elastic component of the uppermost layer insignificant. Thus, assuming a dominant viscosity of 5×10^{21} Pa s, the overall rheology of the lithosphere over times of 10,000 years can be described by a highly viscous fluid.

1.3.2 Nonlinear Mechanisms of Viscous Deformation

The ductile behavior of rocks originates from several different mechanisms that allow a solid material to deform at temperatures far below the melting point. In these mechanisms, the bulk lattice remains always intact, whereas atoms, vacancies, grain boundaries or other lattice defects migrate through the crystal lattice. These creep mechanisms dominate in different ranges of temperature, strain rate and grain size (fig. 1.6). But they all have in common a strong sensitivity on temperature. Thermal energy counteracts the binding energy of the atoms in the crystal lattice, thus all creep mechanisms can be described by Arrhenius-type equations (*Laidler, 1984*) that contain an exponential dependence on temperature:

$$k = A e^{-Q/RT} \quad (1.4)$$

where Q = activation energy, R = gas constant, T = temperature, A = prefactor, k = reaction rate.

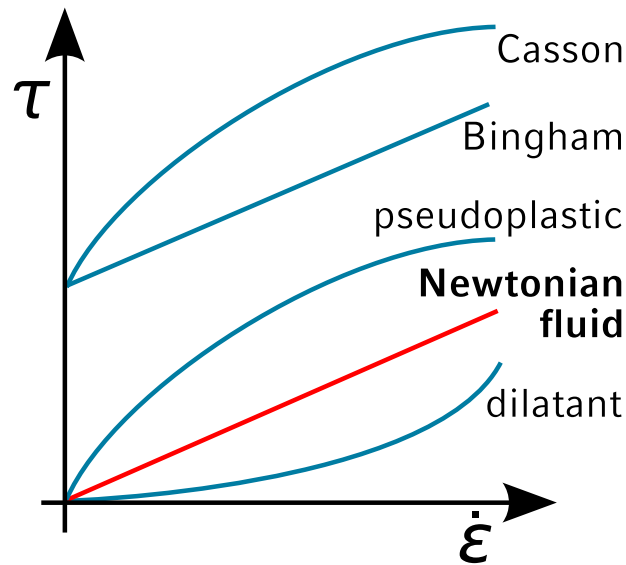


Figure 1.5: Newtonian fluid: shear stress τ is proportional to strain rate, the slope is the viscosity η . In contrast, the shear stress of dilatant and pseudoplastic fluids is not proportional to the strain rate; a dilatant fluid such as Silly Putty exhibits shear thickening, and a pseudoplastic fluid such as ketchup exhibits shear thinning. A Bingham fluid such as toothpaste behaves like a rigid body for low stresses, but becomes a viscous fluid if the yield stress is exceeded. (Figure derived from *Kolossos*, 2005.)

The term *diffusion creep* summarizes all mechanisms that involve the motion of atoms and vacancies through the crystal lattice. In order to move an atom, its binding energy must be overcome. So these mechanisms act preferentially at high homologous temperatures, i.e. close to the melting temperature. The motion through the bulk lattice is called *bulk diffusion* or *Nabarro-Herring creep*; it requires a high amount of activation energy to free the atoms in the lattice. In contrast, the binding energy at grain boundaries is lower, so it requires less energy to remove atoms on the grain sides with high stress and deposit them on the sides where the stress is low. This is called *Coble creep* or, if a fluid is involved in the dissolution and deposition of the ions, *pressure solution*; these mechanisms are more efficient at small grain sizes, since there are more grain boundaries along which the atoms can move.

Much less energy is required to shift an atomic bond from one atom to the next one, instead of breaking all bonds and moving an atom. This is called *dislocation creep*; a lattice dislocation can move through a crystal in the same manner as a wrinkle through a carpet (fig. 1.7). The atoms move only from one lattice site to the next one, so this mechanism is quite slow compared to diffusion creep, but can

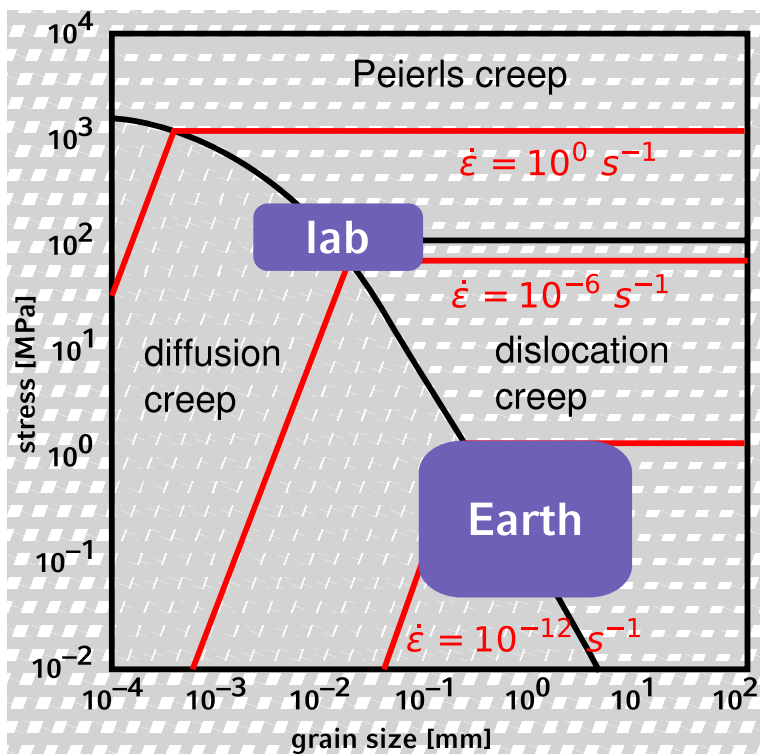


Figure 1.6: Creep mechanisms depending on stress and grain size. The stresses, grain sizes and strain rates that prevail in lab experiments versus in the Earth differ by many magnitudes, thus very different creep mechanisms are activated. Note that for diffusion creep (more precisely: Coble creep), the strain rate depends also on grain size. (After Karato, 2010.)

act at a much lower temperature.

Related to dislocation creep is *dislocation climb*; however, edge dislocations move out of the slip plane — for dislocation creep, the Burgers vector lies within the slip plane. This gives a higher degree of freedom in the direction of motion, but requires more energy, making dislocation climb more temperature-dependent than dislocation creep.

Due to the statistical nature of temperature, all these mechanisms act simultaneously; the dominant one is determined by the governing conditions of temperature, strain rate and grain size. In the lithosphere, where the homologous temperature is low (fig. 1.8), the strain rates are small and the grain size can be rather large, dislocation creep is assumed to be the dominant mechanism. Due to the exponential decay of rock strength with temperature, the overall strength of the lithosphere is controlled by low-temperature creep processes. Other mechanisms may play a

significant role in regions of high temperature, but they contribute only marginally to the total strength of the lithosphere and can thus be neglected.

Unfortunately, dislocation creep is not sufficiently well understood (e.g., *Hull and Bacon*, 1984). Whereas solid-state theory covers other deformation mechanisms such as diffusion creep or pressure solution (e.g., *Poirier*, 1985), the mathematical description of dislocation creep is more an empirical approximation than the description of the governing physics (e.g., *Brace and Kohlstedt*, 1980; *Rutter and Brodie*, 1991).

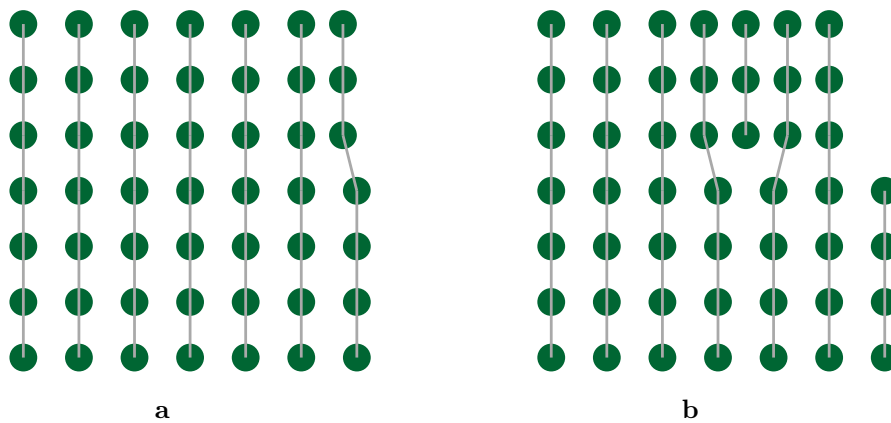


Figure 1.7: Dislocation creep: Two snapshots of a dislocation that propagates from right to left through a 2D lattice. Like moving a wrinkle through a carpet, this requires much less energy than breaking the whole crystal (= moving the whole carpet at once) (*Bulatov*, 2008).

A difficulty arises from the fact that dislocation creep is strongly rock-type dependent (grain size, macro- and microstructure; e.g., *Kirby and Kronenberg*, 1987). Contrary to Coulomb friction, where one friction coefficient seems to match most rocks quite well, it is not possible to determine experimental creep parameters that are valid for all rocks. Furthermore, ductile behavior nonlinearly depends on strain rate and thus on the timescale of the deformation process. Laboratory experiments are conducted on human timescale (5–10 years), their results are then extrapolated to a geological timescale ($> 10^6$ years). This extreme extrapolation may not be appropriate, as different creep mechanisms may be dominant in different scales of strain rate.

Thus, it is only possible to assume an average dislocation creep behavior, that is chosen such that it fits geologic observations — but without any physical background. For example *Bird and Kong* (1994) have chosen the dislocation creep parameters A (shear stress coefficient) and Q (dislocation creep activation energy)

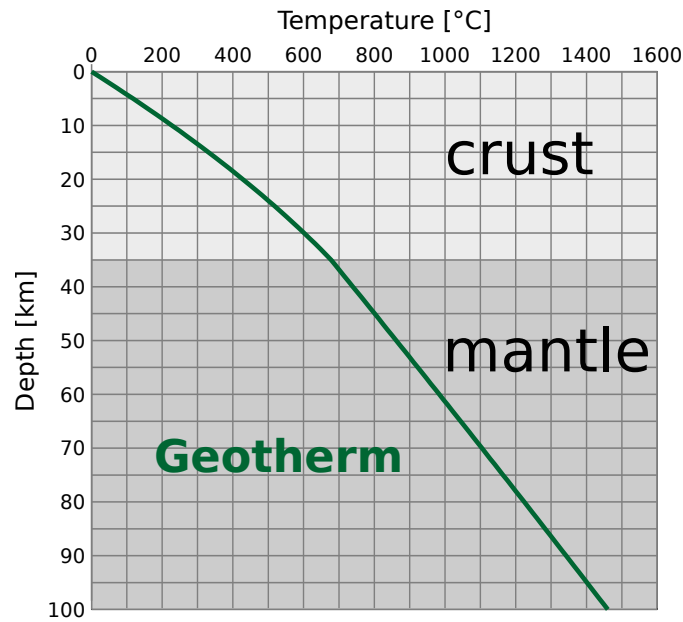


Figure 1.8: Typical geotherm for a 35 km thick crust with a surface temperature of 0 °C, surface heat flow of 65 mW/m² (Pollack *et al.*, 1993), purely conductive heat transfer, and other average parameters (crust: thermal conductivity 2.7 W/(m K), radiogenic heat 0.727 μW/m³; mantle: thermal conductivity 3.2 W/(m K), radiogenic heat 0.032 μW/m³). Although partial melt begins only in the mantle (e.g. solidus temperature for peridotite: ca. 800 °C), ductile deformation due to dislocation creep becomes significant at much lower temperatures.

such that the computed brittle–ductile transition depth matches the observed maximum earthquake depth in California. This yields an effective viscosity η which is dependent on temperature T , pressure p and some other parameters ($\dot{\epsilon}$: strain rate; R : gas constant; A and Q : creep constants; n : stress exponent):

$$\eta(T, p, \dots) = \dot{\epsilon}^{d(1-n)/n} A^{-1/n} \exp\left(-\frac{Q + pV}{nRT}\right) \quad (1.5)$$

This leads to a nonlinear stress–strain rate relation:

$$\sigma = \eta(T, p, \dot{\epsilon}) \cdot \dot{\epsilon} \quad (1.6)$$

The stress–strain rate relation is a smooth function, so it can be approximated as piecewise linear. The viscosity is then constant for a small range of temperatures and strain rates. If the computation is done iteratively, the viscosity can thus be assumed to be constant within an iteration and adjusted between the iterations.

This means that the lithosphere is during an iteration assumed to be a Newtonian fluid.

1.3.3 The Navier–Stokes Equation

The behavior of Newtonian fluids can be modeled using the *Navier–Stokes equation*, which states that the conservation of momentum is an equilibrium of driving, accelerating and resisting forces:

$$\rho \frac{D\mathbf{v}}{Dt} = \nabla \cdot \boldsymbol{\sigma} + \mathbf{f} \quad (1.7)$$

On the left hand side is mass (per unit volume) ρ times acceleration, on the right hand side the divergence of stress $\nabla \cdot \boldsymbol{\sigma}$ and other driving/resisting forces \mathbf{f} . The acceleration can be split into a time-dependent and a convective part, using the advection operator $\mathbf{v} \cdot \nabla$. Furthermore, the stress tensor $\boldsymbol{\sigma}$ can be split into a compressive (volume changes) and a deviatoric part (shape changes). Due to isotropy, the former can be written as pressure p , and the latter can be expressed using viscosity η and velocity gradient $\nabla \mathbf{v}$. This yields:

$$\overbrace{\rho \left(\frac{\partial \mathbf{v}}{\partial t} + \mathbf{v} \cdot \nabla \mathbf{v} \right)}^{\text{inertia}} = \underbrace{-\nabla p}_{\text{pressure gradient}} + \underbrace{\eta \nabla^2 \mathbf{v}}_{\text{viscous resistance}} + \underbrace{\mathbf{f}}_{\text{driving forces}} \quad (1.8)$$

A second condition besides the equation of motion is the conservation of mass, according to which temporal density variations must equal the mass flux through the boundaries. This is described by the *continuity equation*:

$$\frac{\partial \rho}{\partial t} + \nabla \cdot (\rho \mathbf{v}) = 0 \quad (1.9)$$

For incompressible fluids ($\rho = \text{const}$), the density does not vary, so its derivatives vanish:

$$\nabla \cdot \mathbf{v} = 0 \quad (1.10)$$

Besides conservation of momentum (Navier–Stokes equation) and mass (continuity equation), the conservation of energy must also be taken into account in a fluid

mechanical simulation. This is done by the *heat equation* that relates changes of temperature T over time t to heat conduction (influenced by thermal conductivity k , specific heat capacity c_p and density ρ) and internal heat sources or sinks q :

$$\underbrace{\frac{\partial T(\mathbf{x}, t)}{\partial t}}_{\substack{\text{temperature} \\ \text{variation} \\ \text{with time}}} = \frac{k}{c_p \rho} \underbrace{\Delta T(\mathbf{x}, t)}_{\substack{\text{heat} \\ \text{conduction}}} - \underbrace{\mathbf{v} \cdot \nabla T(\mathbf{x}, t)}_{\substack{\text{heat} \\ \text{advection}}} + \underbrace{q(\mathbf{x}, t)}_{\substack{\text{heat} \\ \text{sources}}} \quad (1.11)$$

1.3.4 Simplifications for High Viscosity

The slow creeping flow of the lithosphere is characterized by the absence of turbulence, which allows a considerable simplification of the Navier–Stokes equation. This can be justified by comparing the magnitudes of the involved forces.

The right hand side of the Navier–Stokes equation is dominated by the viscous term:

- The highest pressure gradient is found in orogens; a mountain with a height of 8000 m causes over a horizontal distance of 15 km a horizontal pressure gradient of 16 kPa/m, i.e. the first summand is at most on the order of 10^5 .
- The typical velocity difference between mantle and crust is on the order of cm per year ($= 10^{-10} \text{ m s}^{-1}$), over a typical depth range of 100 km; multiplied with a typical viscosity of 10^{21} Pa s it gives an order of magnitude of 10^6 .

The left hand side is much smaller:

- Density: it is on the order of 10^3 kg m^{-3}
- Acceleration: As an example, the velocity of the Indian plate changed between 50 and 35 Ma from 15 cm/yr to 4 cm/yr; this gives an acceleration on the order of $10^{-16} \text{ m s}^{-1}$.
- Convective acceleration: The product of plate velocities is in the order of $10^{-18} \text{ m s}^{-1}$, with the velocity gradient it is even smaller.

Thus, the right hand side of the Navier–Stokes equation, which describes the driving and resisting forces, is about 20 magnitudes larger than the left hand side, which contains the accelerating forces. So, the latter can easily be omitted and the fluid is assumed to have no inertia. The result is called the *Stokes equation*.

In general, the presence of inertia means that a significant amount of energy can be stored temporarily as kinetic energy. This decouples the driving and resisting

forces, and kinetic energy acts as a buffer. A system without inertia is accordingly characterised by a direct equilibrium of driving and resisting forces. The time derivative in the inertial term of the Navier–Stokes equation disappears in the Stokes equation; this means that the equilibrium of forces is instantaneous.

This has direct consequences for the significance of boundaries. Normally, boundary forces can be neglected for sufficiently short time intervals, because their influence propagates through the model. But without inertia, boundary forces gain far-field character: Being part of the global force balance, they affect instantaneously the whole model. Thus, boundary conditions must be chosen carefully in systems without inertia.

1.4 Rheology of Faults

Faults are velocity discontinuities, so they cannot be described by the smooth velocity field of a Newtonian fluid like the adjacent continuum. The friction in the upper brittle part of a fault is described by the *Coulomb fracture criterion*:

$$\sigma_s = \mu \cdot (\sigma_n - p_f) = \mu^* \cdot \sigma_n, \quad (1.12)$$

This means that the shear stress σ_s is proportional to the normal stress σ_n less the pore fluid pressure p_f . The constant of proportionality is the friction coefficient μ . As it is often impossible to determine p_f independently at the scale of crustal problems (local determinations exist only in areas of oil exploration), it is more appropriate to choose μ^* (effective friction coefficient) for studies involving faults at lithospheric scale. In the absence of pore fluids, $\mu = \mu^*$.

Whereas Coulomb friction, and therefore shear strength, increases with depth, ductile deformation becomes easier with depth due to the increasing temperature. Where the curves of brittle and ductile shear strength intersect, the dominant mechanism changes from brittle to ductile (fig. 1.9). At this *brittle–ductile transition depth* (BDT), the shear strength of the fault reaches a maximum. Also the total fault strength, being the vertical integral of strength over depth, has its maximum around the BDT depth, whereas unfaulked crust is strongest on top. There can be more than one such intersection, even for a homogeneous fault surface with constant dip angle.

Unlike brittle friction, ductile behavior depends strongly on the composition of the material, so there are at least two exponential curves, one describing the dislocation creep strength in the crust and the other in the mantle lithosphere. More changes

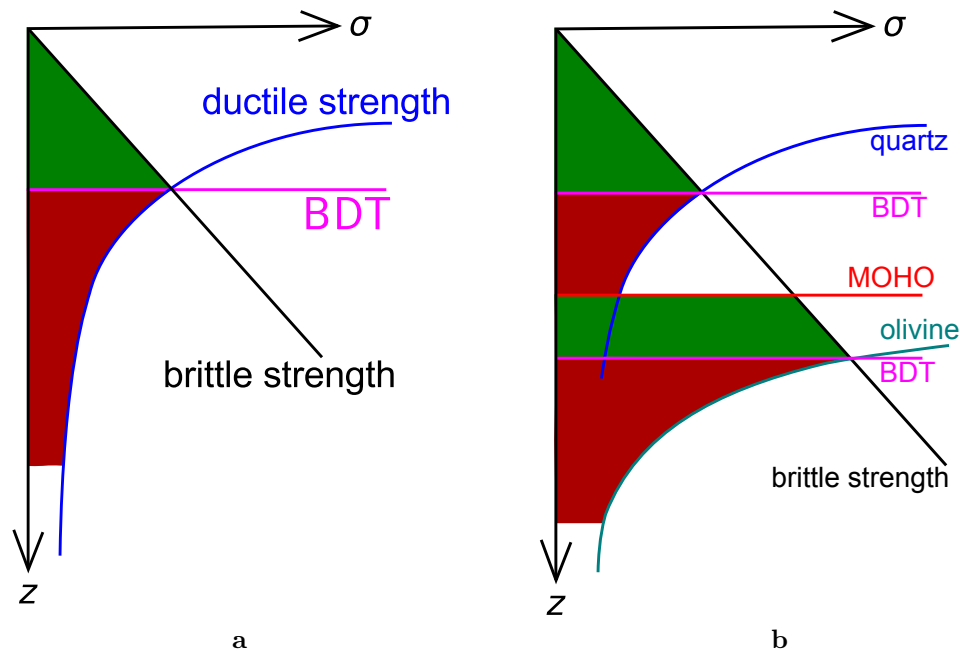


Figure 1.9: Schematic strength profile. **a:** Strength of the crust, with brittle friction in the upper part (below strength limit for plastic deformation) and power-law creep below. **b:** Strength profile of the whole lithosphere. The mantle has a different composition, so the power-law creep is different, but the brittle friction is virtually identical. This can lead to two brittle–ductile transitions within the lithosphere.

in composition, e.g. thick sedimentary layers, can lead to additional BDTs. The result is a strength diagram similar to the one in fig. 1.9 b, with alternating sections of linear increase and exponential decrease of shear strength, leading to a shape that is sometimes compared to a Christmas tree or a sail boat.

Since the major contributions to total fault strength come from the material around the BDT depth, having the correct BDT depth is crucial when computing the total fault strength. A possible indicator for the BDT depth in the crust is seismicity. The build-up of seismic stress is not possible in a purely ductile regime, so in most tectonic settings the depth of the deepest earthquakes can tell where the brittle behavior ends. Unfortunately, the BDT depth alone is an ambiguous criterion for fault strength, since different combinations of strength in both the brittle and ductile part can lead to identical BDT depths. Thus, a combined investigation of fault strength in both brittle and ductile realms is necessary, and it must be performed simultaneously with BDT depth determinations.

2 SHELLS, a Neotectonic Fault Simulation Program

In general, a model of the temporal development of a convective system like the Earth requires a coupled system of equations: The equation of motion must be solved together with the heat equation and the continuity equation. Such a model could be used to reproduce the past development of the lithosphere, or to predict its future evolution. However, our available data of the lithosphere are the limiting factor: We can observe its current state, but we know much less about the lithosphere in the distant past. This lack of initial condition information prohibits a reproduction of the present-day fault configuration. At the same time, it is also of little use to predict faulting in the future: The initial conditions are available (the present-day state). But our model makes predictions on timescales beyond the Maxwell time, and therefore it is not possible to test observationally. These fundamental problems limit the value of a simulation of the temporal evolution of the lithosphere.

However, one can make assertions about the current status of the lithosphere. It is possible to use a model of the present-day lithosphere and compute the balance of forces. Without any development in time, the energy equation can be omitted; only the equation of motion remains. As we know from section 1.3.4, inertia can be neglected in the lithosphere, so the equation that has to be solved is the *Stokes equation*:

$$\underbrace{\nabla p}_{\text{pressure gradient}} - \underbrace{\mathbf{f}}_{\text{other driving forces}} = \underbrace{\eta \nabla^2 \mathbf{v}}_{\text{resisting viscous forces}} \quad (2.1)$$

An implementation of this approach is the program SHELLS (*Bird and Kong, 1994*). It is a finite element program written for the numerical forward-modeling of faulted lithosphere on a spherical grid. The rigid plate motions serve usually as driving forces; the scope of application is accordingly regional or global. On these scales, the typical vertical extensions and velocities are small compared to

the corresponding horizontal dimensions, so only the latter are considered. In order to accomplish this, the lithosphere strength is integrated in the vertical direction and further computations are then performed in 2D. This approach is termed *thin-shell approximation*; it reduces the computational costs and allows a higher grid resolution.

SHELLS cannot determine the fault geometry by itself; the fault network must be given as an input. This is the consequence of the governing physics: Faults are places where the material has been weakened due to deformation — this means that fault formation processes involve positive feedback. As we have seen in section 1.3.2, the deformation of unfaulted material due to creep processes is nonlinear and not well understood. Furthermore, small deviations on the sub-grain size scale lead to stress peaks that facilitate the rupture propagation and finally the formation of large faults. Additional complications are the heterogeneity of the lithosphere and the presence of pre-existing faults. All this makes fault formation an inherently chaotic process. Thus, a model of the temporal development of faults is not only a very demanding in terms of the physical description, but it also cannot provide any additional predictions that can be tested.

2.1 Technical Aspects

The computation is performed on an irregular spherical grid (fig. 2.1), made of triangular continuum elements and linear fault elements. The size and aspect ratio of the continuum elements is arbitrary, but in favor of a good interpolation of the nodal properties within the grid, equilateral triangles are recommended. Thus, a good basis for a spherical grid is a subdivision of the icosahedron (see section 4.1.2 and fig. 4.4), with local modifications and refinements in order to match faults by element boundaries.

A fault is represented by a chain of linear fault elements; these are located between adjacent continuum elements. Each fault element consists of four nodes: two collocated nodes at each endpoint (fig. 2.2). This node doubling is necessary in order to allow a velocity discontinuity — the two triangular continuum elements on both sides of the fault element can then move in different directions, without being connected by shared nodes. Only at fault endpoints, the two endpoint nodes point to the same grid node; the fault cannot have any motion on that end, since one node cannot move in two different directions simultaneously. This is consistent with nature, given that offset and slip rate must go to zero where a fault ceases to exist. Thus, a fault must be composed of at least two fault elements to be able to slip and to even exist as a fault.

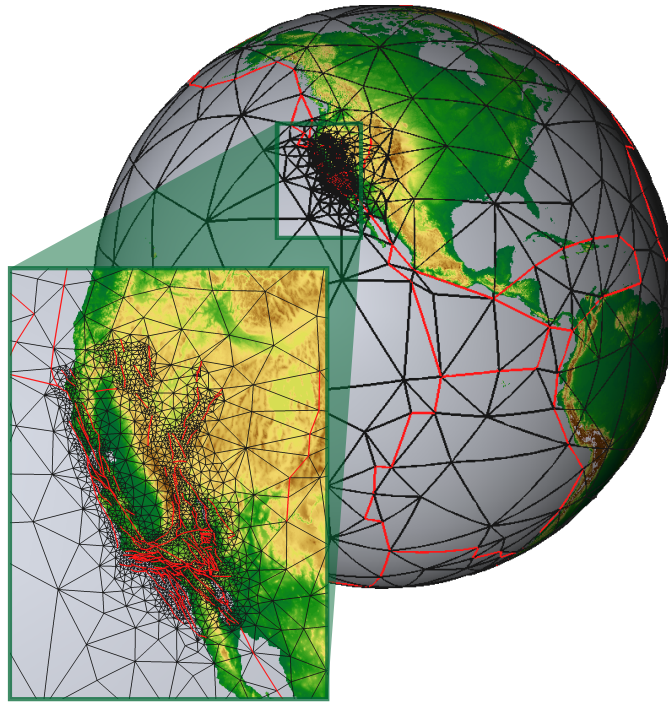


Figure 2.1: Global FEM grid, with local refinement in California.

The simulation is done in an iterative way: Since the driving force depends on the velocity difference between the lithosphere and the driving velocity field in the mantle, there exists a feedback between the input and the output of the computation. Also the ductile fault strength and the strength of the continuum depend on the strain rate, but influence the output velocity field as well. Thus, the computation is repeated several times (typically around 50 times), whereupon the system approaches a state of equilibrium, and stopped when the difference between two successive cycles becomes sufficiently small. Convergence is in principle not guaranteed; however, a damping term in the viscosity restricts its reaction to a changing strain rate, so the differences between iteration cycles remain small — which prevents chaotic oscillations in most cases, at least for a sufficiently stiff lithosphere.

The computation of the stiffness matrix and the forcing vector are performed on seven equally distributed Gauss integration points per continuum element or fault element. The model velocities are stored at the grid nodes. In each iteration cycle, these values are interpolated onto the integration points, and afterwards projected back onto the nodes; this is done using linear nodal functions, which serve as both basis and test functions. There are six nodal functions per continuum element (for two velocity components at each triangle vertex) and four nodal functions per fault

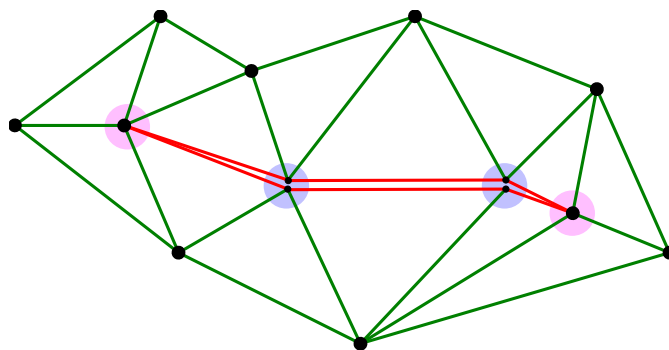


Figure 2.2: Continuum elements (green) and fault elements (red) in the finite element grid. The fault consists of three fault elements; only the two fault nodes in the middle (blue shaded) can move, the fault endpoints (pink shaded) have to stay fixed. Thus, only the middle fault segment has four different nodes; on the other two fault segments, the endpoints on one side point to the same grid node. (The doubled endpoint nodes have the same coordinates; here, they are drawn side-by-side for clarity.)

element (two velocity components at each endpoint of the fault element); the two sides of the fault are identical, so the same nodal function can be used for both of them. Since the grid is spherical, the nodal functions differ from those used for flat triangular meshes; continuum elements are spherical triangles, and fault elements are great circle arcs. (The detailed formulas are given in *Kong and Bird, 1995*.)

At every grid node, the equilibrium of driving and viscous resisting forces is computed. This leads to a large linear system of equations that is expressed as a matrix equation:

$$\mathbf{K} \mathbf{x} = \mathbf{f} \tag{2.2}$$

\mathbf{K} is the stiffness matrix, \mathbf{f} is the forcing vector, and \mathbf{x} is the velocity solution vector. The stiffness matrix contains the connections between all grid nodes, so its size is in principle the square of the number of grid nodes times the two degrees of freedom (= two velocity components). Since most grid nodes do not have a direct connection, the stiffness matrix entry is 0, i.e. \mathbf{K} is a sparse matrix. In order to save memory, the stiffness matrix is assembled using a band storage scheme. The bandwidth of a matrix, being the maximum distance from the main diagonal, depends on the order of the elements; so a reduced bandwidth leads to lower memory consumption and a faster computation. The auxiliary program *OrbNumber* can be used to reduce the bandwidth by renumbering the grid nodes; it uses the Cuthill–McKee algorithm (*Cuthill and McKee, 1969*) to optimize the connectivity.

A direct solver from a numerical library is used to solve the linear system. By default, SHELLS uses the routine DLSLRB from the IMSL library; in the absence of this commercial library, we are using the routine DGBSV from the open source LAPACK library. It uses LU decomposition to solve the matrix equation.

2.2 Computation of Fault Strength

As we have noticed before, fault strength is controlled by brittle friction and ductile deformation. This would allow nearly infinite fault strength, so SHELLS defines upper limits for shear stress and viscosity. This means that SHELLS examines four mechanisms of fault strength; the strength of a fault at a certain depth corresponds to the weakest of these four mechanisms (fig. 2.3):

- brittle friction
- power-law creep
- plastic deformation, for high stresses
- Newtonian viscous flow, with a bounded viscosity

Brittle strength increases linearly with depth; the proportionality factor is the effective friction coefficient μ^* :

$$\sigma_s = \mu \cdot (\sigma_n - p_f) = \mu^* \cdot \sigma_n \quad (2.3)$$

Plastic deformation sets an upper limit of shear stress that a rock can sustain; above it, arbitrary amounts of deformation occur, regardless of temperature and pressure:

$$\sigma_{s,\max} = \text{const} \quad (2.4)$$

Power-law creep is an empirical law describing the migration of lattice dislocations. It depends exponentially on temperature, so with a positive geotherm, rock strength due to creep decreases exponentially with depth:

$$\sigma_c = \left[2A \left(2\sqrt{-\dot{\epsilon}_1\dot{\epsilon}_2 - \dot{\epsilon}_2\dot{\epsilon}_3 - \dot{\epsilon}_3\dot{\epsilon}_1} \right)^{(1-n)/n} \exp\left(\frac{B + Cz}{T}\right) \right] \dot{\epsilon}$$

Finally, there is also an upper limit of viscosity of the creeping layer for Newtonian flow:

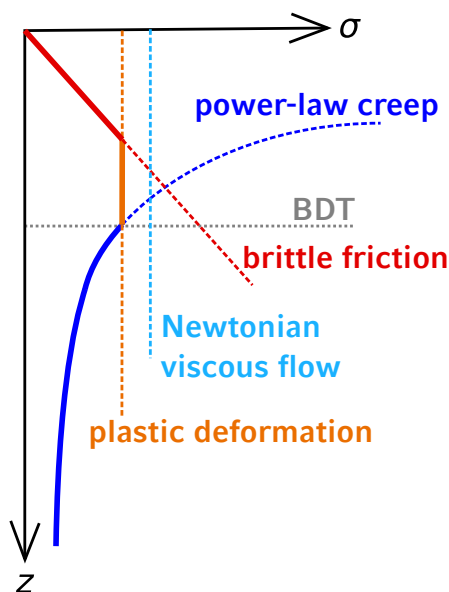


Figure 2.3: Upper limits for fault strength in SHELLS: brittle friction (linearly depth-dependent), power-law creep (exponentially temperature-dependent), plastic deformation (constant upper limit for brittle strength), Newtonian viscous flow (constant upper limit for viscosity; unlike the other lines in this diagram, the limit for ductile strength is not fixed, but dependent on strain rate). The solid line denotes the effective strength envelope.

$$\sigma_{c,\max} = \eta_{\max} \cdot \dot{\epsilon} \quad (2.5)$$

In the original version of SHELLS, the effective friction coefficient μ^* and dislocation creep activation energy Q are set globally via input parameter file. In order to have a better control on both the brittle and ductile fault strength, we have modified the code such that μ^* and Q can be assigned to each fault in the grid file individually.

2.3 Assumptions and Simplifications

SHELLS uses some simplifications in its calculations. It assumes the Earth to be spherical, to have constant density and gravity, to have a purely anelastic rheology that can be described as a Newtonian fluid with varying viscosity, to be incompressible, and to have constant thermal properties. Furthermore, the lithosphere is assumed to have a negligible thickness and no flexural strength.

Several of these assumptions and simplifications can be justified because they have no or only little influence on the balance of forces. The variations in gravitational acceleration, density and sphericity of the lithosphere do have an effect on the absolute value of the gravitational force, but these influences are small. The gravitational force has no influence on the horizontal plate motions, since it acts perpendicular to them. Only the horizontal gradients in gravity act as a driving forces; but since these variations are already small, their horizontal gradients become negligible. For example, the deviation of the geoid from the sphere is only around 0.3% in radial direction and its variation spans over thousands of kilometers, so there is effectively neither an influence on the driving forces nor on the grid geometry. The same holds for variations in gravitational acceleration: The total value varies by only a few percent, and this is mostly caused by the rotation of the Earth and its flattened shape, so the variations occur again over thousands of kilometers. Local density variations due to mineral compositions are even smaller. Also the assumed incompressibility does not have an effect on the horizontal equilibrium of forces. The bulk modulus of crustal rock is $K \approx 700$ GPa. Together with a pressure at 100 km depth (base of the lithosphere) of 3 GPa, this yields a volume change of only 0.4% in vertical direction. The pressure gradients in horizontal direction are much smaller, so horizontal density variations due to the compressibility of rock are also negligible.

The other simplifications are performed mostly because there is no detailed data available. For example, elastic deformations in the lithosphere do exist, but they cannot be observed from geologic fieldwork; only plastic deformations leave traces over geologic times. And since elasticity plays only a minor role in areas of strong deformation where faulting occurs and decays in the long term, it can be omitted if the considered time span is larger than the Maxwell time of the lithosphere. The downside is that earthquake cycles cannot be represented; thus, short-term measurements like GPS data cannot be compared directly to the modeled average behavior, but the model results must undergo a correction first. Also the linear Newtonian rheology is just a simplification, for the true rheology has power law character. Therefore an idealized linear rheology is assumed and adjusted at each iteration. Similarly, there is a high variability in the thermal properties — thermal conductivity and radiogenic heat production — of different minerals, and heat transfer is not always predominantly conductive. But an average geotherm can be assumed for simplicity. Since these properties are only used in conjunction with the surface heat flow to compute the temperatures at depth, it is sufficient to adjust the surface heat flow in order to get plausible temperatures at depth, without having a detailed knowledge about the origin and transport of the heat.

The third type of simplification, namely the thin shell approximation, has been

made in order to reduce the computational complexity. The lithosphere is assumed to be a two-dimensional spherical shell. The rationale for this assumption is that the horizontal extension of the lithosphere is much larger than its vertical dimension. Additionally, horizontal velocities (whole plates move at several cm/year rates) are much larger than vertical velocities (only few mountain ranges grow at mm/year rates, but whole plates have a vertical velocity close to zero), so the vertical dimension can be represented by the vertical integral of its properties on a two-dimensional plate. This reduction by one dimension reduces the computational costs and memory requirements, without introducing much of an error. Alternatively, the horizontal resolution can be increased while maintaining the same computational effort.

A consequence of the thin shell approximation is the omission of vertical shear tractions; thus, any uncompensated buoyant forces cannot be counteracted by flexural strength, but emerge as horizontal pressure gradients, and hence lateral driving forces. As the Maxwell time of the lithosphere is much smaller than the age of the Earth, there has been enough time to equilibrate for most of the lithosphere; exceptions are only regions with a recently changed vertical load, e.g. ice sheets. Thus, lithostatic equilibrium is a reasonable assumption for most of the Earth and advisable in order to avoid driving forces that are unrelated to the global plate motions.

2.4 Input Parameters

The basic principle of SHELLS is to compute the equilibrium between driving and resisting forces. The major part of driving forces comes from viscous coupling to a velocity field in the mantle. The velocity vectors are either read from a separate file and interpolated over the grid nodes, or the velocity field is computed from a set of built-in Euler poles (*Bird, 2003*) and appropriate plate boundaries (see also section 4.1.3). It is possible to couple only continental lithosphere to the mantle velocity field; for this, the type of lithosphere is determined from the topography. If the elevation is above -2500 m, it is assumed to be continental, otherwise oceanic.

A second contribution to the driving comes from horizontal pressure gradients, caused by topography. The elevation of every node is stored in the grid file, as well as the thickness of crust and mantle lithosphere. In order to compute the weight of rock, two average rock densities are assumed for the two layers of the lithosphere, and all areas with an elevation below sea level are assumed to be covered by water. The only larger inaccuracy that remains are polar ice sheets. Since the ETOPO

datasets are now available with and without ice coverage, we were able to compute the reduced elevation of the ice sheets if they had the same density as rock.

In order to avoid vertical excess pressure, SHELLS takes the lithosphere to be in isostatic equilibrium, i.e. the weight of orogens is assumed to be compensated by the buoyancy of continental roots. This is a reasonable assumption, since the Maxwell time for the crust is much smaller than the age of the Earth, so there has been plenty of time for most of the lithosphere to equilibrate. Uncompensated excess pressure can be expected only for a few regions where the load has changed recently, e.g. due to changing ice sheets, and for convergent margins. The thicknesses of crust and lithospheric mantle can be computed from topography and heat flow using the auxiliary program *OrbData*; the crustal thickness is controlled by the required buoyancy, and the thickness of the lithospheric mantle is given by the temperature difference between crust and asthenosphere. But even if the lithosphere is in isostatic equilibrium, the higher elevation of one grid point compared to the neighboring one and the corresponding higher buoyancy of the thicker crust cause an increased pressure and thus a horizontal force towards points with lower pressure.

The resistance to deformation is determined by the friction coefficient and the parameters of the power law creep equation. These values are specified in the input parameter file; in our modified version, the effective friction coefficient and the creep activation energy are assigned to each fault in the grid file. A further important influence on the creep behavior is the rock temperature. Since the temperatures at depth are largely unknown, they are computed using the surface heat flow (specified per node in the grid file) and the thermal properties, namely thermal conductivity and radiogenic heat production, which are specified in the input parameter file. This assumes a purely conductive heat flow. Furthermore, the temperature is used together with the thermal expansion coefficient to compute the buoyancy of the lithosphere.

2.5 Output and Comparison with Observations

Solving the equation of motion gives a horizontal velocity field, which is the direct output of SHELLS. Other parameters can then be computed from the velocity field and these can be compared with observations:

- The differential velocities along fault traces can be compared with observed fault slip rates and seafloor spreading rates. Due to the anelastic nature of the computation, one must compare to geologic slip rates that are averaged

over the seismic cycle, i.e. over more than the crustal Maxwell time of approximately 10,000 years.

- The horizontal velocity field itself can be compared to geodetic measurements like GPS data. Since this data is short-term by its nature, additional corrections must be performed on the computed velocity field in order to account for the interseismic locking of faults and the resulting elastic strain of the surrounding continuum. The auxiliary program *OrbScore* uses an elastic halfspace correction from *Mansinha and Smylie (1967)* which assumes the brittle part of the crust to be locked, from the surface down to the brittle–ductile transition depth. This is done by adding a reverse velocity field to the fault nodes which sets the net fault slip rates to zero. This reverse velocity field leads to an elastic deformation of the continuum. The original velocity field, readjusted by the elastic deformation of the continuum, can then be compared to geodetic short-term measurements.
- From the gradients of the velocity field the directions of maximum horizontal compressive stress (S_{Hmax}) can be determined, and compared with data from the World Stress Map project (*Heidbach et al., 2008*). In combination with the fault geometry (given as input), these also determine the type of faulting (normal, reverse, strike-slip), which can then be compared to observed fault types in the field.

Additional information can be found in the log file of SHELLS, for example the depth of the brittle–ductile transition (BDT). This can be compared to the maximum hypocenter depths of earthquakes and used to constrain the range of models that can be considered realistic. For example, models that fit all other observations but have zero depth to BDT are computationally possible, but obviously physically unrealistic.

3 Case Studies

3.1 California: The Strength of Faults in the Crust in the Western United States¹

3.1.1 Abstract

The strength of secondary faults within plate-boundary zones and master faults like the San Andreas has been controversial for decades. We use a global finite-element code with a variable-resolution grid and global plate-driving forces to determine whether the effective friction μ^* on the San Andreas fault is high ($\mu^* 0.6-1$), intermediate ($\mu^* 0.5-0.3$) or low ($\mu^* \leq 0.2$), whether a single value of μ^* can be used for all mapped faults within California, and whether weakening of the ductile lower crust associated with faulting is important. We compare our model results with existing data on fault slip-rates, GPS velocity field, stress field, and earthquakes depth distribution. The comparison indicates that all faults are weak ($\mu^* \leq 0.2$), and that additional weakening of major faults is important. All viable solutions also indicate that weakening of the lower crust below major faults is necessary. The strongest faults in the region have μ^* in the range 0.2–0.05. The San Andreas fault is a very weak fault among weak faults, with $\mu^* < 0.05$. Our results also show that a global code with appropriate grid-refinement and driven by global plate motions can reasonably reproduce regional tectonics.

3.1.2 Introduction

There is little agreement concerning the brittle strength of large strike-slip faults like the San Andreas, or even the strength of faults in general. Determining the strength of faults has significant implications for structural geology, tectonics, and seismology. According to classic fault mechanics theory (*Anderson, 1942; Byerlee,*

¹Published as: Carena, S., and C. Moder (2009), The strength of faults in the crust in the western United States, *Earth and Planetary Science Letters*, 287(3–4), 373–384, doi:10.1016/j.epsl.2009.08.021

1978), the San Andreas fault should not be able to slip in its current orientation. Other faults, like low-angle normal ones, should not even exist, and those that do exist exhibit anomalous seismicity (*Wernicke, 1995; Axen, 2007*). Several authors have shown that at least some large faults in different tectonic settings appear to be much weaker than predicted by Byerlee's Law (e.g. *Mount and Suppe, 1987; Zoback et al., 1987; Bird and Kong, 1994; Carena et al., 2002; Townend and Zoback, 2004; Bilotti and Shaw, 2005; Suppe, 2007*).

Concerning the San Andreas fault, there are arguments both in favor of it being weak (*Lachenbruch and Sass, 1992; Bird and Kong, 1994; Zoback, 2000; Hardebeck and Hauksson, 2001; Townend and Zoback, 2004*) and of it being strong (*Scholz, 2000a,b*). Even though the hypothesis of a weak San Andreas fault currently encounters more favor, the definition of "weak San Andreas" itself varies considerably and the range of proposed effective friction coefficients (μ^*) is rather wide, from ≈ 0.05 (*Zoback et al., 1987; Bird and Kong, 1994; Townend and Zoback, 2004*), to ≈ 0.1 (*Humphreys and Coblenz, 2007*) to ≈ 0.3 (*Townend and Zoback, 2004*). Large faults in other tectonic settings may be equally weak or even weaker, and plate-boundary faults appear to be overall very weak, with μ^* as low as 0.03 (*Iaffaldano et al., 2006*).

There are also questions concerning whether μ^* is the same for all faults in a region, or whether it is even constant along strike on the same fault. For example, in California, *Scholz (2000a)* infers Byerlee friction not only on the San Andreas fault, but on all nearby faults as well ("strong fault in a strong crust"). *Hickman and Zoback (2004)* and *Townend and Zoback (2004)* instead postulate the existence of a weak San Andreas surrounded by strong smaller faults that have all the same μ^* ("weak fault in a strong crust"). Other possibilities are an intermediate-strength San Andreas fault (*Hardebeck and Michael, 2004*), a San Andreas fault whose strength varies along strike (*Provost and Houston, 2003; Townend and Zoback, 2004*), and a model where all faults in California are equally weak (*Hardebeck and Hauksson (2001); Hardebeck and Michael (2004)*; "weak fault in a weak crust"). Finally, *Bird and Kong (1994)*, based on a flat-Earth finite element model, concluded that all faults in California are weak in the brittle crust ($\mu^* \approx 0.2$), but that the ones with the largest net slip are likely even weaker (slip-dependent weakening), suggesting anomalous pore pressure due to thick fault gouge as a possible reason. Heterogeneous friction has also been suggested by *Rivera and Kanamori (2002)* based on variability of earthquake focal mechanisms. As far as the frictional strength in the upper crust is concerned, we want to determine whether the effective friction on the San Andreas is high (i.e. Byerlee friction, or $\mu^* = 0.6 - 1$) or low ($\mu^* \leq 0.2$), and whether a single value of μ^* can be used for all faults within our region of interest.

Recent works by *Bürgmann and Dresen* (2008) and *Thatcher and Pollitz* (2008) suggest that the brittle strength of faults cannot be studied independently of their strength in the ductile lower crust. Evidence of weakening in the lower crust below faults would also contribute to settling a long-standing debate as to whether major faults exist at lithospheric scale (e.g. *Tapponnier et al.*, 1986; *Thatcher*, 1995; *Jackson*, 2002), or are confined to the brittle crust (e.g. *England and Houseman*, 1985; *Houseman and England*, 1986, 1993). We therefore test for fault behavior in both the brittle and the ductile zones simultaneously.

We focus on the San Andreas fault and its surrounding fault network in western California because of the large amount and good quality of data available, and because the numerous studies that have already been carried out help us constrain at least some parameters. We also include in our model the neighboring areas of eastern California and western Nevada, in order to provide a smooth transition between the global and local grid of our model.

3.1.3 Models

We use SHELLS (*Kong and Bird*, 1995; *Bird*, 1999), a global finite element code, for modeling. We opted for a global finite element code instead of a flat-Earth one in order to avoid unphysical boundary conditions at the edges of our area of interest. A global code has never been used before to model the behavior of a regional area in such detail, therefore our work is as much an investigation of fault strength as it is a feasibility test for this type of models.

In SHELLS, elastic strain is neglected and only permanent strain is considered, therefore the results of SHELLS calculations correspond to an average over several seismic cycles. The rheology of the model is thus elastic everywhere, and the active deformation mechanisms are either frictional sliding along faults or nonlinear dislocation creep. In dislocation creep, $\dot{\epsilon}$ (strain-rate) relates to stress (σ) and creep activation energy (Q) through the power-law equation

$$\dot{\epsilon} \propto A \sigma^n \exp\left(-\frac{Q}{RT}\right), \quad (3.1)$$

where A is the shear stress coefficient, R the gas constant, and T is the temperature. In the model frictional sliding and dislocation creep compete at faults: friction dominates in the upper part, where the normal force is small, while dislocation creep dominates at depth, where the temperature is high enough to achieve substantial slip-rates. The depth of the transition between the two for each fault element (brittle–ductile transition depth) is calculated by assuming that the rheology resulting in the lowest shear stress will prevail.

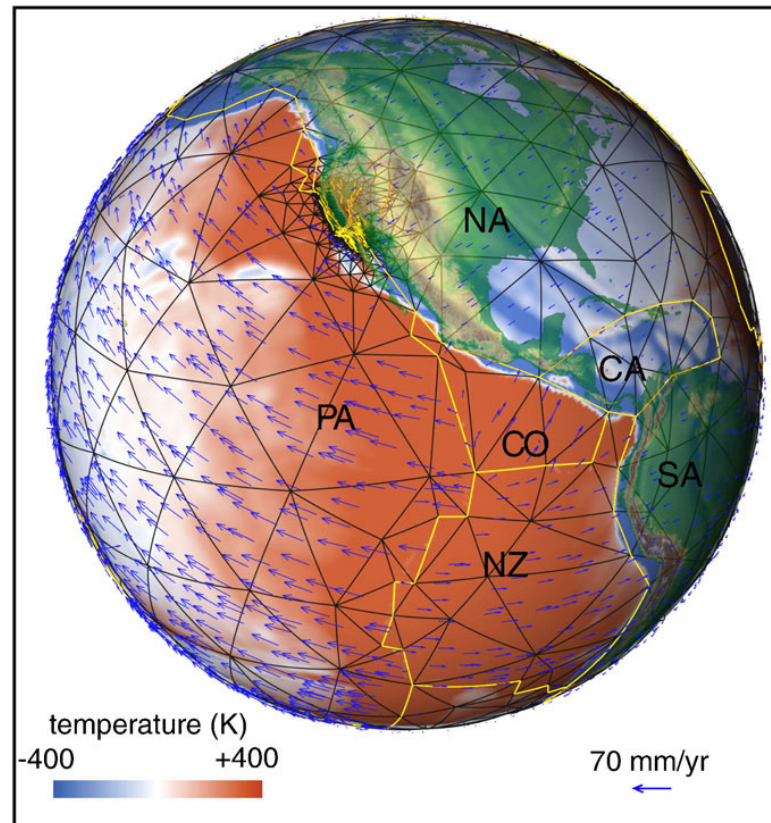


Figure 3.1: Global grid showing temperature at 100 km depth as deviation from the average calculated at that depth, and MCM velocity vectors (blue arrows) at 100 km depth. Faults and plate boundaries are in yellow. PA = Pacific, NA = North America, CO = Cocos, CA = Caribbean, NZ = Nazca, SA = South America.

The only boundary conditions that need to be specified are the global plate-driving forces, for which we tested both NUVEL-1A velocities, and velocities derived from global mantle circulation modeling (*Bunge et al.*, 1998, 2002) applied at the bottom of the plates everywhere in our model. The actual depth at which velocities are applied does not significantly affect results, as long as the velocities are not applied within the crust itself. We adopt a high-resolution mantle circulation model (Fig. 3.1, *Schubert et al.*, 2009) that provides sufficient spatial resolution to resolve the vigorous convective regime of the mantle. In addition to representing the dynamic effects from a mechanically weak asthenosphere on mantle flow (*Richards et al.*, 2001), the model incorporates internal heat generation from radioactivity together with a significant amount of heat flow from the core, for which there is growing evidence (*Bunge*, 2005; *van der Hilst et al.*, 2007). Combined with constraints on the history of subduction (*Engelbreton et al.*, 1984; *Richards and*

Engebretson, 1992) this allows us to place first-order estimates on the internal mantle buoyancy forces that drive plates.

We assume we have a good knowledge of the 3-D fault geometry, and then solve for fault strength. In particular, we examine the effect of effective fault friction (μ^*) in the upper brittle part of the crust and of creep activation energy (Q) in the ductile lower crust. SHELLS calculates forces and velocities, which we use to compute parameters that can be directly compared with data (fault slip-rates, GPS velocities, earthquakes depth distribution, and stress directions) in order to score our model and determine fault strength. Input for the model is provided as information about fault geometry, topography and heat flow, stored in the finite element grid, and as parameters like friction coefficients and creep activation energies for crust and mantle (a complete list of parameters and values used is provided in table 3.1). Such models have already been shown to produce realistic results at global scale (e.g. *Bird, 1999; Iaffaldano and Bunge, 2009*) and therefore we chose our set of global parameters to match published models. In this paper we limit ourselves to describing the local modifications to strength-controlling parameters, with the understanding that global parameters remain unchanged throughout the entire set of simulations.

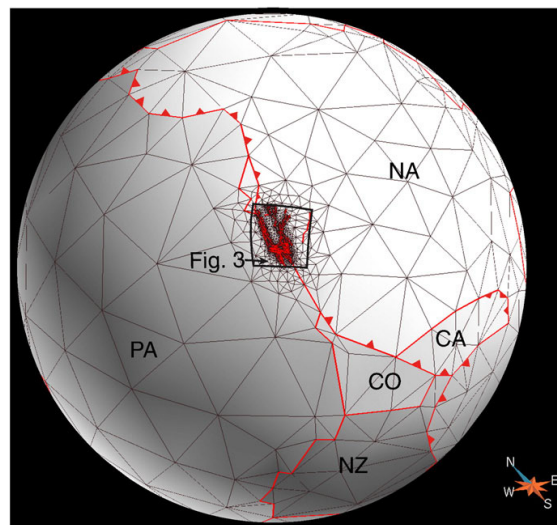


Figure 3.2: Variable-resolution grid, global view. The largest elements at global level have sides of $\approx 2 \times 10^3$ km away from plate boundaries, and 1×10^3 km at plate boundaries. NA = North American plate, PA = Pacific plate, CO = Cocos plate, NZ = Nazca plate, CA = Caribbean plate. Plate boundaries from *Bird (1999)*.

SHELLS uses a grid of spherical triangles for the continuum elements, and arcs of great circle for the fault elements (*Kong and Bird, 1995*). To drive the local model

as part of a global one, we constructed a variable-resolution grid (Fig. 3.2) that gradually transitions from a low-resolution global grid to a high-resolution local one covering California and western Nevada (Fig. 3.3). In order to position the fault elements as accurately as possible, we built the grid using Gocad (Mallet, 2002), which allows us to incorporate the faults directly into the local grid and to optimize the mesh for triangle equilaterality and smooth transition between local and global grid, while keeping the fault elements fixed in 3-D space. The distance between nodes in the local part of the grid varies between about 5 km and 50 km. This distance is based on the level of complexity of the fault geometry in a given area, rather than on the resolution of the topography and heat flow data: complex fault junctions and closely-spaced faults need a higher density of nodes, because they cannot otherwise be separated and represented in the grid. At every point the node spacing in our grid is at least the minimum required to separate the faults that we want to represent. Tests with a grid finer than that did not produce any significant changes in the results. Removing minor faults from the grid also did not alter significantly the slip-rates of remaining faults, it simply resulted in more distributed deformation of the continuum in between them.

In addition to defining grid geometry, we must also define the values of topography and heat flow at each grid node (to compute thickness of crust and lithospheric mantle), and the dip of each fault element. Topography is linearly interpolated onto our grid from the ETOPO2 data set (Fig. 3.3; *National Geophysical Data Center*, 2006). We generated a surface heat flow map for California and western Nevada by merging the heat flow data of the U.S. Geological Survey *U.S. Geological Survey* (2007) and of the Southern Methodist University *Southern Methodist University* (2007) heat flow databases. The remainder of the grid is assigned heat flow values based on the Global Heat Flow Database of the International Heat Flow Commission *International Heat Flow Commission* (2005). Crustal thickness is then calculated from topography and heat flow assuming an isostatically compensated crust and using the Airy compensation (Bird, 1999). Where necessary, we locally correct heat flow values so that the calculated crustal thickness matches the crustal thickness map of *Fuis and Mooney* (1990).

Only active faults, here defined as faults that show signs of Quaternary activity, are included in the model. The assumption of well-known fault geometry for active faults is a reasonable one in most of California and at our current resolution. In the past 5–10 years, efforts towards building reliable fault models have resulted in two major 3-D fault geometry databases available for California: the SCEC Community Fault Model (Fig. 3.4) (SCEC CFM; *Plesch et al.*, 2007) and the U.S. Geological Survey 3-D Bay Area Geologic Model (*Graymer et al.*, 2005; *Horsman et al.*, 2008; *Jachens et al.*, 2009). The geometry of the faults at the margin of the

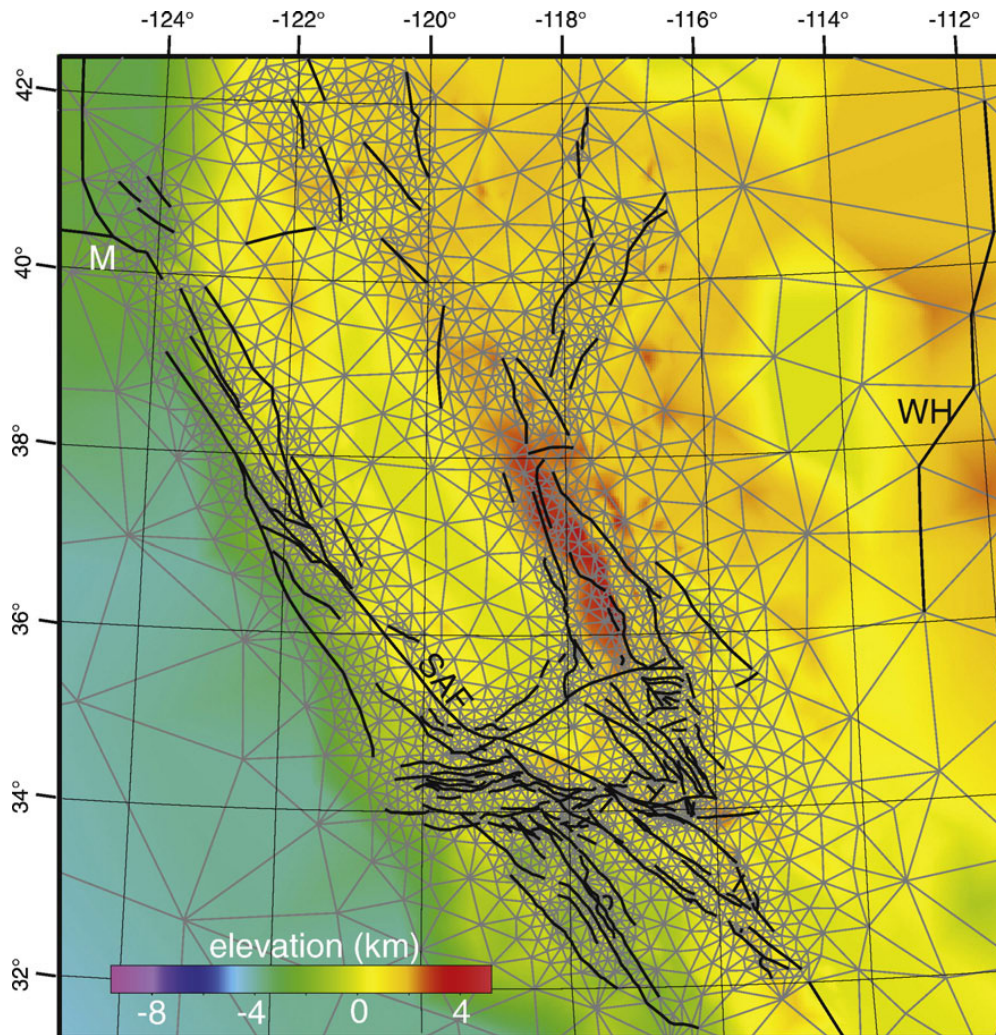


Figure 3.3: Local, high-resolution grid, with topography from ETOPO2 (*National Geophysical Data Center, 2006*) and fault elements (thick black lines). M = Mendocino triple junction, WH = Wasatch-Hurricane fault system, SAF = San Andreas fault.

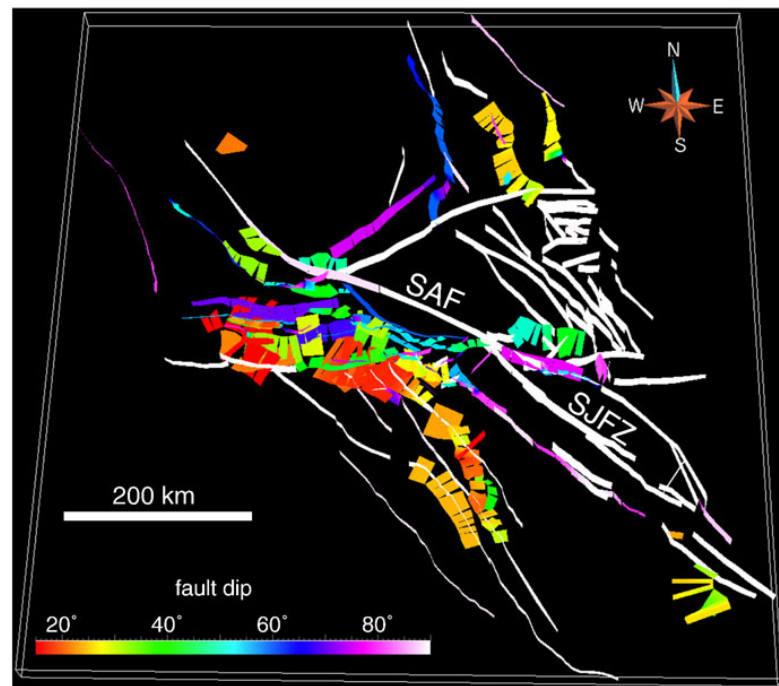


Figure 3.4: Perspective view of the SCEC Community Fault Model, simplified version that represents fault segments as rectangular patches (Plesch *et al.*, 2007). SAF = San Andreas fault, SJFZ = San Jacinto fault zone.

area of interest (northeastern California and western Nevada) is less constrained. For most of these fault, we obtained the strike and dip information from the USGS Quaternary Fault and Fold database (U.S. Geological Survey, 2006). Most of the faults in northeastern California and western Nevada are not used in scoring the model due to the uncertainties in both geometry and slip-rates. We do not force connections between faults in the grid unless they are documented, because fault segmentation is usually real. Our purpose is to keep the model network geometry as close to reality as possible. Connectivity between faults is accomplished by including all known active faults in the model, without imposing any cutoff at a predetermined slip-rate. This allows us to preserve small connecting faults in the model that would otherwise be excluded due to their small slip-rates.

3.1.4 Results

Velocity vectors resulting from the calculations can be used to make specific predictions. We want to predict from our model long-term fault slip-rates (geologic rates), azimuth of maximum compressive horizontal stress (S_{Hmax}), depth to BDT

(brittle–ductile transition), and horizontal velocities. The latter need first to be corrected in order to simulate temporary fault locking before they can be compared with geodetic data. The method used for this correction follows *Savage* (1983) and is described in detail by *Liu and Bird* (2002). To summarize it, elastic dislocation corrections are calculated for the brittle (locked) part of each fault element and then added to the long-term velocities predicted by our models. In this way, model results and observations can be compared directly in the short-term realm of GPS velocities. It is important to note here that the BDT depth used to define the base of the locked zone in our models is calculated independently of any “locking depth” intrinsic to the GPS data themselves.

Our model can then be scored against actual observations: 59 faults with reliable geologic slip-rates (SCEC CFM, *Plesch et al.*, 2007; USGS Quaternary Fault and Fold database, *U.S. Geological Survey*, 2006), 964 A-C quality S_{Hmax} directions from the World Stress Map database (*Reinecker et al.*, 2005), and 1345 permanent and campaign GPS station velocities (*Hackl and Malservisi*, 2008). We can also verify whether our predicted BDT depth is consistent with the hypocentral depth distribution extracted from the Southern and Northern California Earthquake Catalogs. Concerning the quality of fault data, the faults used in slip-rate scoring are A-quality faults (table 3.2) for which $\text{Max slip-rate} - \text{Min slip-rate} \leq \text{Average slip-rate}$, which correspond to 59 of the faults listed in table 3.2 for a total of 408 individual fault elements. As a measure of misfit we chose the RMS error in mm/yr for long-term slip-rates and for GPS velocities, and the mean error in degrees for stress directions. For each computed model we also verify whether the BDT depth is realistic. Most of the seismicity in the region is confined to depths of less than 20–25 km: brittle faults at larger depths are unrealistic, as are faults moving by dislocation creep to within a few km of the Earth’s surface.

In order to find the optimum value of μ^* for California faults, we started by decreasing it systematically from 0.6 (lower bound of Byerlee’s friction) to 0.001, initially assigning the same μ^* to all faults in our local region (i.e. all faults have the same frictional strength). Plate-boundary faults outside the local region are always assigned $\mu^* = 0.03$ in agreement with *Iaffaldano et al.* (2006) and *Bird et al.* (2008), who show that low values of friction give better results. Our test shows a general preference for values of fault friction in California 5 to 10 times lower than Byerlee’s friction (Fig. 3.5). We conducted tests with both NUVEL-1A- and MCM-driven models. For the latter, MCM velocities at two different depths (100 and 200 km) are applied to the base of the plates (Figs. 3.1 and 3.5). We also test models for which mantle convection speed has been increased by 20% to simulate a larger lithosphere–mantle coupling. As shown in Fig. 3.5, differences in the results between NUVEL- and MCM-driven models are minor when compared to

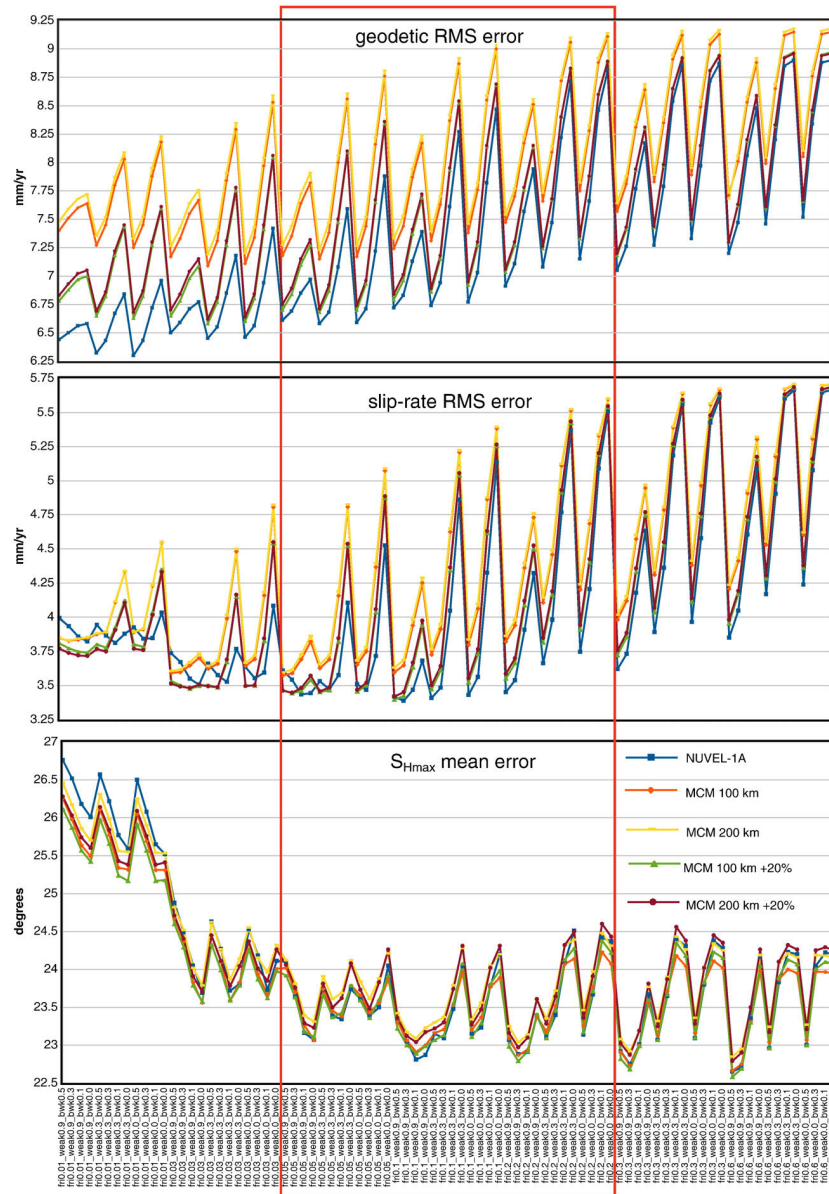


Figure 3.5: Overview of results of simulations performed with different driving mechanisms (NUVEL-1A, or MCMs from *Schubert et al., 2009*). For each value of μ^* we also test various combinations of slip-dependent weakening (as defined by *Bird and Kong, 1994*) both in the upper and lower crust. Red box shows the range in which all acceptable models (as defined in section 3) exist; no acceptable models can be produced outside this range of strengths. Key for reading x-axis: fri0.01_weak0.9_bwk0.5 = effective friction of 0.01 with 90% slip-dependent weakening in the upper crust and 50% slip-dependent weakening in the lower crust. Slip rates and horizontal velocities are sensitive to changes in all input parameters, while the sensitivity of S_{Hmax} is mostly limited to weakening. The characteristic saw-tooth pattern reveals the prominent effect of weakening the faults in the upper and lower crust, while the broad overall trend of the curves reflects the changes in initial μ^* . It is apparent that the effect of initial μ^* and weakening are of first-order importance, while the effects of changing the plate driving mechanism are second order.

the pronounced differences associated with changes in fault strength. This suggests that fault properties are a key controlling factor of our models when plate-driving forces are accounted for. In the remainder of this paper we will therefore report only results from NUVEL-driven models for simplicity.

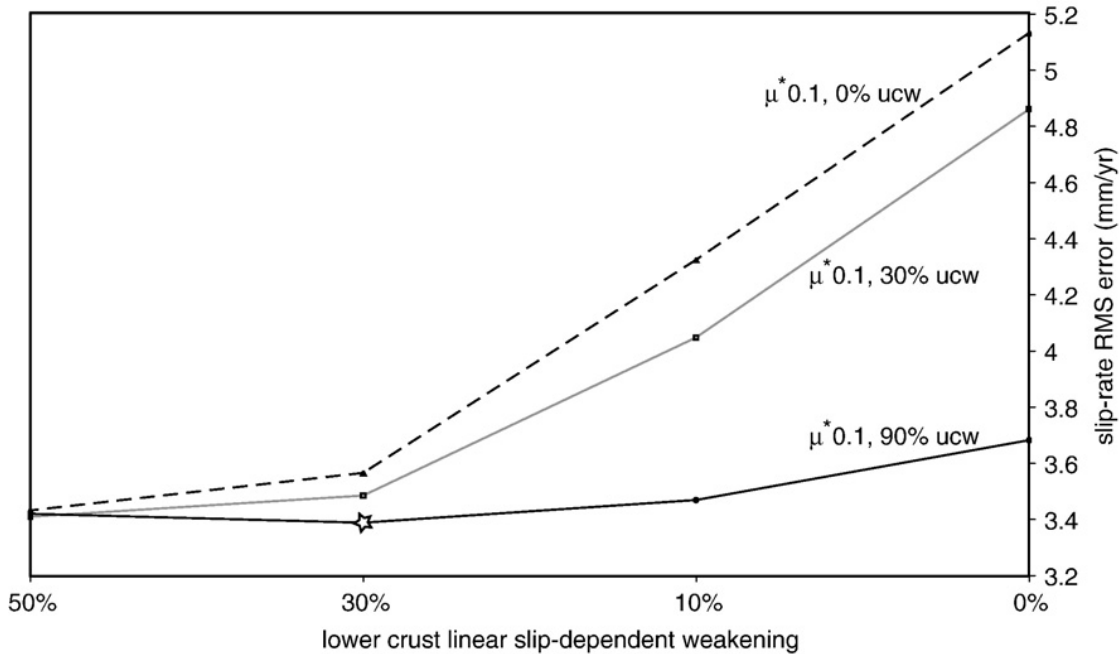


Figure 3.6: Effect of introducing linear slip-dependent weakening in the upper (ucw) and lower crust on slip-rate RMS errors. Significant upper and lower crust weakening are needed to achieve good results. The star represents our best model, which corresponds to model 2 of figures 3.8 and 3.10.

Bird and Kong (1994) postulated a linear dependency of μ^* on cumulative fault displacement (“slip-dependent weakening”): the faults with the largest net slip will also be the weakest ones. For example, if $\mu^* = 0.5$ for the fault with the smallest net slip, at 90% linear weakening the fault with the largest net slip will have $\mu^* = 0.05$. We find that slip-dependent weakening generally improves results, unless the initial μ^* value is already very low (Figs. 3.5, 3.6), and with a few notable exceptions that we will address in section 4.

Concurrently with the tests conducted on μ^* , we tested for the influence of weakening below faults in the ductile zone. We reduced the creep activation energy below faults in 10% increments from 0% to 90% of its value in non-faulted crust ($Q = 100$ kJ/mol). We examined three cases: uniform Q reduction below all faults, Q reduction below the San Andreas fault only, and slip-dependent Q reduction. The latter is analogous to slip-dependent weakening in the brittle crust. All viable models

show that moderate weakening of major faults in the lower crust is necessary to avoid excessive weakening in the brittle crust and therefore unrealistically large depths to the brittle–ductile transition. The range of models that produce acceptable results (Figs. 3.7 and 3.8) on all aspects tested (slip-rates, geodetic rates, $S_{H_{\max}}$ azimuth, and brittle-ductile transition depth) is narrow. All models fall within the range $\mu^* = 0.2$ to 0.05 with 90% linear slip-dependent weakening in the brittle crust and 30% Q reduction in the lower crust either below the San Andreas fault alone (i.e. the San Andreas is the only fault that is weakened in the lower crust), or as linear slip-dependent reduction involving all faults. This produces fault slip-rates RMS error values of 3.3–3.5 mm/yr, geodetic RMS error values of 6.5–7 mm/yr, $S_{H_{\max}}$ mean error values of 22° – 23° , and realistic maps of the depth to the brittle-ductile transition below faults (Figs. 3.7 and 3.8).

As a comparison, the average fault slip-rate (weighted by segment length) in the region is 8 mm/yr, while the average intrinsic error in the worldwide stress data set about 24° (Heidbach *et al.*, 2008) (for comparison, the average error on A–C quality data we used is about 20°). GPS velocity errors are larger than slip-rate errors because of the much larger number of elements that need to be matched: several thousands of nodes versus the few hundred segments used for fault slip-rates, resulting in many nodes lacking a data point located close enough for a good match. In addition, the need to correct our model results for temporary fault locking means that the comparison with GPS velocities can only be an approximation. Thus we define the “acceptable” ranges (Fig. 3.8) for the four parameters considered as follows: (1) slip rates RMS error: 0–4 mm/yr, where the maximum is half the regional average slip-rate; (2) $S_{H_{\max}}$ mean error: $\leq 24^\circ$; (3) GPS velocity RMS error: 0–7 mm/yr, a range that includes all of the models that score reasonably well on the other parameters; (4) average BDT depth 10–20 km, because values outside this range cannot be obtained if we want to have a realistic distribution of maximum hypocentral depths in the region. The value of 24° as a bound for the $S_{H_{\max}}$ mean error is rather high, but as evident in Fig. 3.5, of the three parameters shown this is the least sensitive to changes in the model, and making the acceptable range smaller here would have excluded too many models without good reason. There are several issues with the BDT depth as well that should be mentioned. First, like for GPS velocities, we do not have a one-to-one match with model elements. This is because there are areas of the model where we have faults, but not enough earthquakes in the record that match these faults (Fig. 3.7). Second, the earthquake depth distribution is a only proxy for BDT depth. Third, while it makes sense to assume that for old, well-established faults, the distribution of seismicity has not changed much in the last million years, this is likely not true for younger faults. Geologic slip-rates represent therefore the most robust of the four scoring data sets, because there is a one-to-one match between model faults

and real faults, and because we can compare modeled and observed rates directly, without any intermediate steps.

3.1.5 Implications for Fault Strength in California

Our results indicate that in the upper, brittle crust all examined faults in California and western Nevada are weak, ($\mu^* \leq 0.2$), and that further weakening of major faults is important: major faults are about 10 times weaker than the rest. The strongest faults in this region have μ^* in the range 0.2–0.05 and can therefore be classified as “weak”. Accounting for both the fact that several models produce acceptable results (Fig. 3.8), and that not all segments of the San Andreas have the same strength (fig. 3.10), we can conclude that the San Andreas fault has μ^* in the range 0.04–0.01 and it is therefore a weak or a very weak fault. Low effective friction on faults however does not necessarily mean a weak crust overall, as it can be inferred from the work of *King* (1986) and as explicitly stated by *Suppe* (2007). Thus, the San Andreas could be defined either as a “weak fault in a weak crust”, or a “weak fault in a strong crust”. Further studies to determine crustal strength in California independently of fault strength (for example along the lines of those conducted by *Suppe* (2007), on accretionary wedges) are needed to make this determination.

As far as the reason for such a low apparent frictional strength of faults is concerned, we agree with *Di Toro et al.* (2004) on a possible link with a drop in dynamic effective friction during earthquakes. The faults that we have considered in our simulations, with the notable exception of the creeping segment of the San Andreas fault, owe most of their total slip to earthquakes. Several laboratory studies in recent years (e.g., *Di Toro et al.*, 2004; *Han et al.*, 2007; *Tanikawa and Shimamoto*, 2009) show that a significant drop in dynamic friction, below values of 0.2 and possibly down to near-frictionless behavior (*Di Toro et al.*, 2004), occurs when rock interfaces slip at typical earthquake slip velocities. What we produce in our simulations is the long-term result of faults slipping, regardless of how such slip actually happens or is initiated; we can only predict what the integrated effect over many earthquake cycles will look like. For a fault that slips mostly in earthquakes, it is the cumulative effect of the processes happening during such events that will dominate in the long-term and control long-term observables. In other words, if the dynamic friction of a fault during its characteristic earthquake drops to 0.1, then this is the strength that will best match long-term observations for this fault, provided that over the course of its existence most of the fault area has achieved the peak slip-velocity necessary for this drop in friction. In this context, only truly creeping faults, of which the creeping segment of the San Andreas fault is one

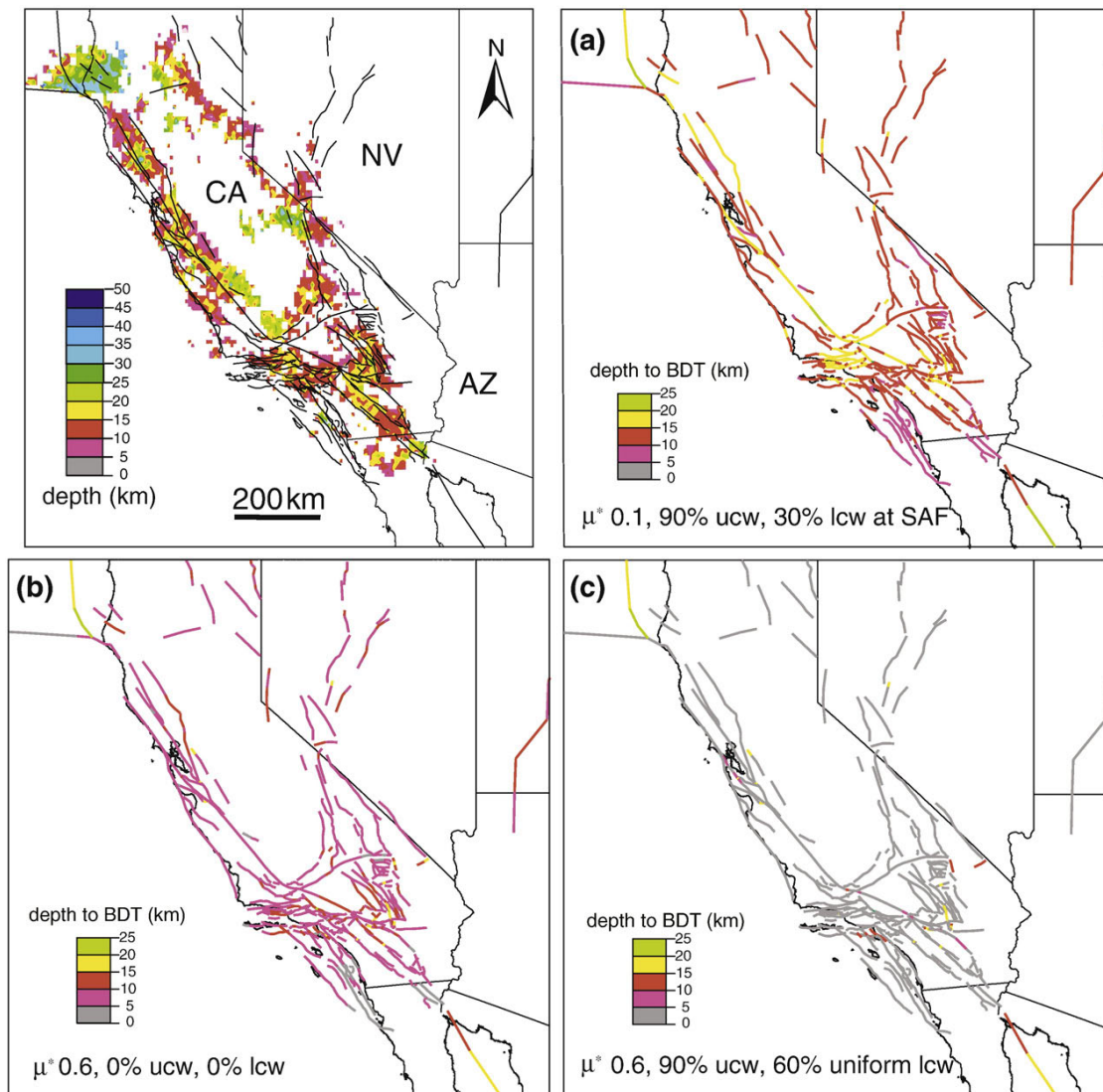


Figure 3.7: Examples of calculated depth to the brittle-ductile transition (BDT). Maximum depth of seismicity, which we use as a proxy for BDT depth, is shown in the top left corner. We created this map by taking the deepest event in each 5×5 km cell from the combined Southern California Earthquake Center (SCECDC) and Northern California Earthquake Center (NCEDC) earthquake catalogs, without any averaging or interpolation: blank cells have no earthquakes. (a) represents one of our best models with upper-crust linear slip-dependent weakening, showing a reasonable BDT depth along faults. (b) is the strong-faults case (model 1, Fig. 3.10) with no weakening, which shows too shallow BDT depth. (c) is a model with high initial friction and significant weakening, which scores at acceptable levels on slip-rates, GPS velocity and S_{Hmax} mean error, but for which the resulting BDT depth is unacceptably low. ucw = upper crust slip-dependent weakening. lcw = lower crust slip-dependent weakening, which is set as follows for the three fault maps: 30% below the SAF alone in (a), none in (b), and 60% uniform (non slip-dependent) below all faults in (c).

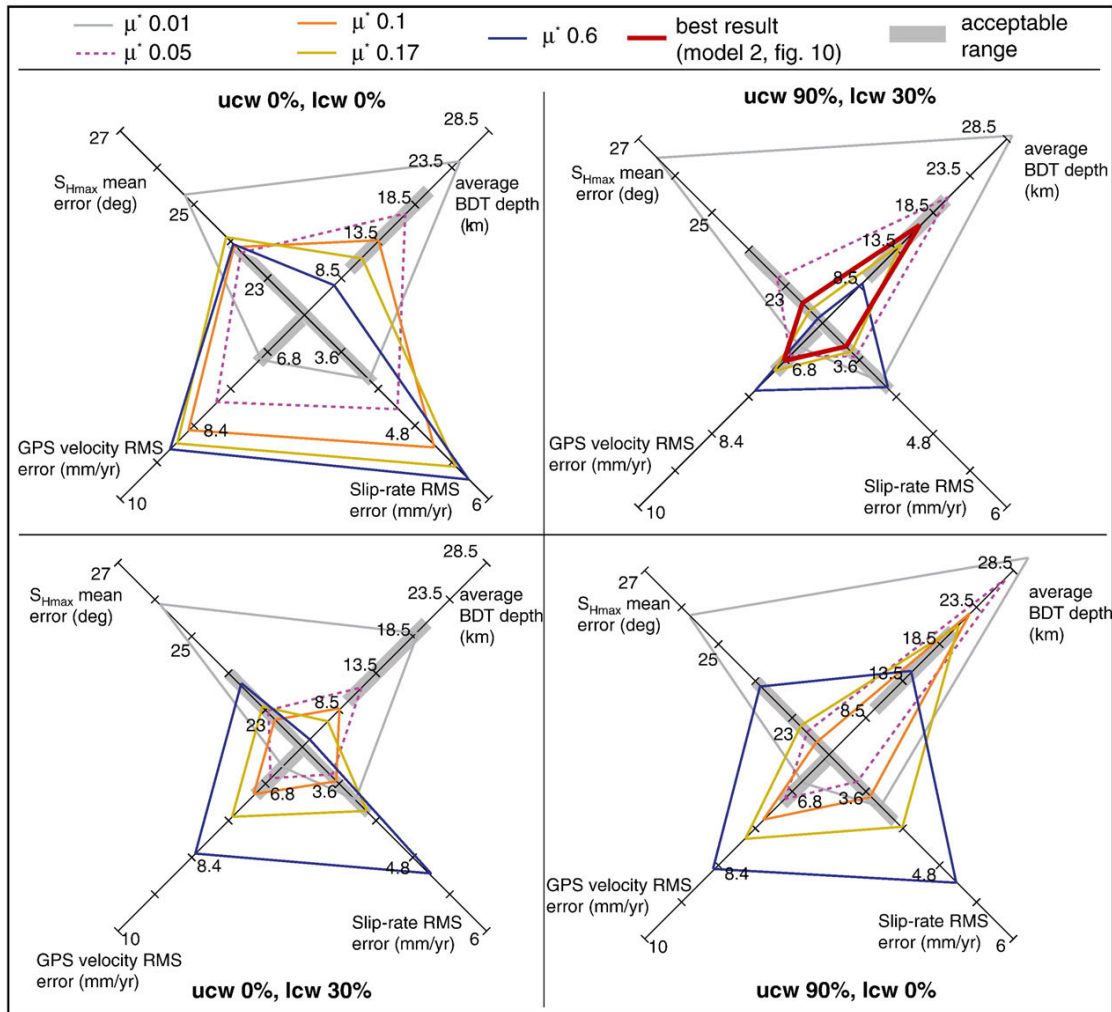


Figure 3.8: Diagrams showing the results of several different combinations of parameters for models driven by NUVEL-1A. Models are grouped according to absence or presence of slip-dependent weakening of faults in the upper and lower crust. ucw = upper crust slip-dependent weakening, lcw = lower crust slip-dependent weakening. Acceptable models must have all four vertices of the corresponding polygon falling within the gray-shaded “acceptable range” (as defined in section 3) on each axis of the diagram. Top left diagram represent the no-weakening case. The results are improved significantly by the introduction of slip-dependent weakening at faults in at least one crustal layer, as shown in the two bottom diagrams. The best results are obtained when weakening is introduced in both upper and lower crust (top-right diagram). Our best model is represented by the solid red line. Both extremely low initial friction ($\mu^* = 0.01$) and the absence of weakening coupled with high initial friction ($\mu^* = 0.6$) consistently produce poor results.

of very few known examples worldwide, need to have very low ($\ll 0.1$) intrinsic μ^* . In all other cases there is no need to invoke exceedingly weak materials or anomalously high pore fluid pressures on large swaths of these faults in order to explain the apparent low frictional strength.

A second important outcome of our simulations is that the integrated strength of faults must include contributions from both the brittle and the ductile parts of the crust, at least for major faults. The significance of this is that major faults like the San Andreas, the Altyn Tagh, the Red River–Ailao Shan, the North Anatolian Fault and many others likely exists at lithospheric level as postulated by several authors (*Tapponnier et al.*, 1986; *Thatcher*, 1995; *Jackson*, 2002), while secondary faults in the network may well be confined to the brittle crust. Lack of significant weakening in the lower crust is the likely cause of failure to match observed slip-rates in the case of several faults that are effectively branches of the San Andreas system (e.g. San Jacinto, Hayward and Calaveras), but which have insignificant net slip values compared to those of the San Andreas fault proper (see Figs. 3.9, 3.10, and table 3.2). Additional work will therefore be needed, both to define weakening relationships other than simple linear dependency on net slip, which may not be appropriate in the lower crust and/or faults like the San Jacinto, and to extend weakening into the lithospheric mantle to verify whether major faults must exist there too as discrete, narrow zones of weakness.

3.1.6 Conclusions

All faults in the vicinity of the transform plate boundary of the western USA are frictionally weak to very weak faults in the upper crust. The major faults in the system must continue as discrete, narrow, moderately weak zones also in the lower crust. Strength is not constant on all faults: major faults are significantly weaker than the rest, and in a fault system like the San Andreas strength can vary from one segment to another. Our results also demonstrate that a global finite element code with a variable-resolution grid can realistically reproduce the tectonics of local areas while being driven by global plate motions.

Acknowledgments: This project is funded by Deutsche Forschungsgemeinschaft (DFG) grants #CA691/1-1 and #CA691/1-2. The authors would like to thank the anonymous reviewer whose comments helped to improve this paper.

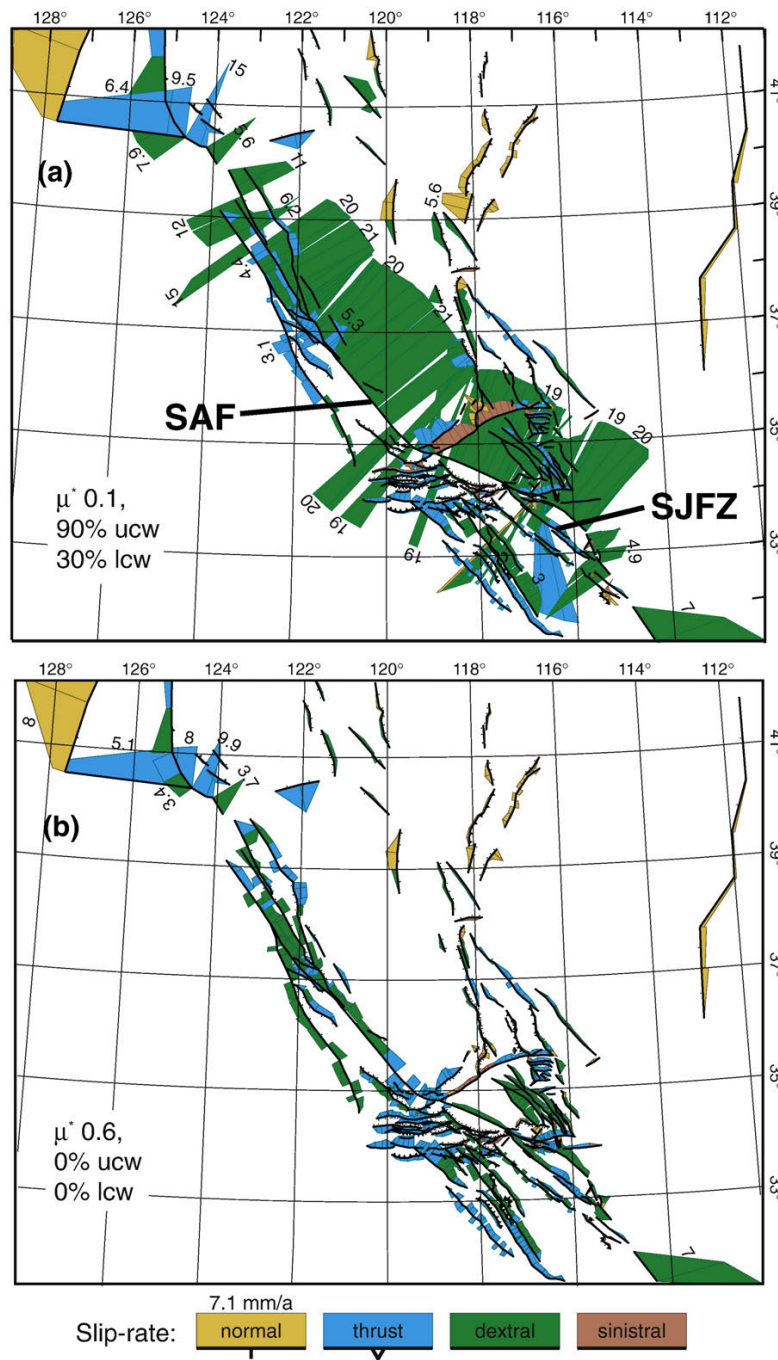


Figure 3.9: Fault slip-rates plotted as slip patches for (a) our best model (model 2 of Figs. 3.8 and 3.10) and (b) for the high-friction, strong-faults case (model 1 of Fig. 3.10). The color of slip-rate patches represents the dominant slip component. Numbers next to the patches are slip-rates in mm/yr. Both slip-rates and type of faulting match observations much better when the strength of faults is low and slip-dependent weakening is introduced. In addition to a marked slip-rate increase in (a) when compared to (b), we can also observe that the compression along the Big Bend of the SAF visible as thrust faulting (blue) in (b) disappears in (a). The SAF becomes a dominantly right-lateral strike-slip fault and compression is now confined to faults on either side of it. SAF = San Andreas fault, SJFZ = San Jacinto fault zone.

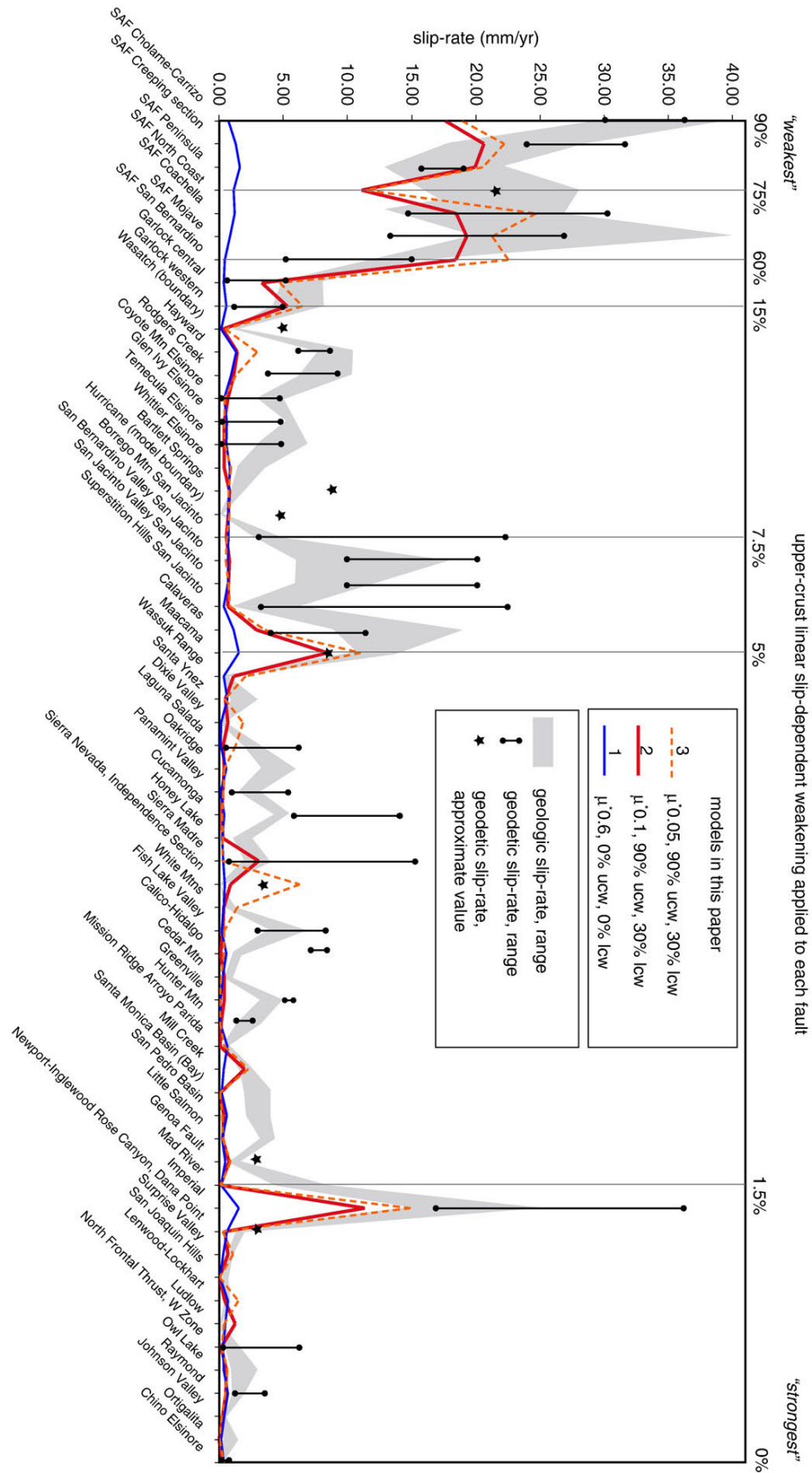


Figure 3.10: Comparison between observed slip-rates and slip-rates calculated for several models. Model 1 is the strong-faults case: all fault slip-rates are reduced to as little as 5%–10% of their observed values. Model 2 is our best model (star in Fig. 3.6), model 3 is another model that shows a slightly better fit for slip-rates on several important faults and that still produces acceptable results for the three other parameters (BDT depth, S_{Hmax} , GPS velocities, see Fig. 3.8).

Table 3.1: Parameters used in SHELLS calculations.

Parameter	Value
Continuum friction coefficient	0.85
Crust mean density	2816 kg m ⁻³
Mantle mean density	3332 kg m ⁻³
Asthenosphere density	3125 kg m ⁻³
Water density	1032 kg m ⁻³
Biot coefficient	1.00
Gravitational acceleration	9.8 m s ⁻²
Surface temperature	273 K
Crust upper temperature limit	1223 K
Mantle-lithosphere upper temperature limit	1673 K
Crust thermal conductivity	2.7 J m ⁻¹ s ⁻¹ K ⁻¹
Mantle thermal conductivity	3.2 J m ⁻¹ s ⁻¹ K ⁻¹
Crust radioactive heat production (volume)	7.27 × 10 ⁻⁷ J m ⁻³ s ⁻¹
Intercept of upper mantle adiabat	1412 K
Slope of upper mantle adiabat	6.1 × 10 ⁻⁴ K m ⁻¹
Volumetric thermal expansion coefficient (crust)	2.4 × 10 ⁻⁵ K ⁻¹
Volumetric thermal expansion coefficient (mantle)	3.94 × 10 ⁻⁵ K ⁻¹
Exponent on strain-rate in creep-stress laws (1/n)	0.333333
Temperature coefficient of creep rheology (crust)	4000 K
Temperature coefficient of creep rheology (mantle)	18,314 K
Shear stress coefficient of creep law (crust)	2.3 × 10 ⁹ Pa s ^{1/n}
Shear stress coefficient of creep law (mantle)	9.5 × 10 ⁴ Pa s ^{1/n}
Plate defining velocity reference frame	North America
Number of grid nodes	4761
Number of grid elements	6996
Number of fault elements	1363

Table 3.2: List of faults used in the model and their calculated slip-rates compared with observations. Q = quality factor (A = well-constrained geologic/long-term slip rate as reported in catalogs; B = poorly constrained geologic slip-rate — e.g. rate inferred from nearby faults; C = no geologic slip rate available); Type = observed dominant component of slip (r = reverse, n = normal, dx = right-lateral strike-slip, sx = left-lateral strike-slip, u = undetermined); D = net slip (when no value listed, we estimated it for our simulations by comparing the fault to its neighbors). Names of faults used in slip-rate model scoring are in italics. Geologic slip-rates, D values, fault type information and faults names are from the USGS Quaternary Fault and Fold Database (U.S. Geological Survey, 2006) or from the SCEC Community Fault Model Database (Plesch *et al.*, 2007) and references therein. Geodetic slip-rates are from Bennett *et al.* (2003)^a, Miller *et al.* (2001)^b, Titus *et al.* (2005)^c, McGill *et al.* (2003)^d, Shen and Jackson (2005)^e, Genrich *et al.* (1997)^f, Fialko (2006)^g, Dixon *et al.* (1995)^h, McCaffrey (2005)ⁱ, Meade and Hager (2005)^j, Lundgren *et al.* (2009)^k, d’Alessio *et al.* (2005)^m. Calculated average slip-rates are from our model 2 of fig. 3.10. Green shading indicates faults whose calculated slip-rates fall within the observed range of geologic rates (i.e. slip-rate RMS error would be zero for these faults).

Fault name	Q	Type	D (km)	Slip-rate (mm/yr)		
				Geologic	Geodetic	Calculated, average
Anza San Jacinto	A	dx	24	7–23	10–20 ^d , 3–21 ^k	0.77
<i>Bartlett Springs</i>	A	dx	33	1–2	7.3 ⁱ	0.79
Benton Spring	A	dx	8	0.13–0.4		0.59
<i>Borrego Mtn San Jacinto</i>	A	dx	24	2.8–5	3–21 ^k	0.70
<i>Calaveras</i>	A	dx	23	9–19	5.1–11 ⁱ	2.92
<i>Calico-Hidalgo</i>	A	dx	9	1–1.7	7–8 ^b	0.40
Camp Rock	A	dx	3	0.02–2	≈ 10^b	1.23
<i>Cedar Mtn</i>	A	n	9	0.5–1		0.15
Channel Islands Thrust	A	r	8	0.3–2.3	3.5 ⁱ	0.13
<i>Chino Elsinore</i>	A	dx	1	0.3–0.5	≈ 0.1^j, 1.3ⁱ	0.30
Cleghorn	A	sx	4	1–5		5.45
<i>Coyote Mtn Elsinore</i>	A	dx	40	3–5	2–4 ^d , 3 ⁱ , 0–5 ^k	0.42
<i>Cucamonga</i>	A	r	10	4.5–5.5	≈ 7 ^e , 6 ⁱ , 8.5–11.5 ^j	0.36
<i>Dixie Valley</i>	A	n	14	0.14–0.34		0.68
Emerson (Landers)	A	dx	4	0.2–1		0.49
<i>Fish Lake Valley</i>	A	n	9.5	4–7	3–5 ^b , 4.7 ⁱ , 3.9–8.1 ^j	0.27

Fault name	Q	Type	D (km)	Slip-rate (mm/yr)		
				Geologic	Geodetic	Calculated, average
Fish Lake Valley, Leidy section	A	dx	2.5	0.4–1.7	2.9 ⁱ	0.28
<i>Garlock central</i>	A	sx	64	5–8	≈ 5 ^b , 0.3–3.3 ^j	3.32
Garlock eastern	A	sx	64	1–5	1.1–2.5 ^b , ≈ 1 ^e , 1.6 ⁱ , 0–3 ^j	0.51
<i>Garlock western</i>	A	sx	64	4.3–8.3	≈ 5 ^b , ≈ 2 ^e , 4.9 ⁱ , 1.7–4.7 ^j	5.31
<i>Genoa Fault</i>	A	n	6.5	0.7–1.6	2.9 ⁱ	0.76
<i>Glen Ivy Elsinore</i>	A	dx	40	5.5–5.9	1.3 ⁱ , 0–5 ^k	0.39
<i>Greenville</i>	A	dx	9	3.3–4.9	5.0–5.8 ^m	0.09
Hat Creek	A	n	7.5	0.7–1.4		0.40
<i>Hayward</i>	A	dx	44	7.8–10.6	7.4 ⁱ , 6.3–7.9 ^m	1.40
Helendale-South Lockhart	A	dx	3	0.2–1	1–3.4 ^j	2.58
<i>Honey Lake</i>	A	dx, n	10	1.1–2.6		0.25
<i>Hunter Mtn</i>	A	dx	9	1.5–3.5	≈ 3 ^a , 2 ⁱ	0.10
<i>Hurricane</i> (model boundary)	A	n	31	0.1–0.3	5 ⁱ	0.73
<i>Imperial</i>	A	dx	4.6	15–25	17–23 ^f , 21.1 ⁱ , ≈ 36 ^j	11.38
<i>Johnson Valley</i>	A	dx	1.6	0.4–0.6		0.28
<i>Laguna Salada</i>	A	dx	12.5	2–3	2–6 ^d , 0.7 ⁱ	0.34
Lavic Lake (Hector Mine)	A	dx	3.2	0.2–1	≈ 2.5 ^b	0.11
<i>Lenwood-Lockhart</i>	A	dx	3	0.5–0.8		1.27
Likely fault	A	dx	9.7	0.1–1		1.43
<i>Little Salmon</i>	A	r	7	3.3–4.3		0.27
<i>Ludlow</i>	A	dx	3	0.1–0.3		0.45
<i>Maacama</i>	A	dx	20	11–14	7.3 ⁱ	8.46
<i>Mad River</i>	A	r	6	4.4–8.3		0.12
Malibu Coast	A	r	3.8	0.3–3.7		0.28
<i>Mill Creek</i>	A	dx	8	1.6–2.6		1.98
<i>Mission Ridge Arroyo</i>	A	r, sx	9	0.2–0.6		0.40
<i>Parida</i>						

Fault name	Q	Type	D (km)	Slip-rate (mm/yr)		
				Geologic	Geodetic	Calculated, average
<i>Newport-Inglewood Rose Canyon, Dana Point</i>	A	dx	4	1.3–2.1	$\approx 3^{e,i}$	0.46
Newport-Inglewood	A	dx	4	0.9–1.9	$\approx 3^{e,i}$	0.70
Rose Canyon, Del Mar	A	dx	4	0.9–1.9	$\approx 3^{e,i}$	0.70
<i>North Frontal Thrust, W Zone</i>	A	r	2.9	0.5–1.5	0–6 ^j	0.18
Northridge Hills	A	r	3.2	0.3–1.7		0.16
<i>Oakridge</i>	A	r	11.7	3.5–6	5.8–10.2 ^j	0.41
<i>Ortugalita</i>	A	dx	1.5	0.5–1.5		0.01
Owens Valley 1872 rupture	A	n, dx	25	0.5–3.8	$\approx 3^a, 2.6^i, 2.6–4.4^j$	0.70
<i>Owl Lake</i>	A	sx	2.6	1–3		0.55
Palos Verdes	A	dx	2	0.5–3.8	3.4 ^{i,j}	2.44
<i>Panamint Valley</i>	A	dx, n	11	1.5–3.2	$\approx 3^a, 2^i, 1.8–4.4^j$	0.27
Pisgah-Bullion (Mtn Mesquite Lake)	A	dx	10	0.2–1		0.28
Pleito	A	r	6	0.3–2		2.19
Puente Hills	A	r	5.4	0.5–2	3.3–5.1 ^j	0.15
<i>Raymond</i>	A	sx	2.6	1–2	1.3–3.3 ^j	0.57
Redondo Canyon	A	r	1.5	0.2–1		0.26
<i>Rodgers Creek</i>	A	dx	44	6.4–10.4	7.4 ⁱ , 4.2–9.2 ^m	1.14
<i>SAF Cholame-Carrizo</i>	A	dx	315	30–40	$\approx 34^b, 30.5^i, \approx 36^j$	17.62
<i>SAF Coachella</i>	A	dx	225	12.5–26.8	$\approx 30^b, \approx 25^g, 20–30^d, 25.3^i, \approx 23^j, 14–20^k$	18.48
<i>SAF Creeping section</i>	A	dx	315	18–28	24–26 ^c , 31.7 ⁱ	20.62
<i>SAF Mojave</i>	A	dx	225	20–40	$\approx 27^b, 25.1^i, \approx 5^j$	19.27
<i>SAF North Coast</i>	A	dx	295	16–28	20.9–21.1 ⁱ	11.10
SAF Parkfield	A	dx	315	26.3–39.5	31.0 ⁱ , 36 ^j	20.36
<i>SAF Peninsula</i>	A	dx	315	13–22	23.8 ⁱ , 15.7–18.5 ^m	19.94
<i>SAF San Bernardino</i>	A	dx	225	12–16	$\approx 15^b$	18.44

Fault name	Q	Type	D (km)	Slip-rate (mm/yr)		
				Geologic	Geodetic	Calculated, average
<i>San Bernardino Valley San Jacinto</i>	A	dx	24	6–18	10–20 ^d	0.58
<i>San Jacinto Valley San Jacinto</i>	A	dx	24	6–12	10–20 ^d , 11.1 ⁱ	0.83
<i>San Joaquin Hills</i>	A	r	3.6	0.3–0.7		0.04
<i>San Pedro Basin</i>	A	dx	7.3	2–4		0.36
Santa Monica Basin (Bay)	A	dx	8	2–4		0.11
Santa Susana	A	r	3	1.2–11.2	≈ 12 ^j	0.22
<i>Santa Ynez</i>	A	sx, r	14.6	1–3		0.47
<i>Sierra Madre</i>	A	r	10	2–4	3.3–5.5 ⁱ , 1.5–11.7 ^j	0.27
<i>Sierra Nevada, Independence Section</i>	A	n	10	0.08–0.19	2.6 ⁱ	3.10
<i>Superstition Hills San Jacinto</i>	A	dx	24	1–7	10–15 ^d , 3–21 ^k	0.73
<i>Surprise Valley</i>	A	n	3.8	0.6–1		0.7
<i>Temecula Elsinore</i>	A	dx	40	3–7	1.5 ⁱ	0.42
<i>Wasatch (boundary)</i>	A	n	46	1–1.3	≈ 5 ^{h,i}	0.29
<i>Wassuk Range</i>	A	n	15	0.4–0.5		1.12
<i>White Mtns</i>	A	dx	10	0.4–1.2		0.89
<i>Whittier Elsinore</i>	A	dx	40	1.5–3.5		0.67
Zayante-Vergeles	A	r	10	0.04–0.2		6.29
Ash Hill	B	dx, n	3.7	0.1–2		0.05
Banning	B	dx, r	5	1.7–2.6		10.29
Big Pine	B	sx	7	1–4	≈ 1 ^e	1.1
Black Mountains, Artists Drive Section	B	n	2	1–5		0.09
Blackwater	B	dx	6	0.2–1	≈ 5 ^b , 1.3–2.5 ^j	0.68
Burnt Mtn	B	dx	2.1	≈ 0.5		0.07
Carson City	B	n	2	0–0.2		0.50
Clamshell Sawpit (Sierra Madre)	B	r	2	0–1		0.24
Coronado Bank	B	dx, n	9	2–4	5.1 ⁱ , 2–8 ^j	2.61
Cortez Mtns	B	n	8	0.15–1.7		0.49
Coyote Creek San Jacinto	B	dx	24	2–6	10–20 ^d , ≈ 21 ^g , 3–21 ^k	0.39

Fault name	Q	Type	D (km)	Slip-rate (mm/yr)		
				Geologic	Geodetic	Calculated, average
Death Valley, Northern	B	dx	24	1–6	$\approx 3^a, 2.6^i$	0.14
Death Valley, Southern	B	dx	8	1–5	$\approx 3^a, 2.6^i$	0.63
Earthquake Valley	B	dx	2.5	1–3	2.5^i	0.19
Elmore Ranch	B	sx	2	0.5–1		0.52
Eureka Peak (Joshua Tree)	B	dx	2	≈ 0.6	$\approx 21^j$	0.25
Excelsior Mtn	B	sx	3.4	≈ 0.2		0.40
Galway Lake	B	dx	0.7	0–0.5		0.09
Garnet Hill (SGPT+Garnet Hill)	B	dx, r	2.5	2–10		4.19
Grass Valley	B	n	6.9	≈ 0.2		0.13
Gravel Hills Harper Lake	B	dx	2	≈ 0.9		0.72
Hollywood	B	sx, r	1.4	0.33–0.75	$2.1^i, 1.3–3.5^j$	0.21
Holser	B	r	2.6	0.3–0.6		0.06
Hosgri San Simeon	B	r, dx	115	1–3.5	$\approx 3^e, 4.2^i, \approx 4^j$	1.84
Julian Elsinore	B	dx	40	3–7	$2–8^d, 2.2^i, 0–5^k$	0.48
Klamath Lake faults	B	n	19	0.15–1		0.13
Little Lake	B	dx	4.5	≈ 1		1.26
Lower Pitas Point	B	r	7.8	≈ 1.3	3.1^i	0.13
Montalvo						
Mono Lake	B	n	1.8	0–1.2		1.98
Monterey Bay-Tularcitos	B	dx	9	0.1–0.9		0.68
Newport-Inglewood L.A. Basin North	B	dx	3	≈ 1	$\approx 3^{e,i}, \approx 0.8^j$	0.69
Newport-Inglewood L.A. Basin South	B	dx	3	0.6–1.2	$\approx 3^{e,i}, \approx 0.8^j$	0.57
Newport-Inglewood Rose Canyon, Ocean-side	B	dx	4	≈ 0.8	$\approx 3^{e,i}$	0.73
Newport-Inglewood Rose Canyon, San Diego	B	dx	4	1–2	$\approx 3^{e,i}$	0.50

Fault name	Q	Type	D (km)	Slip-rate (mm/yr)		
				Geologic	Geodetic	Calculated, average
Newport-Inglewood Rose Canyon, Silver strand	B	dx	4	1–5	$\approx 3^e, i$,	0.19
North San Gabriel	B	dx	7	1–5	$\approx 6^e, 0.8^i$	0.21
Point Dume	B	dx	7.5	1–5	2.8^i	0.85
Red Mountain	B	r	1.9	0.4–11.6		0.16
SAF Santa Cruz Mtns.	B	dx	315	13–21	22.1^i , $15.4–17.4^m$	18.77
San Cayetano	B	r	5.8	1.3–9	$\approx 2^e$, $2.1–6.3^j$	0.36
San Diego Trough	B	dx	15	1.1–2.1		0.31
San Jose	B	sx	1.8	0.2–2		0.23
Santa Cruz Catalina Ridge	C	dx, r?	6	—		0.86
Santa Rosa Island	C	r	7.8	—		0.26
Sierra Nevada, Haiwee Reservoir Section	B	n	10	0.2–1	5.9^i	1.00
South San Gabriel	B	dx	7	1–5	0.8^i	0.26
Superstition Mtn San Jacinto	B	dx	24	1–5		0.47
Tank Canyon	B	n	2.3	0.5–1.5		0.13
Toiyabe Range	B	n	17	≈ 0.22		0.41
Ventura Pitas Point	B	r	5.4	0.4–1.5		0.36
Verdugo	B	r	2.7	≈ 0.5		0.16
White Wolf	B	r	7.8	0.3–0.9	$2.9–6.1^j$	0.15
Anaheim	C	u	2	—		0.37
Bicycle Lake	C	u	—	—		0.05
Big Bear 1	C	sx	3	—		0.52
Big Bear 2	C	u	—	—		0.75
Black Mountains, Smith Mountain Sec- tion	C	n	2	—		0.49
Blue Cut	C	sx	11	—		0.12
Brawley Seismic Zone	C	dx	6.8	—	$\approx 25^e, 22.6^i$	3.59
Cady	C	u	—	—		0.03
Canada David detach- ment	C	u	—	—		0.54
Carlsbad	C	u	—	—		0.14

Fault name	Q	Type	D (km)	Slip-rate (mm/yr)		
				Geologic	Geodetic	Calculated, average
Cerro Centinela detachment	C	u	—	—		0.34
Cerro Prieto	C	dx	11.5	—	$\approx 40^j$	0.11
Coyote Canyon	C	u	—	—		0.31
Coyote Lake	C	u	—	—		0.21
Del Valle	C	u	—	—		0.22
Dixie Valley East	C	n	4.9	—		0.19
Fairview	C	n, dx	4	—		3.59
Fontana seismicity	C	u	—	—		0.02
Furnace Creek	C	dx	24	—	$\approx 3^a$	0.10
Garlic Spring	C	u	—	—		0.02
Goldstone Lake	C	u	—	—		0.46
Kern Canyon	C	n	16	—		0.34
Lake Isabella seismicity	C	u	—	—		0.03
Manix Afton Hills	C	sx	12	—		0.08
McLean Lake Drinkwater Lake	C	u	—	—		0.30
Mendocino	C	dx	14.2	—		3.29
Mission Creek	C	dx, r	2	—		0.26
Morales	C	r	25	—		5.19
Nacimiento	C	u	—	—		0.28
Nelson Lake	C	u	—	—		0.12
North Channel	C	r	8.8	—		0.09
North Frontal Thrust, E Zone	C	r	2.9	—		0.12
Oceanside	C	u	—	—	$0-3.2^j$	0.28
Owens Valley, Keough Hot Springs	C	u	—	—		1.60
Palo Colorado	C	dx	8	—		1.75
Paradise	C	u	—	—		0.56
Peralta Hills	C	r	1.3	—		0.15
Pine Mtn	C	r	7.6	—		0.55
Pinto Mtn	C	sx	16	—	$2-5^e,$ $2.6-3.2^i,$ $\approx 9^j$	0.26
Pleasant Valley	C	n	9	—		0.09
Red Pass Lake	C	dx	10	—		0.32
San Gregorio	C	dx	115	—	$\approx 3^e,$ $1.3-3.4^m$	7.59

Fault name	Q	Type	D (km)	Slip-rate (mm/yr)		
				Geologic	Geodetic	Calculated, average
Scodie Lineament	C	u	—	—	—	1.34
Simpson Park Mtn	C	n	8.7	—	—	0.26
Sisar	C	u	—	—	—	0.09
South Cuyama	C	u	—	—	—	0.11
Stateline	C	dx	30	—	—	0.51
Thirty Miles Rivero	C	u	—	—	—	0.26
Upland strikeslip	C	u	—	—	—	0.43
Walnut Creek	C	r	0.3	—	—	0.02
Yorba Linda	C	u	—	—	—	0.09

3.2 Taiwan

The second case study where we have modeled fault strength with SHELLS is Taiwan, as an example of a convergent plate margin. Similarly to California, Taiwan is a densely populated area with significant earthquake hazards. Like California, a dense seismic network has been installed. Over 100,000 earthquakes have been recorded by this network in the past 15 years, and from such a dense record it is possible to determine the geometry of many active faults.

3.2.1 Tectonic Setting

Taiwan is located at the boundary between the Eurasian plate (EU, here consisting of three subplates: Sunda, Yangtze and Okinawa plates, fig. 3.11) and the Philippine Sea plate (PSP). Taiwan is a classic example of oblique arc-continent collision. The Philippines plate is moving towards the northwest relative to the Eurasian plate, which leads to subduction of oceanic crust of the South China Sea (EU) under the Philippines plate, resulting in arc volcanism (Luzon arc). At its northern end, the Luzon arc is in oblique collision with the Eurasian continental margin and active subduction of Eurasia ceases (fig. 3.12). The resulting accretionary wedge, composed of Cenozoic marine sediments, becomes wider and higher from south to north and forms the main part of Taiwan (*Suppe, 1981*). The Coast Range, east of the Longitudinal Valley, does not belong to the wedge, but is an accreted portion of the Luzon arc (*Chang, 2000*) (fig. 3.13). The subaerial accretionary wedge, which forms the upper 10–15 km of crust of the Taiwan orogen, is fully decoupled from the rest of the lithosphere below by the presence of a major detachment that is nearly horizontal in the west, and folds to steeply dipping in the east under the Central Range (*Carena et al., 2002*). The wedge contains many active thrust faults at several levels, which root into the basal detachment at depth.

The oblique collision results in (1) lithospheric folding below the detachment level and, once folding cannot fully absorb convergence any longer, in (2) flipping of subduction polarity (*Carena et al., 2010*). In the north, the Philippines plate subducts under Eurasia along the Ryukyu trench, the Okinawa trough opens, and the Taiwan orogen is no longer active and collapses.

Thus, the main difference with California is the convergent setting with predominantly low-angle thrust faults, compared to the sub-vertical strike-slip faults that dominate California tectonics (fig. 3.4).

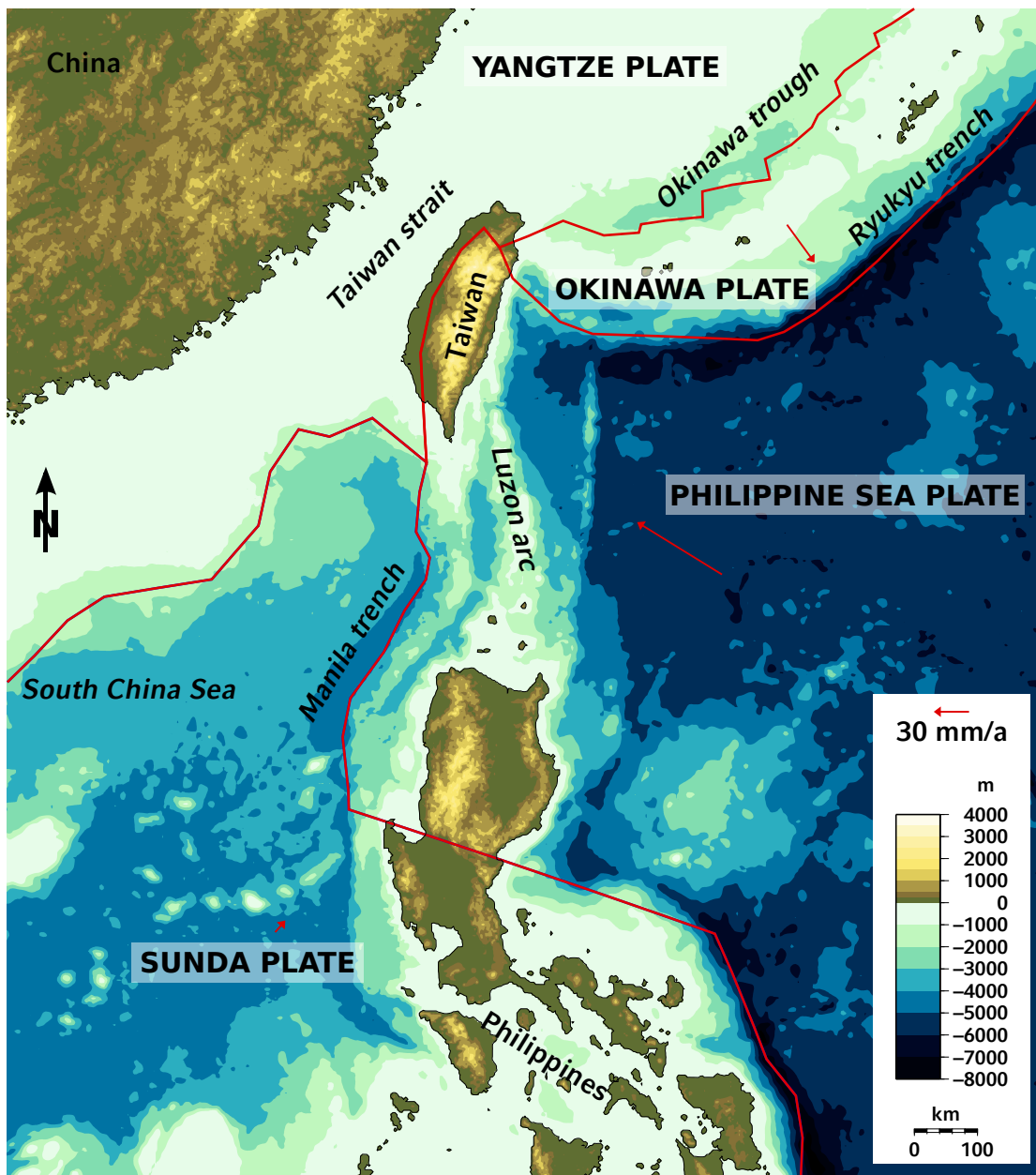


Figure 3.11: Regional map of Taiwan and the northern Philippines. The red lines are plate boundaries, and the red arrows are the velocity vectors (relative to the Yangtze plate) that have been used to drive the model.

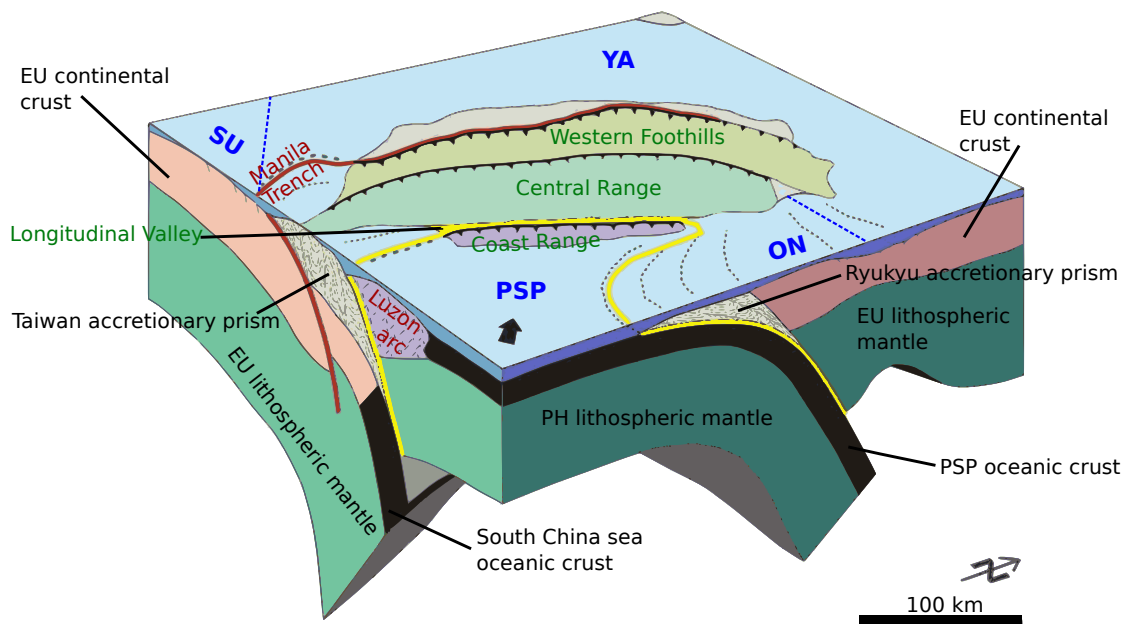


Figure 3.12: Tectonic setting of Taiwan. In the south, the Sunda plate (SU) is being subducted beneath the Philippine Sea plate (PSP) at the Manila trench and produces an accretionary wedge that emerges and forms the island of Taiwan. To the north, the subduction polarity flips, and the Philippine Sea plate is subducted under the Okinawa plate (ON). EU = Eurasia (here either SU, YA or ON). (Modified after *Angelier et al.*, 2001.)

3.2.2 Model Setup

The model setup is largely the same as the one we used for California (see section 3.1.3). We used the same global heat flow data (*International Heat Flow Commission*, 2005), into which we merged the heat flow map of Taiwan from *Lee and Cheng* (1986) for the local area. The topography data is linearly interpolated from the ETOPO1 database (*Amante and Eakins*, 2009) with our ice sheet correction (see section 2.4). The grid is a coarse global grid with a local refinement of the study area. It consists of 2585 nodes and 580 fault elements, 280 of which are located in the Taiwan region (inside the box in fig. 3.14 a).

We have used a more recent version of SHELLS than in our California work (SHELLS release of 2006) mainly because it contains a newer set of plate velocities (PB2002 from *Bird* 2003 instead of NUVEL-1) and revised and more detailed plate boundaries. Whereas both are identical for the California region, the older plate boundaries (*Bird et al.*, 2002) are very coarse in the West Pacific region. In the old version, the boundary between the Eurasian plate and the Philippine Sea plate

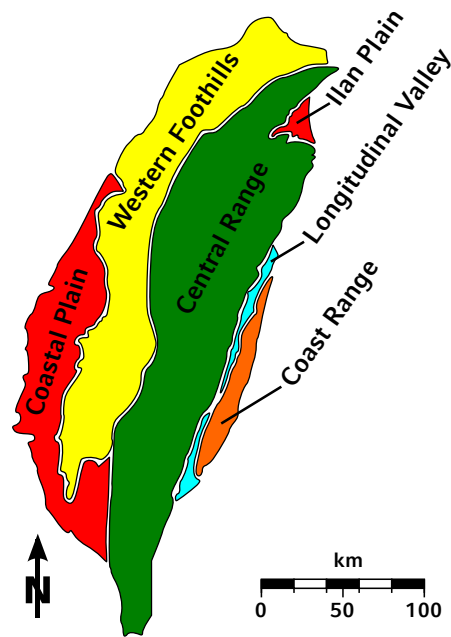


Figure 3.13: Tectonic provinces of Taiwan. The accretionary wedge spans the Western Foothills and Central Range; the Longitudinal Valley is considered the suture zone between the Eurasian and Philippines plates. The Coast Range consists of accreted parts of the Luzon arc. (Modified after *Central Geological Survey, MOEA, 2004*)

is somewhere offshore east of Taiwan, and all local subplates (Sunda, Yangtze, Okinawa) do not exist.

We have integrated into the newer SHELLS version our code extension that lets us assign friction coefficients and creep activation energies to faults individually (see section 2.2). The range of dislocation creep activation energy that we have considered is 100–400 kJ/mol (*Kirby, 1983*), and reasonable fault friction coefficients from independent studies are in the range of 0.1–0.01 (*Carena et al., 2002; Hsu et al., 2009*).

3.2.3 Heat Flow

As mentioned in section 1.3.2, temperature has a nonlinear effect on viscous strength. In SHELLS, the temperature is computed from the surface heat flow, assuming a purely conductive heat transfer. Since the surface temperature is known, the temperature deviations (and hence the exponential effect on viscous strength) increase with depth. The strength of unfaulted rock is dominated by the strength

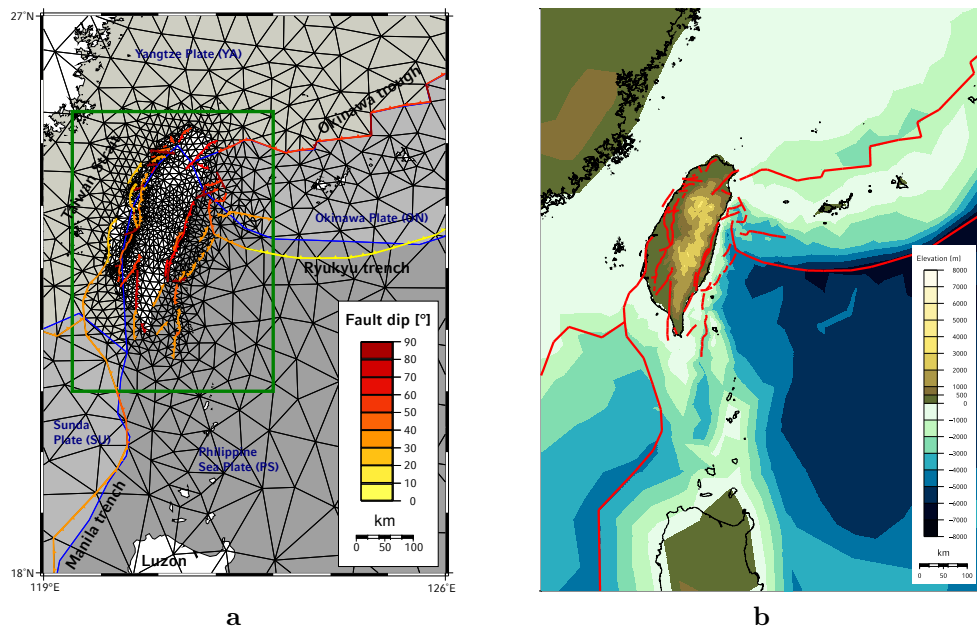


Figure 3.14: **a:** Grid of the study area. The different shades of grey denote the plates of the PB2002 plate model (*Bird, 2003*), plate boundaries are in blue, and faults in colors from yellow to red, indicating their dip angle. The green – white box indicates the area where local conditions (effective friction coefficient μ_i^*) have been applied. **b:** Topography interpolated from the ETOPO1 dataset (*Amante and Eakins, 2009*).

of the uppermost part, so the effect of an inappropriately chosen heat flow is small. Faults, whose strength is determined by their properties near the BDT depth, are instead much more sensitive to errors in the surface heat flow.

The relationship of heat flow and temperature gradient is linear. Thus, an increased surface heat flow together with a constant surface temperature leads to an accordingly elevated temperature at depth. The effect of a non-conductive heat flow is more difficult to quantify. Thermal advection is much more efficient than conduction, so an increase in the surface heat flow due to e.g. hydrothermal mechanisms produces a much higher temperature difference than if only conduction is assumed. As Taiwan does have a significant number of hot springs, a hydrothermal effect on the surface heat flow must be considered. Besides the hydrothermal fluid circulation, there is another factor to take into account in such an active tectonic setting. Due to its tropical climate, Taiwan has one of the highest erosion rates worldwide (*Suppe, 1981*) and, together with the rapid uplift (ca. 5.5 mm/yr in the Central Range, *Li, 1976*), this results in a rapid exhumation of warm crust. The resulting high thermal gradient increases the surface heat flow. However, since

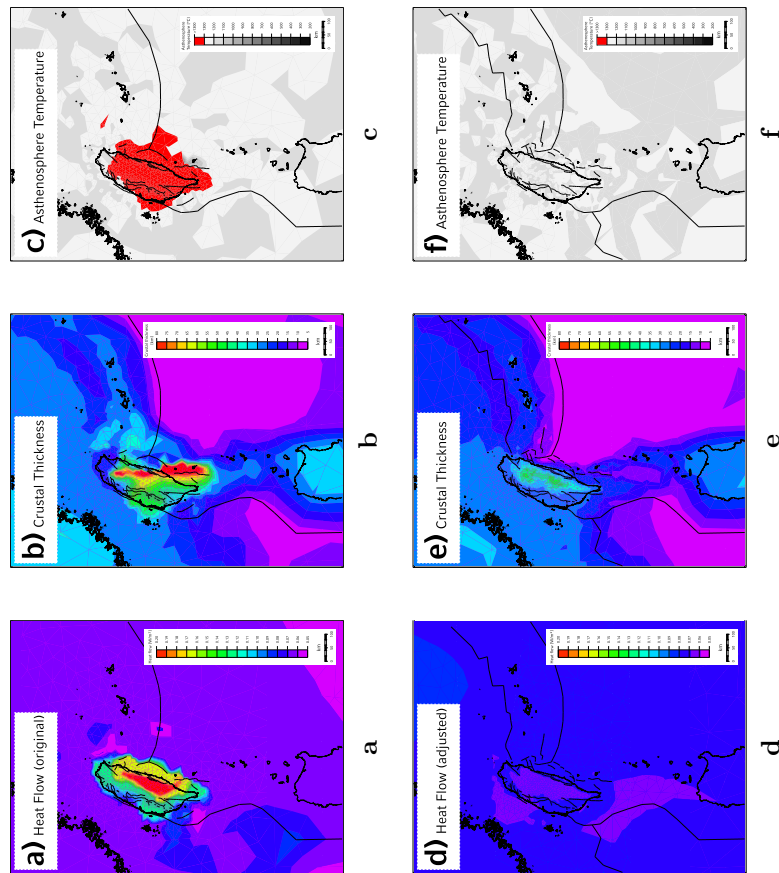


Figure 3.15: Local surface heat flow models for Taiwan: If the heat flow **a** from the measurements of *Lee and Cheng* (1986) is purely conductive, isostatic compensation is not possible: it leads to an unrealistic crustal thickness **b** and an asthenosphere temperature above the liquidus of basalt everywhere below the island **c**. However, if a sensible crustal thickness **e** derived from seismicity and tomography (*Carena et al.*, 2010) is used, the assumptions of isostatic compensation and conductive heat transfer lead to a surface heat flow close to the regional average **d**, and the asthenosphere temperature **f** is not unrealistically elevated at any place.

rapid exhumation only involves the top 10 km of crust at most, high surface heat flow tells us little about the rheology at greater depths.

3.2.4 Fault Strength

Due to the uncertainties in the local heat flow map, we need to be very careful about making sure that all other input parameters are consistent, starting with the global plate motions. For this, we tested different effective friction coefficients at the global level (μ_g^*) while keeping the other parameters fixed (e.g. $Q = 100$ kJ/mol), and compared the velocities of grid points in the center of the major plates with the model driving velocities (computed from the Euler poles of *Bird*, 2003, also at the plate center): modeled velocities should match observed velocities at the Earth's surface. Smaller plates have not been considered, since their plate boundaries are too close — the few grid points in the center are too much influenced by the neighboring plates, so it is not meaningful to compare their motion with rigid plate velocities. The results are shown in fig. 3.16:

- For $\mu_g^* = 0.6$ (Byerlee friction), the plates move much slower than they should: the Pacific plate moves at half of its actual velocity, and most of the other plates (India, Australia, North America, Nazca) almost do not move.
- For $\mu_g^* = 0.1$, most plates move more or less with their expected velocities, except for the Nazca plate, which still does not move.
- For $\mu_g^* = 0.01$, most plates move with their expected velocities, matching both speed and direction. The Nazca plate motion also matches observations and this is in agreement with *Iaffaldano et al.* (2006), who modeled the motion of the Nazca plate and needed to use a similarly low friction coefficient.

The lack of unbiased data is problematic for thermal models of Taiwan. The only original data collection is *Lee and Cheng* (1986), which were originally collected for geothermal energy studies and which we have tried to use for our models. The basic shape of their heat flow map looks reasonable. The isolines of increased heat flow follow the topographic contour lines, which is what rapid uplift and erosion would produce. However, the values are very high, in excess of 240 mW/m², which is not only much more than the average continental heat flow of 65 mW/m² (*Pollack et al.*, 1993), but similar to the values measured at mid-ocean ridges (*Stein and Stein*, 1992), where the thermal gradient is high due to a still-thin lithosphere. The temperatures in a continental lithosphere required for such a high heat flow are far too high. The liquidus for basalt is already reached at 14 km depth (if computed with the same parameters as SHELLS uses) and an isostatic equilibrium is never possible, even after the adjustment of the lithospheric thickness (using the auxiliary

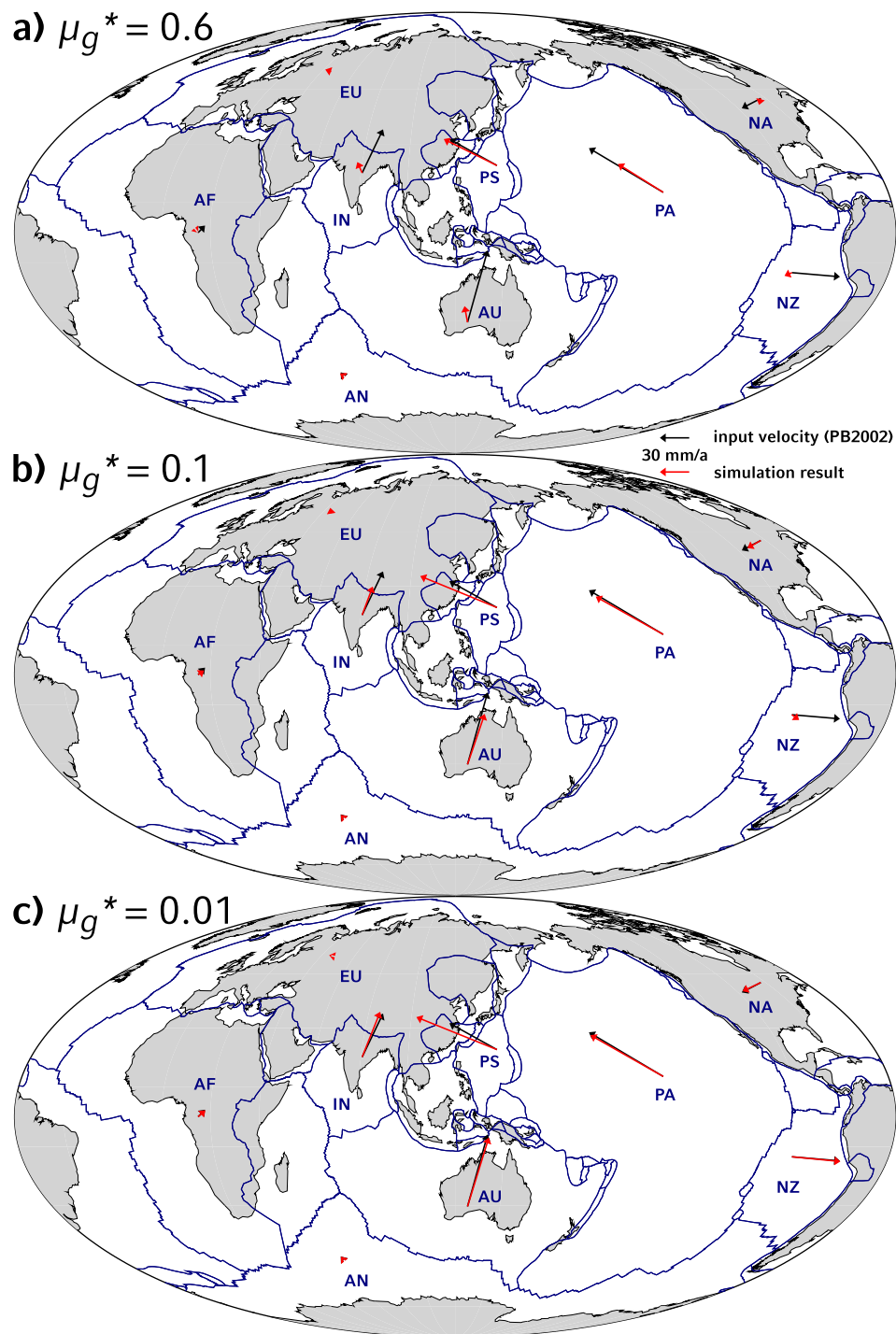


Figure 3.16: Different global effective friction coefficients (μ_g^*) and their effects on the rigid plate velocities of the major plates. The red arrows are the simulation results for grid points in the middle of the plates, and the black arrows are the driving velocities according to the plate model PB2002 (*Bird, 2003*), computed for the same locations. All velocities are relative to the Eurasian plate (EU) and are plotted on the Earth's surface, although driving takes place below the plates.

program *OrbData*). The adjusted grid has a reduced crustal thickness under elevated topography in Taiwan (which is unrealistic) and too high temperatures on the base of the lithosphere, which result in generalized melting (fig. 3.15). So, if a simulation is run in SHELLS, the high vertical excess pressure leads to large landslides at all faults that obliterate any effects of real fault behavior.

This means that the heat flow data from *Lee and Cheng* (1986) is not usable when assuming a purely conductive heat transfer. Although *Lin* (2000) has tried to model this dataset numerically and explain it just with exhumation, the data has been collected as part of a geothermal investigation, and hydrothermal systems likely play a prominent role. In order to avoid creating an unrealistic, unphysical model, we resorted to the inverse method, and computed the surface heat flow from the crust and lithosphere thicknesses, which are today better constrained than the heat flow (*Carena et al.*, 2010).

Next, we examined the local fault strength in terms of effective friction (μ_i^*). The outcome is the same: high friction ($\mu_i^* = 0.6$) prevents motion on most faults, except for some major plate boundaries (fig. 3.17 a). Lower friction (fig. 3.17 b and c) activates the faults in Taiwan, but only a few: most of the plate motion is taken up by the large plate boundary faults (Manila trench, Ryukyu trench) and by internal deformation of the lithosphere. Even at $\mu_i^* = 0.01$ most faults seem to be too strong.

A look at the depth of the brittle–ductile transition in the crust (fig. 3.18 a–c) reveals that the transition depth is unrealistically shallow for most of Taiwan for the conditions used ($Q = 100$ kJ/mol everywhere). The faults should be weaker and the BDT should be deeper. Since the faults are, with $\mu^* = 0.01$, already nearly frictionless, it does not make sense to decrease the friction coefficient further; it is unlikely that small faults are weaker than the large plate boundaries. If we look at strain distribution in the region (fig. 3.19) and compare it to fault slip distribution (fig. 3.17), we notice that the lack of fault motion coincides with a high strain in the continuum. The meaning of this observation is that the surface heat flow, which is virtually impossible to fully correct, results in a continuum that is too weak if its dislocation creep activation energy (Q_c) is assumed to be 100 kJ/mol. It is necessary to make the continuum stiffer in order to transfer more of the deformation to the faults by increasing Q_c . This has been done in the models d–f of figs. 3.17 and 3.18: The global effective friction coefficient has been set to $\mu_g^* = 0.01$ (as determined from the rigid plate velocities in fig. 3.16) and the local friction coefficient to $\mu_i^* = 0.1$. The area of application of local parameters is the box in fig. 3.14 a. If the creep activation energy is increased for both the continuum (Q_c) and the faults (Q_f) to 200 kJ/mol (higher values did not have any significant difference from the 200 kJ/mol case), then the slip rates of large faults decreases

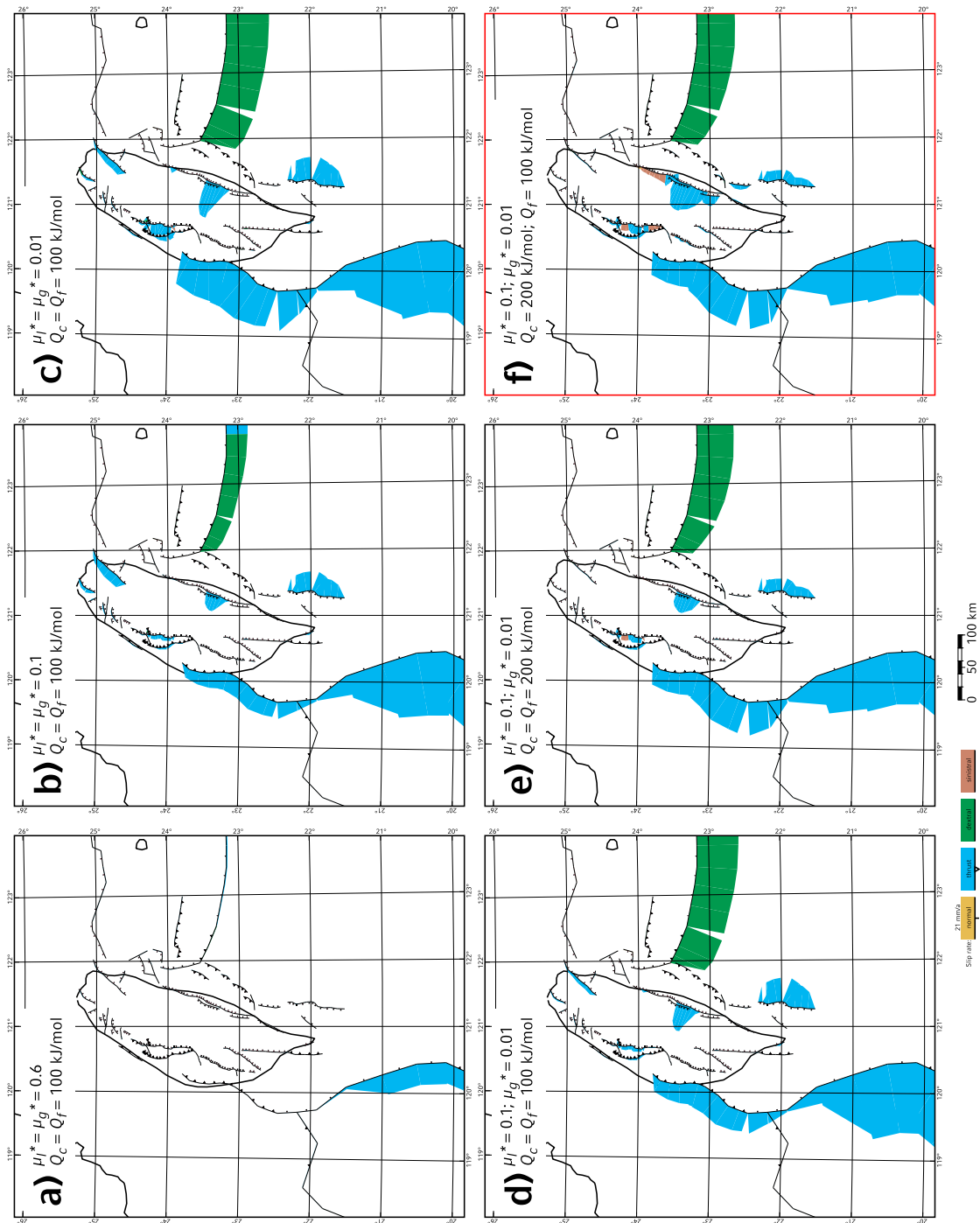


Figure 3.17: Fault slip-rates for different combinations of global (μ_g^*) and local (μ_l^*) effective friction coefficients (varied between a–c) and dislocation creep activation energies (varied between d–e) for the continuum (Q_c) and faults (Q_f). (“Global” and “local” refers to the box in fig. 3.14a.) The best result is figure f, shown in a red box.

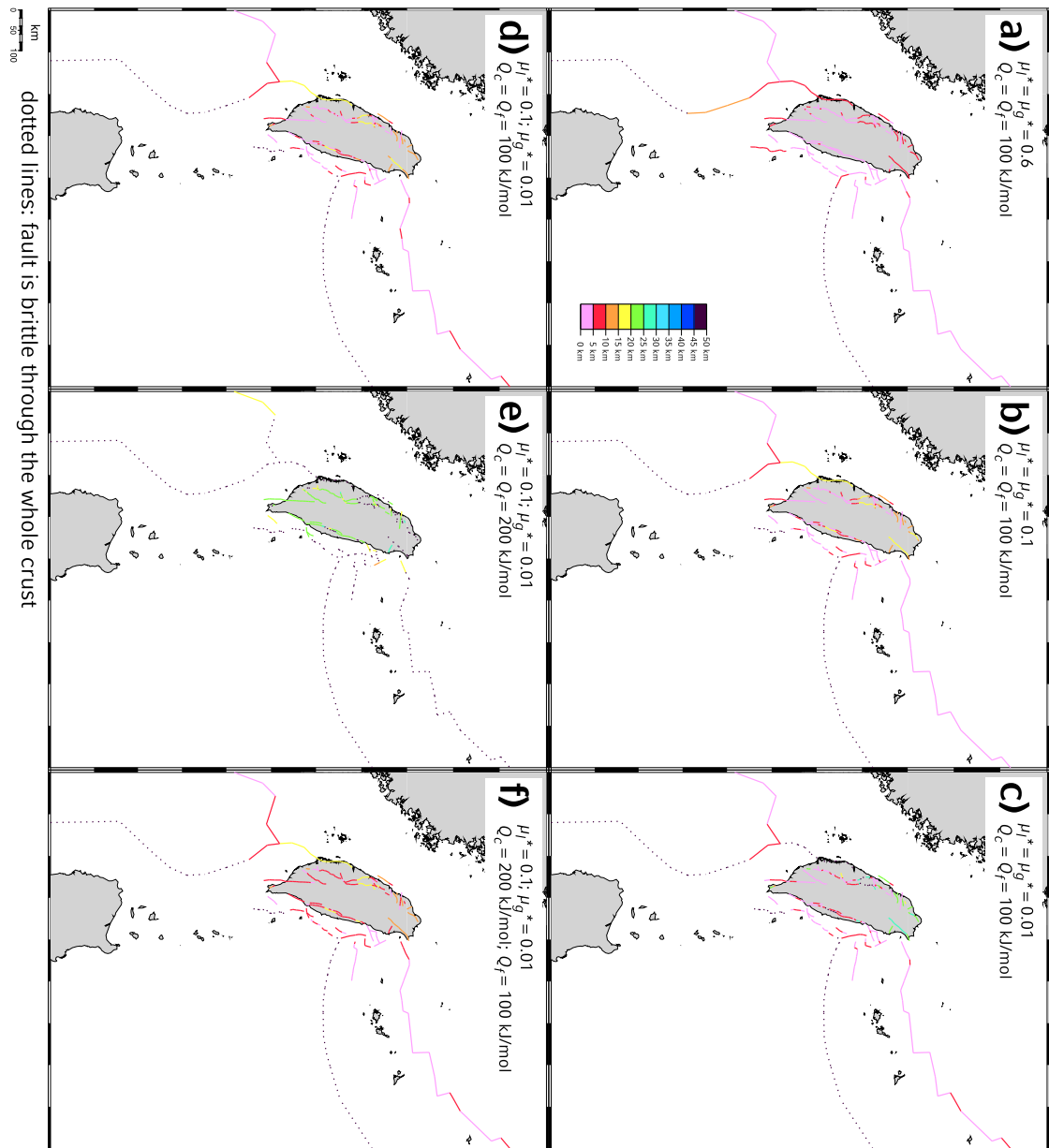


Figure 3.18: brittle–ductile transition depths for the simulations of fig. 3.17. Whereas the main plate boundaries (Manila trench, Ryukyu trench) are brittle throughout the whole crust, the faults in Taiwan require an elevated dislocation-creep activation energy Q_f ; otherwise their BDT is too shallow.

somewhat, but more small faults are activated (fig. 3.17, compare d and e). The brittle–ductile transition however deepens to more than 20 km (fig. 3.18 e), which is a bit too much, considering that most faults here are active seismically only at depths of less than 15 km.

We achieved our best result (fig. 3.17 f) with a small modification to model e. Only the continuum creep activation energy Q_c is set to 200 kJ/mol, the creep activation energy of the faults stays at 100 kJ/mol. This reduces the fault strength, while keeping the continuum stiff. Thus, more faults are activated, while the brittle–ductile transition depth is still reasonable, and these values of Q are also in the reasonable range (*Kirby, 1983*). To summarize:

- The canonical surface heat flow data of Taiwan in *Lee and Cheng (1986)* is not suitable for numerical models of the rheology of the lithosphere, since the measured heat flow does not result from a purely conductive heat transfer in a static equilibrium.
- Global plate motions and local fault slip-rates require effective friction coefficients of $\mu^* \leq 0.1$, i.e. faults are frictionally weak.
- The best simulation results can be achieved when the faults are weaker than their surroundings in the ductile domain as well, i.e. faults have lithospheric-scale extent.

However, there are still some unresolved issues:

- Several faults in Taiwan do not move at all in our simulations. Since the fault slip-rate data for Taiwan are very much incomplete, it is unclear how many of them are indeed active. We have tried to eliminate smaller, poorly constrained faults from our model, but that did not change the general behavior. Also in northern Taiwan, our models do not show any normal faulting in the Okinawa trough region which is instead expected from the extensional nature of the trough.
- The increase in creep activation energy of the continuum simply counteracts the effect of elevated crustal temperature; so a need for a stiffer crust could simply mean that the heat flow we obtain by inverting from crust and lithospheric mantle thickness is still too high.
- It is certainly not correct to assume that the faults in Taiwan maintain constant dip with depth. We tried to modify SHELLS to handle dip changes. This was accomplished by introducing multiple depth-layers corresponding to changes in fault dip. However, since SHELLS often uses gradients to compute depth-dependent properties, it is necessary to change major parts of the program logic. Although a large part of that has been finished, we

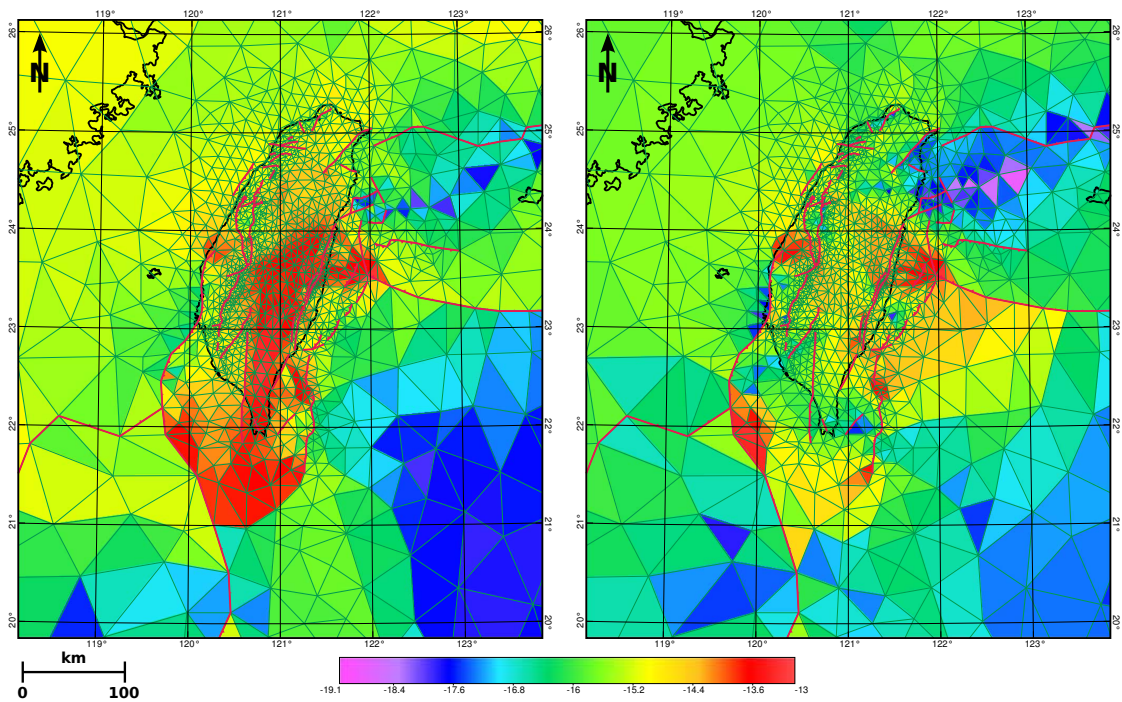


Figure 3.19: Continuum strain rates (unit: $\log(\text{strain}/\text{s})$) of the models d (left hand side) and f (right hand side) from fig. 3.17: Both models have the same fault strength (μ^* and Q_f), but the stiffer crust of model f ($Q_c = 200$ kJ/mol instead of 100 kJ/mol) reduces the continuum deformation in the same way as the slip rates increase in fig. 3.17.

did not manage to get it to work within the time limits. In any case, with the uncertainties in the local surface heat flow, it is questionable whether a more realistic fault geometry would have a major effect on the results in this particular case.

4 Plate Boundaries for Mantle Circulation Simulations

Similar to the lithosphere, the viscosity of the mantle is very high compared to the inertial forces, so its behavior can as well be described as a Newtonian fluid using the Stokes equation. Yet there are differences; the mantle is, due to its convective behavior, much more homogeneous than the lithosphere. And while the lithosphere must be considered as mostly driven from outside — since neither ridge push nor slab pull could explain its motion without any coupling to a circulating system below (*Bird, 1998*) —, the mantle rather drives itself. Its convection can be described by the temperature gradient between its inner and outer surface and the resulting buoyancy differences. This, together with the lack of highly nonlinear processes like fault formation, allows the time-dependent forward modeling of the convecting behavior. An example for such a mantle convection code is TERRA (*Bunge et al., 1997*).

However, to be able to evaluate the convective pattern not only in a qualitative way, but to compare it with observations obtained from e.g. seismic tomography, a correct model of the governing physical laws alone is not enough. The convection history has also an effect: the presence of slabs and plumes causes driving buoyancy forces and advection of heat. Thus, the correct initial conditions are needed in order to model the mantle circulation correctly. However, we do not know anything about the internal state of the mantle at any previous time, but we can observe plate motions, which are surface expressions of mantle circulation, and use this information to adjust the forward model. This technique is called *data assimilation*: in every time step, the corresponding plate velocity field is assigned to the uppermost layer in the mantle (*Bunge et al., 2002*).

Of course, plate motions are also not known for the whole history of the Earth. A physically meaningful period of time that is required for a simulation is given by the convective time scale of the mantle, which is on the order of 100 Ma. At typical mantle velocities of cm per year, subducted slabs can traverse the whole mantle during this amount of time. So the plate motion history must be known for

at least 100 Ma in order to distribute all influences from the surface that can be observed in tomography over the whole mantle.

4.1 From Linear Features to Grid Point Velocities

4.1.1 Plate Reconstruction

The crust is an archive for many marks of past plate motions: the stripe patterns of geomagnetic reversals in oceanic crust, paleolatitudes derived from rock magnetization, hotspot tracks, the distribution of sediments that have formed during the same time period, the position of orogenic belts etc. Being available for all oceanic crust, the magnetic pattern is the most important constraint for plate motion; it allows the computation of relative motion of two adjacent plates that share an uninterrupted magnetic record. A useful reference system for this is the African plate: It is surrounded mostly by passive margins, so the motion of most surrounding plates can be related directly to Africa.

This allows us to reconstruct the motion of Eurasia, India, Antarctica and North and South America relative to Africa, and equally the motion of other plates relative to these — the dependencies between the plates form a tree structure (fig. 4.1). Any plate motion can be related to the reference frame by traversing this tree. There is a problem with this approach for plates like the Pacific plate, since they are surrounded mostly by subduction zones — i.e., there is very little continuous magnetic data that constrains the motion of these plates to the surrounding; so they are related to the hotspot motion rather than to the other continents.

The amount of time that a plate reconstruction can cover in principle is given by the size of an ocean. In the case of a supercontinent, the ocean covers about 70% of the circumference of the Earth, so the distance between the continent and the mid-ocean ridge is on the order of 14,000 km. With an average half-spreading rate — the growth rate on one side of a ridge — of 2.6 cm/a (*Cogné and Humler, 2004*) for the last 180 Ma, the maximum possible age for oceanic crust is 400 Ma. Today, after the break-up of Pangaea, there are three main oceans with ridge systems; this limits the average maximum age of oceanic crust to ca. 140 Ma, which is almost exactly what the maps of ocean floor age of *Müller et al. (2008)* show. Although there are a few places older than that, they are not sufficient to constrain global plate motion models.

This means, plate reconstructions based on the age of oceanic crust are possible back to the early Cretaceous, comprising the break-up of Pangaea. However, with

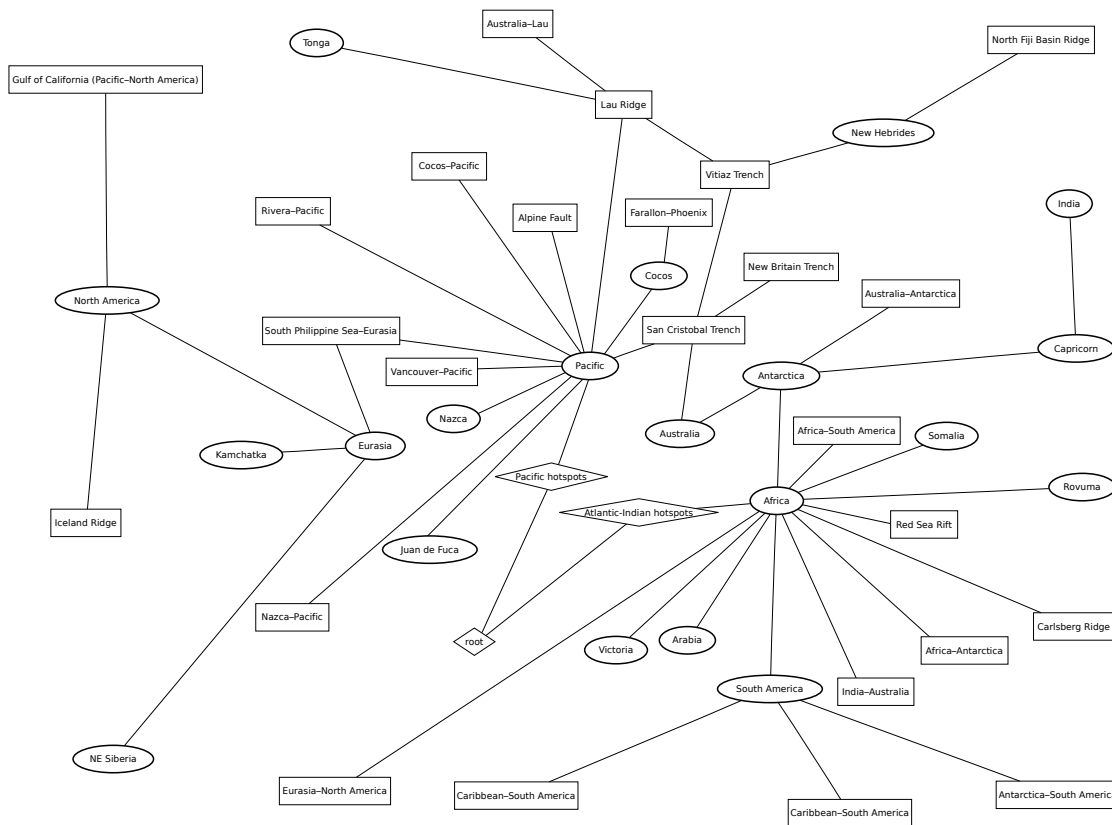


Figure 4.1: Reconstruction tree of the plate reconstruction shown in fig. 4.2, for the present-day plate configuration. Plates are shown as ellipses, ridges and trenches as boxes, and reference frames as diamonds. Only direct relations between two features are shown, the number of indirect relations would be several times higher.

larger uncertainties, plate reconstructions up to 250 Ma are possible (fig. 4.2) — for mantle circulation simulations, a plausible plate model with large uncertainties performs still better than no information about the plate geometry at all.

The open source software *GPlates* (*GPlates development team*, 2010) allows one to reconstruct a self-consistent model of plate motion. This program offers a graphical editor to display and combine all involved datasets, assign single data points to a common entity, compute Euler poles, rotate the plates over time, fill in missing parts, and define the hierarchical reconstruction tree that relates all plate motions to a common reference frame.

GPlates does not deal directly with plate geometries; plate shapes vary over time, this makes a seamless fit difficult. It treats a plate rather as the sum of its bounding objects, such as ridges, trenches, or simple lines that connect those objects. These

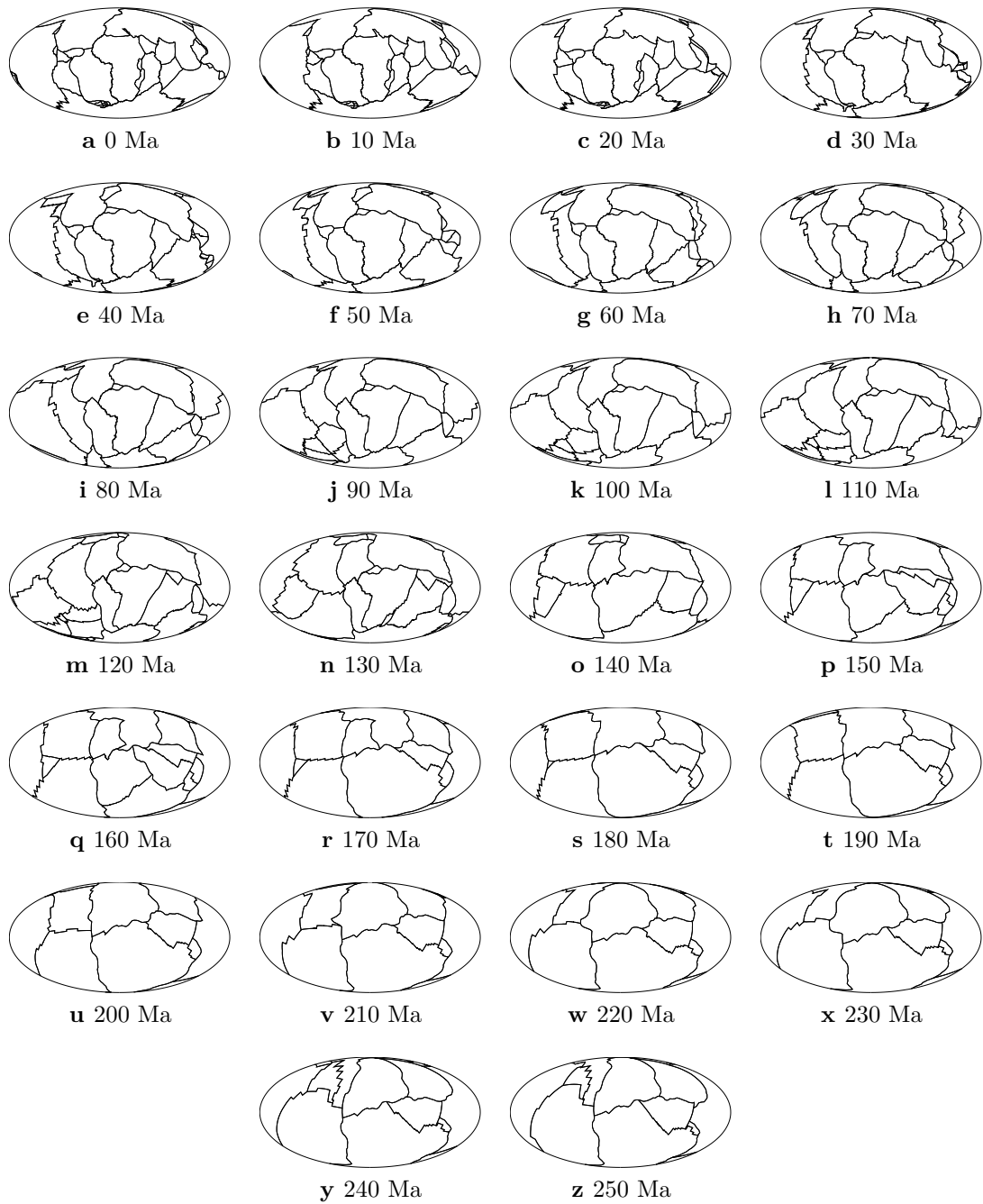


Figure 4.2: Reconstructed plate boundaries over 250 million years. Reference frame: African moving hotspots (0–100 Ma: *O'Neill et al.*, 2005; earlier: *Müller et al.*, 1993)

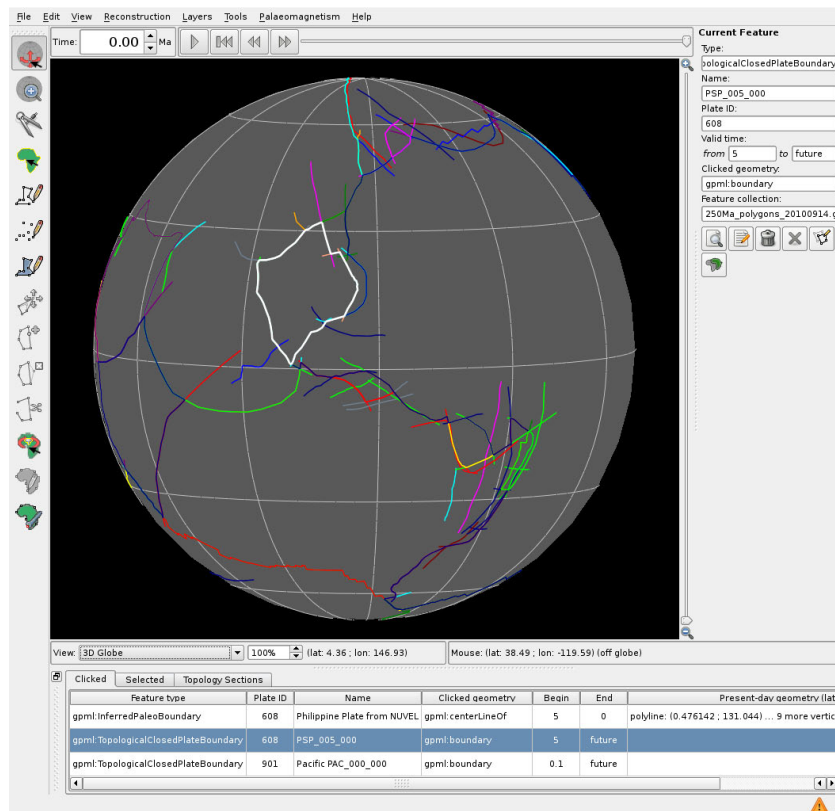


Figure 4.3: Screenshot of GPlates (*GPlates development team, 2010*), showing the Australian and East Asian region. Note the linear features that depict the actual pieces of knowledge about plate boundaries; their intersections form closed plate polygons (example: Philippine Sea plate, highlighted in white) that are used to create the TERRA velocity field.

linear features usually do not form directly the outlines of plates, but rather overlap in many places (fig. 4.3). GPlates connects these overlapping boundaries and creates closed plate polygons for any desired time step.

4.1.2 The TERRA Grid

The grid resolution that a numerical simulation program requires is determined by the size of the smallest structures that have to be resolved. For mantle convection, this is the thickness of the thermal boundary layers, which is in turn controlled by the Rayleigh number. For a viscosity of 10^{21} Pa s a boundary layer thickness in the order of 30 km (thickness of oceanic lithosphere at ridges) must be resolved, and accordingly a similar horizontal distance.

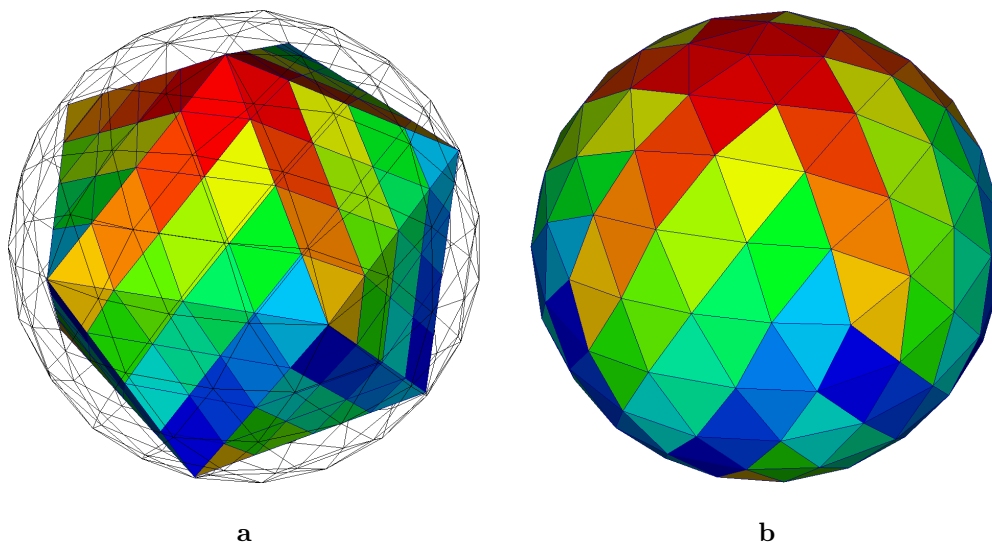


Figure 4.4: Creation of the TERRA grid from a subdivision of the icosahedron: Two adjacent triangles are combined to a diamond and iteratively divided into four smaller diamonds (here: two iterations of bisection, thus diamond edges divided into four pieces, yields 16 cells per diamond). The colors (from red to blue) denote the order of numbering: parallel to one of the diamond edges, starting at the pole. **a:** subdivided icosahedron; **b:** grid points projected onto a sphere.

An equal distribution of grid points on a sphere is generally not possible. Good approximations can be derived from regular polyhedra, i.e. Platonic bodies; a popular example is the *cubed sphere*. A better point distribution can be achieved if the shape of the polyhedron is closer to the sphere. The grid spacing is distorted by the projection onto the sphere; if there are more and thus smaller faces, the difference in distortion between edge and center of the face is smaller, so the grid spacing is more regular.

The Platonic body with the most faces is the icosahedron, from which the TERRA grid is derived. To simplify the subdivision of the grid, pairs of adjacent triangular faces are combined; then the resulting diamonds are iteratively bisected along both axes. The grid points are finally projected onto the circumscribed sphere (fig. 4.4). This grid is simply repeated in the radial direction.

A common subdivision that is used in TERRA divides the diamond edges into 256 pieces; this results in 257^2 grid points in each of the 10 diamonds, in total 660,490 points per spherical layer. The angle subtended by a diamond edge a is $\gamma = \arccos((a^2 - 2r^2)/(-2r^2)) = 63.4^\circ$ (law of cosines), so the length of the spherical arc on the circumscribed sphere is 7054 km, and thus the minimal distance between

grid points 27.6 km. The maximal grid point distance is 13% larger (length of the arc over half edge, multiplied by ratio of the radii of circumscribed sphere to midsphere), i.e. 31.1 km.

4.1.3 Plate Polygons and Grid Points

The plate velocity at any grid point can easily be obtained by multiplying the coordinates of the grid point with the Euler vector of the corresponding plate. However, it is challenging to find out to which plate a grid point belongs. GPlates generates plate polygons; to test whether a grid point lies within a given polygon is a frequent problem in computer graphics, and there are several standard approaches available (*Haines*, 1994):

- **Ray casting:** A line from the point being examined to infinity (or further away than any polygon point) is drawn, and the number of intersections with the polygon is counted. If the number is even (or zero), the point is outside the polygon; otherwise, the point is inside (fig. 4.5 a).
- **Winding number:** The angles that subtend the polygon edges with vertex at the grid point are summed up. If the grid point is inside the polygon, the legs of the angles circle the grid point, so the angle sum is $\pm 360^\circ$ (fig. 4.5 c). If the grid point is outside, the legs of the angles move back and forth on one side of the grid point, thus the angles have opposite signs and cancel out; the angle sum is 0° (fig. 4.5 d).
- **Subdivision:** Any polygon can be subdivided into triangles, which are much easier to test than the large and possibly concave polygon. Only a series of comparisons is needed: if a grid point lies on the correct side of all three triangle edges, then it lies inside the triangle (fig. 4.5 b).

These algorithms are fairly simple and there exist numerous tools and source code for the problem in 2D cartesian coordinates. For the 3D case, there is very little software available; but the main problem is that a polygon on a sphere does not lie in a plane. Thus, there is no ready-made software available for this problem. We found some implementations in the source code of programs used in the Earth sciences, but none of them worked reliably:

- The OGR library (used e.g. by Quantum GIS) offers such a functionality; it turned out that it is very fast, but had problems with plates spanning over the date line. Even splitting the polygons into parts belonging to either the western or eastern hemisphere did not help. Obviously this library is only suited for applications where the scope is not global.

- An implementation of the winding number algorithm is used in SHELLS. It is complicated since it projects the grid point and the polygon onto a plane before computing the angles. Although it seems to work fine with the coarse present-day plate boundaries PB2002 (*Bird, 2003*), it failed at some of the plate polygons exported from GPlates, which requires laborious manual corrections.
- We have also dealt with an implementation of the ray casting algorithm; it draws a great circle arc from the grid point to one of the poles. For this, the program needs to know which plates contain the poles, which requires manual work. Additionally, the implementation has numerical problems, so there are sometimes artifacts that require a lot of manual corrections.

We finally found the most reliable code in the GPlates code itself. The current releases of GPlates can neither read nor write unstructured grids like the TERRA grid; it was extremely cumbersome to get the grid data into GPlates, so it turned out to be easier to extract the algorithm from GPlates and implement a stand-alone program. GPlates uses a combination of the ray casting and the winding number algorithms:

- First, it tests whether the polygon contains one of the poles, using a variant of the winding number algorithm: with the pole at its vertex, the angle between two polygon points is simply their difference in longitude; no expensive projections and vector functions are needed. If the pole is inside the plate, the angle sum is $\pm 360^\circ$, otherwise 0° .
- If the polygon contains a pole and the grid point latitude is closer to the pole than any of the polygon points, the point is inside the plate. Likewise, if the grid point latitude is further away than any of the polygon points, it is certainly outside.
- Otherwise, if the polygon does not contain a pole, a variant of the ray casting algorithm is used. It computes the intersections of all polygon edges with the meridian through the grid point. If the number of intersections is even and the polygon does not contain any of the poles, which are the endpoints of the test meridian, the point must be inside the plate, otherwise outside. If one of the poles is inside the plate, there is always one intersection less, so an odd number of intersections implies the point being inside.

This algorithm failed only for plates containing both poles — i.e. Pangaea. To cover this case, we split the plates into parts belonging either to the northern or southern hemisphere. After that, the program worked in all cases reliably, no manual editing was needed.

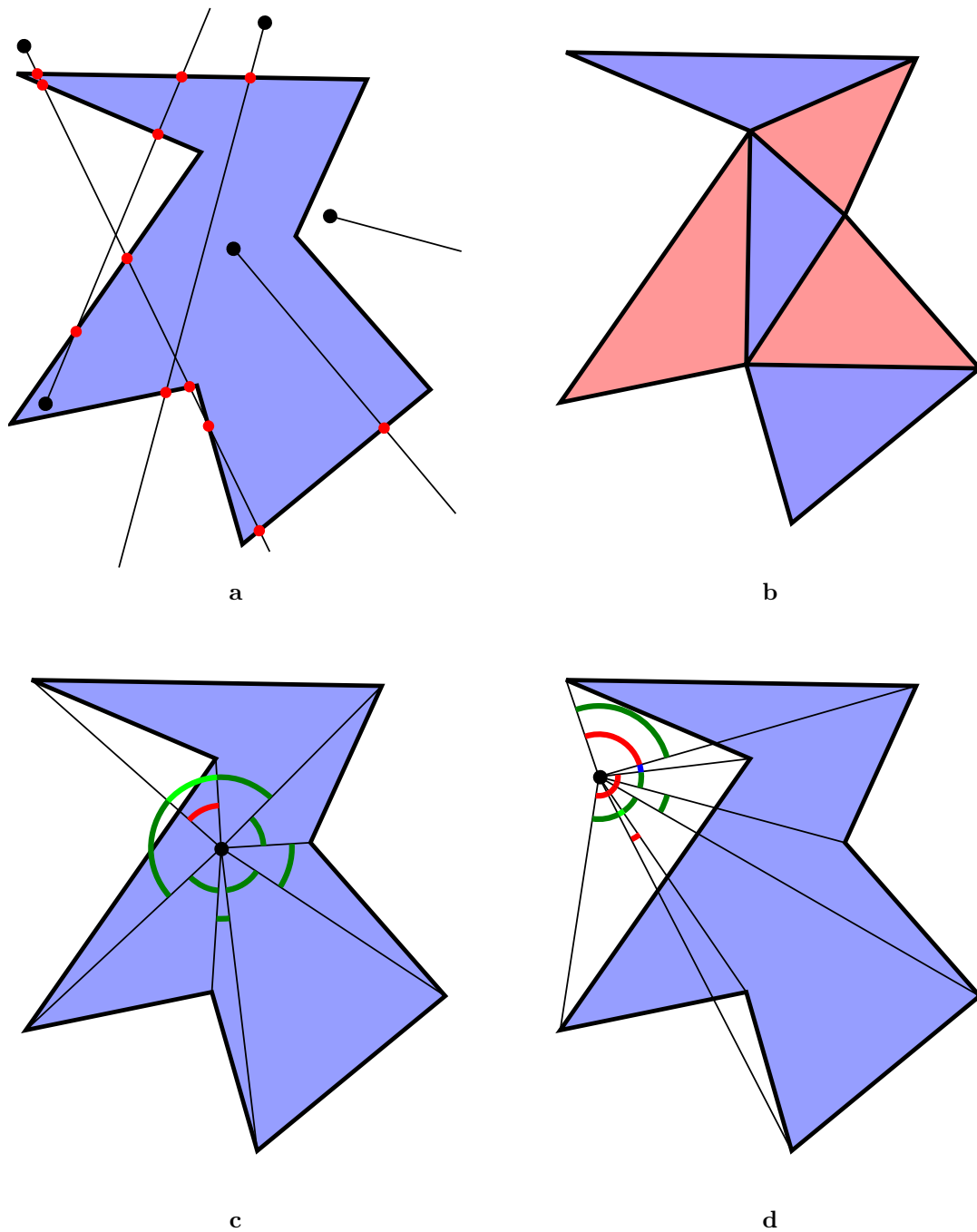


Figure 4.5: Three different point-in-polygon testing algorithms. **a:** ray casting; rays starting from outside the polygon have an even number of intersections (marked by red dots) with polygon edges (or none at all), rays starting from inside have an odd number of intersections. **b:** triangulation. **c, d:** winding number algorithm; if the point is inside, the angles between adjacent vertices add up to $\pm 360^\circ$ (opposite directions shown in red and green, the light green arc is counted twice, it cancels out with the red arc); if the point is outside, the angle sum is 0° (red and green cancel out; light green: twice in same direction; blue: twice in opposite direction).

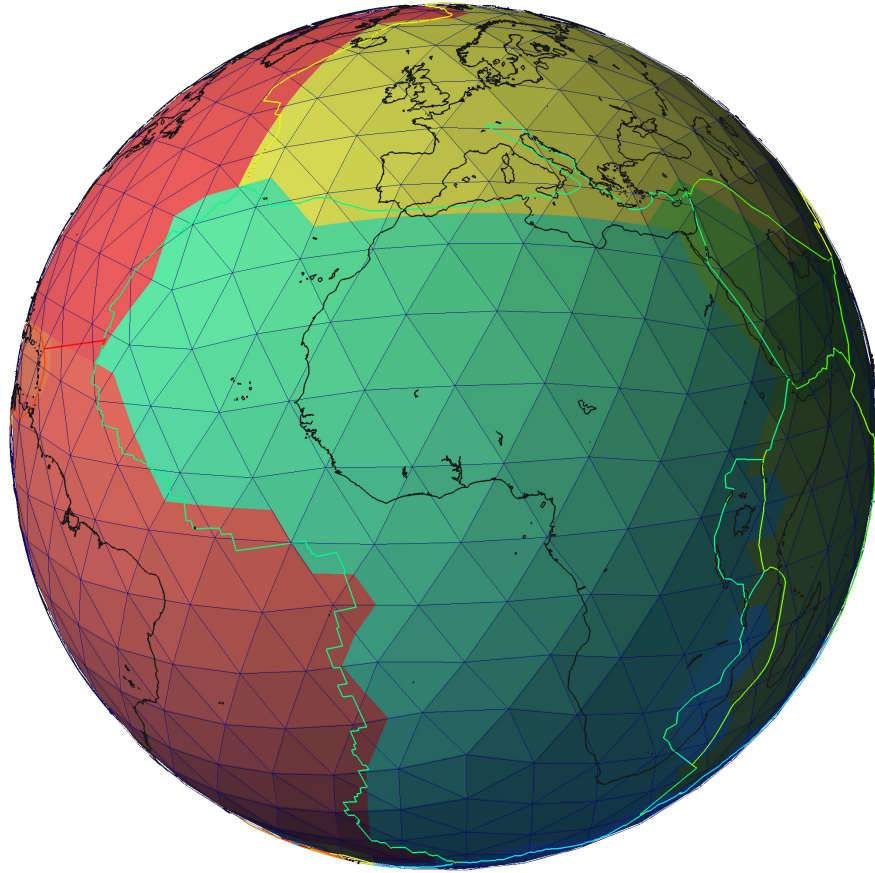


Figure 4.6: Plate polygons and TERRA grid (with $NT = 8$ subdivisions of the icosahedral edges) for the present-day plate configuration.

4.1.4 Performance Issues

Although the computation of such plate maps is not time-critical, especially when compared to the time-consuming tasks of creating plate configuration scenarios and running mantle circulation simulations, the performance is still important. For example, a grid derived from the subdivision of the icosahedral edges into 256 pieces contains 660,490 grid points per radial layer, and a typical plate reconstruction involves 250 time steps and in average 15 plates per time step. If half of the plates must be tested on average, this yields more than 1.2 billion point – polygon tests. In order to do this over night, roughly 80,000 polygons must be tested per second. The point-in-polygon algorithm described above uses only simple arithmetic operations and comparisons, so there would be no benefit from using a numerical library. For comparison, the winding number algorithm used by SHELLS is computationally

much more expensive due to several vector multiplications; on the other hand, the number of grid nodes in SHELLS is limited by the size of the stiffness matrix to several ten thousands, not billions, so it works reasonably well there. We applied the following optimizations to our code:

- Mostly, successive grid points are adjacent (fig. 4.4); so it is sensible to test the plate of the previous grid point first. With the grid resolution of the example above, more than 99% of the grid points belonged indeed to the same plate as their predecessors, increasing the program speed by a factor of 7.
- If this is not the case, polygons with many edges are tested first. Although a high number of edges need not coincide with a large plate area and hence a higher probability to contain the grid point, it is still more likely.
- Only those plates are considered whose bounding boxes contain the grid point.

The program is written in the scripting language Perl (see listing C.1) and needs ca. 12 min per plate map on a state-of-the-art PC. A wrapper script (see listing C.2) remaps GPlate's three-digit plate numbers to sequential numbers needed by TERRA and starts a process on every CPU core of the computer. A set of 250 time steps can thus be converted in less than three hours on a server with 16 CPU cores.

4.2 Application: Mantle Circulation Model¹

We have run a series of mantle circulation models with a sequence of reconstructed plate configurations as boundary conditions. The plate boundaries are taken from the older reconstructions of *Lithgow-Bertelloni and Richards (1998)*, which exist only as polygons for a few time steps. In the absence of GPlates, we have created linear interpolations between these polygons in order to get a finer time stepping, and then used the method described in the previous sections to create plate maps. We have then investigated the resulting temperature distribution in the mantle, and we have used a mineralogical model in order to convert temperatures to seismic velocities. This allows a comparison with tomographic data.

4.2.1 Introduction

Seismic tomography has advanced to a point where it provides considerable insight into the structure of the deep Earth. Particularly important for our understanding of deep Earth processes are two robust features of lower mantle heterogeneity (see Figure 4.7): One is a long wavelength fast seismic velocity anomaly concentrated into the circum-Pacific and regions under Asia (e.g., *Li and Romanowicz, 1996; Masters et al., 1996; Grand et al., 1997; van der Hilst et al., 1997; Su and Dziewonski, 1997; Kennett et al., 1998; Masters et al., 2000; Ritsema and van Heijst, 2000, 2002; Montelli et al., 2004, 2006*). It is now widely agreed upon by geodynamicists that this feature is associated with cold downwellings from past subduction driving a substantial part of the mantle general circulation (*Richards and Engebretson, 1992; Bunge et al., 1998; Lithgow-Bertelloni and Richards, 1998; Becker and O'Connell, 2001; Conrad and Lithgow-Bertelloni, 2002; McNamara et al., 2002*).

Less certain is the origin of another feature consisting of two pronounced low seismic velocity anomalies located beneath the Pacific and under Africa. Hot buoyant mantle from a strong thermal boundary layer at the core-mantle boundary (CMB) would provide a straightforward explanation for these anomalies. However, several studies argue that these regions are characterized by a different bulk composition from the surrounding mantle (*Ritsema et al., 1999; Ishii and Tromp, 1999, 2001; van der Hilst and Karason, 1999; Wen et al., 2001; Ni et al., 2002; Ni and Helmberger, 2003; Ritsema and van Heijst, 2002; Deschamps and Trampert,*

¹Parts of this section have been published as: Schubert, B. S. A., H. P. Bunge, G. Steinle-Neumann, C. Moder, and J. Oeser (2009), Thermal versus elastic heterogeneity in high-resolution mantle circulation models with pyrolite composition: High plume excess temperatures in the lowermost mantle, *Geochem. Geophys. Geosyst.*, 10(1), Q01W01, doi:10.1029/2008GC002235

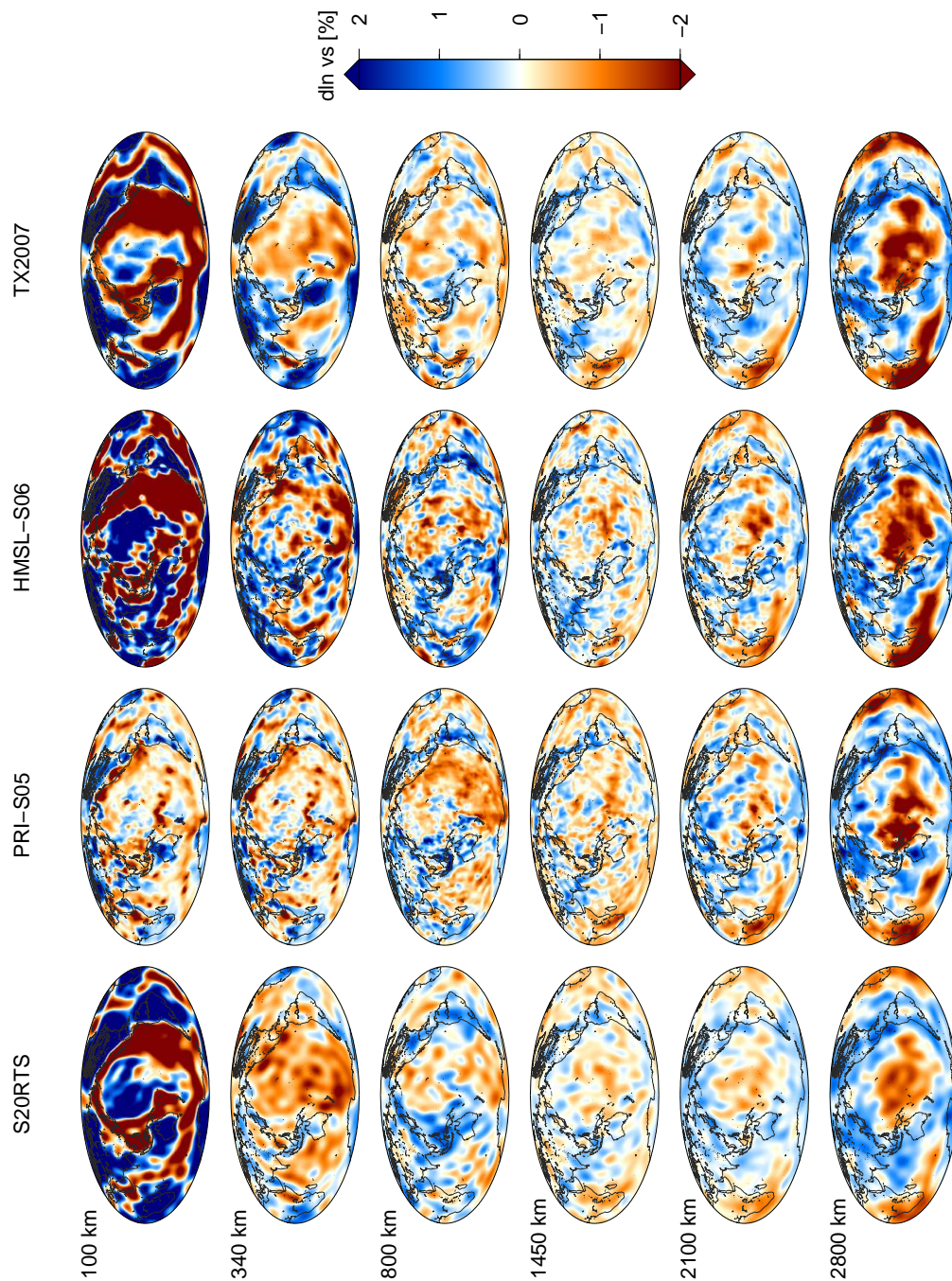


Figure 4.7: Depth slices through tomographic mantle models of shear wave velocity S20RTS (*Ritsema et al.*, 2004), PRI-S05 (*Montelli et al.*, 2006), HMSL-S06 (*Houser et al.*, 2008), TX2007 (*Simmons et al.*, 2007). Variations in S-wave velocity are given relative to each corresponding 1-D radial seismic reference model. The color scale ranges from -2% to $+2\%$ as shown on the right. Heterogeneity is strongest in the lithosphere, the upper mantle and near the CMB. Note the dynamically important slow seismic velocity structures located under the Pacific and Africa in lowermost mantle (called “Large Low Velocity Provinces” or “superplumes”) and the ring of fast velocities around the Pacific.

2003; Wang and Wen, 2004). Supporting evidence for this comes from probabilistic models of mantle heterogeneity (Resovsky and Trampert, 2003; Trampert et al., 2004), and from seismic studies that simultaneously map the pattern of bulk sound and shear wave velocities (Kennett et al., 1998; Masters et al., 2000).

The complex character of the low seismic velocity anomalies has prompted geodynamicists to investigate the behavior of mantle flow with compositional variations (e.g., Christensen and Hofmann, 1994; Davaille, 1999; Kellogg et al., 1999; Tackley, 2000, 2002), and to illuminate the dynamic consequences of a dense component in the deep mantle (Hansen and Yuen, 1989, 1994, 2000; Montague and Kellogg, 2000; Davaille et al., 2002; Stegman et al., 2002; Jellinek and Manga, 2004; Nakagawa and Tackley, 2004; McNamara and Zhong, 2004, 2005; Farnetani and Samuel, 2005).

Equally important for our understanding of these anomalies is the thermal state of the mantle, which is complicated by the simultaneous presence of mixed heating modes, i.e., by the effects of internal heating from radioactive decay and bottom heating from the core. The subadiabatic nature of the mantle geotherm away from thermal boundary layers is a direct consequence of internal heating, as noted early on by Jeanloz and Morris (1987), and there is growing consensus that the mantle geotherm departs by as much as 300–500 K from the adiabat (Matyska and Yuen, 2000; Bunge et al., 2001; Monnereau and Yuen, 2002; Sleep, 2003).

Mantle non-adiabaticity points to a strong thermal gradient and a correspondingly high heat flux across the CMB (Bunge, 2005; Mittelstaedt and Tackley, 2006; Zhong, 2006; Lay, 2008), as large as 30 percent (~ 10 TW) of the total mantle heat loss. Thus, it is likely that bottom heating plays a more prominent role in the mantle general circulation than what is commonly inferred from arguments based on the dynamic topography over hotspots (Davies, 1988; Sleep, 1990). It is therefore important to study the nature of heterogeneity in global mantle circulation models (MCM) when strong core heating is present. Of course, mantle heterogeneity modeled by geodynamicists must be compared to the seismic properties mapped by tomography. Both are related through the material properties of mantle mineralogy. In this respect, however, interpretations have remained limited as the trade-offs between thermal and chemical effects have not allowed an unequivocal identification of the cause of heterogeneities both for the upper (Cammarano et al., 2003) and the lower mantle (Deschamps and Trampert, 2004; Mattern et al., 2005; Matas et al., 2007).

In this study, we test in a forward modeling approach whether strong core heating results in seismic heterogeneity compatible to observations in spectral characteristics and magnitude. To keep things simple, and to isolate the effects of core heating, we

focus our attention on isochemical global mantle circulation. The pyrolite model (Ringwood, 1975; Irifune, 1987) is consistent with this choice.

We start this paper with a brief description of the computational methods and parameters employed. We next investigate the thermal heterogeneity of mantle flow with a substantial amount of core heat flux (as much as 12 TW), and isolate the effects of core heating from variations in the radial viscosity profile through simple end-member models. We explore the influence of thermal structure on corresponding heterogeneities in shear (v_s) and compressional (v_p) wave velocity, which we compare to tomographic models directly and with statistical measures. For the conversion of temperatures into elastic parameters we take advantage of progress in mineral physics and use two recently published thermodynamic models of mantle mineralogy (Piazzoni *et al.*, 2007; Stixrude and Lithgow-Bertelloni, 2007), coupled to a model of shear moduli (Stixrude and Lithgow-Bertelloni, 2005). In both models, stable phase assemblages in the CFMAS (CaO – FeO – MgO – Al₂O₃ – SiO₂) system are computed by Gibbs Free Energy minimization. We refer to these models hereafter as PSBD and SLB, respectively.

In the analysis of seismic properties and their relation to temperature via a mantle mineralogy model one needs to pay special attention to the vigor of convection, as one must ensure that modeled temperature variations are consistent with temperature variations assumed in the underlying mineralogy. To this end, we capitalize on growing computational resources and employ new global mantle circulation models at very high numerical resolution. This allows us to approach for the first time the vigorous regime of global mantle flow and to construct its corresponding elastic structure. Our models do not preclude the existence of chemical variations, but they suggest that the large-scale elastic heterogeneity of the mantle can be understood in terms of isochemical whole mantle circulation with strong hot upwellings from the CMB.

4.2.2 Computational Methods, Boundary and Initial Conditions

We compute global mantle flow with the parallel finite element code TERRA, which has been benchmarked (Bunge, 1996) and described in detail before (Bunge and Baumgardner, 1995; Bunge *et al.*, 1996, 1997). The code solves the momentum and energy balance at infinite Prandtl number (no inertial forces) in a spherical shell, with the inner radius being that of the outer core and the outer radius corresponding to Earth's surface. The computational domain is discretized with a mesh derived from the regular icosahedron, providing almost equidistant grid

spacing throughout the mantle. A key difference to earlier studies (e.g., *Bunge et al.*, 2002) is the very high resolution of the mesh with more than 80 million finite elements. The models are implemented on 128 cores of a topical compute cluster dedicated to large-scale geophysical modeling (*Oeser et al.*, 2006). The horizontal resolution is 30 km at the outer surface, and decreases to half that value at the CMB, while a uniform radial grid spacing of 25 km is applied throughout the shell. This fine discretization allows us to explore large-scale mantle flow at earth-like convective vigor and to employ a thermal Rayleigh number of 10^9 based on internal heating; that is, we are able to resolve a characteristic thermal boundary layer thickness on the order of 100 km, comparable to that of oceanic lithosphere.

Our circulation models incorporate mantle compressibility effects in form of the anelastic liquid approximation (*Jarvis and McKenzie*, 1980; *Glatzmaier*, 1988), and the radial variation of state variables is represented through a Murnaghan equation of state (*Murnaghan*, 1951) with parameter values identical to (*Bunge et al.*, 2002). We apply a thermal conductivity of $3.0 \text{ W m}^{-1} \text{ K}^{-1}$ and an internal heating rate of $6.0 \times 10^{-12} \text{ W kg}^{-1}$ throughout this study, roughly the chondritic value (*Urey*, 1956). Thermal boundary conditions are constant temperature at the surface (300 K) and the CMB. The latter is chosen such as to produce models with weak or strong core heat flux (see section 4.2.2). Mechanical boundary conditions are always free-slip (no shear-stress) at the CMB, while velocities are specified at the surface according to a widely adopted plate motion history model (*Lithgow-Bertelloni and Richards*, 1998) that spans the past 120 million years (Ma). Meteorologists refer to this approach as *sequential* data-assimilation (see *Talagrand*, 1997, for a review).

The high numerical resolution in our models requires an interpolation of all plate boundaries between successive plate stages, similar to *Steinberger* (2000), to avoid unrealistic separation of slab fragments. The interpolation is performed at 1 Ma intervals and involves geometric, but no geologic considerations. For this, we created a set of 120 plate configurations based on the eleven plate stages of *Lithgow-Bertelloni and Richards* (1998) while keeping their corresponding set of eleven Euler poles.

The large convective vigor in our models has the effect that the RMS surface velocity obtained from an independent set of free convection simulations (with no imposed plate motion) approaches earth-like values (about 5 cm/yr). This remarkable observation allows us to keep time identical to Earth time in all simulations, and to avoid scaling the assimilated plate velocities to lower values.

A general problem in mantle circulation modeling is the choice of an initial condition. This choice is rather arbitrary, as the structure of the mantle sometime in the past is principally unknown. Here, we follow the philosophy of *Bunge et al.* (1998,

2002) and approximate the unknown initial conditions of mid-Cretaceous mantle heterogeneity by running our models with global plate configurations fixed to the oldest available reconstructions at 120 Ma ago until they reach a thermal quasi steady-state.

Finally, the temperature field of the MCMs is post-processed and mapped to seismic velocities using the two thermodynamically self-consistent models of mantle mineralogy, PSBD and SLB, mentioned in section 4.2.1. In this simple approach, phase transitions of upper mantle minerals are therefore incorporated in our elastic models, even though their dynamic effects on the flow are not included in the calculations.

Model Setup

We focus on four mantle circulation models (M1 – M4) and explore variations in the amount of bottom heating and the radial viscosity structure, while keeping all other model parameters constant (see Table 4.1). Our radial viscosity profiles account for three distinct layers (which we identify with the lithosphere, the upper and the lower mantle, respectively) separated at 100 km and 660 km depth. These are inferred from geoid (e.g., *Hager and Richards*, 1989) and post glacial rebound studies (*Paulson et al.*, 2007) as a first-order rheological stratification of Earth’s mantle. Each model includes a relatively strong lithosphere, where the viscosity is 10^{23} Pa.s. The upper mantle viscosity in model M1 is 10^{21} Pa.s, the Haskell value (see *Mitrovica*, 1996), and increases by a factor of 100 in the lower mantle. We ease the notation and index our model viscosities to the Haskell value, which we denote as “1”. Thus, the viscosity profile of M1 is 100, 1, 100 for the lithosphere, the upper and the lower mantle, respectively. A modest CMB heat flux of 1.5 TW (around 5% of the total surface heat flow) is accomplished by setting the CMB temperature to 2900 K.

The viscosity profile of M2 is identical to M1, but we impose a much higher core heat flux of 12 TW (roughly 35% of the surface heat flow) by setting the CMB temperature to 4200 K. This makes M1 and M2 end-members in terms of core heating with Urey numbers (the ratio of internal heating to total surface heat loss) of 0.95 and 0.65, respectively. M3, to which we ascribe a viscosity profile of 100, 0.5, 100, in effect explores the influence of a mechanically weaker upper mantle (relative to M1 and M2) and a correspondingly higher upper/lower mantle viscosity jump. A core heat flow of 9 TW (roughly 25% of the surface heat flow) is accomplished by setting the CMB temperature to 4000 K. M4 (with a profile of 100, 0.5, 50) reduces the overall mantle viscosity relative to M1, and moves the upper/lower mantle viscosity jump to 450 km depth. The depth and magnitude of the viscosity

Table 4.1: Physical parameters and values employed in the simulations of mantle circulation. Values in this table were kept constant in all four mantle circulation models M1–M4.

outer shell radius	6370	km
inner shell radius	3480	km
T_{Surface}	300	K
η_{ref} (reference viscosity)	1.0×10^{21}	Pa s
thermal conductivity k	3.0	$\text{W m}^{-1} \text{K}^{-1}$
thermal expansivity α (surface)	4.011×10^{-5}	K^{-1}
thermal expansivity α (CMB)	1.256×10^{-5}	K^{-1}
internal heating rate Q_{int}	6.0×10^{-12}	W kg^{-1}
heat capacity	1.134×10^3	$\text{J kg}^{-1} \text{K}^{-1}$
Ra_H (based on η upper mantle)	$\simeq 10^9$	

Table 4.2: Variable parameters and respective values in models M1–M4. Viscosities in the lithosphere (LI), upper mantle (UM) and lower mantle (LM) are indexed to the reference viscosity of $\eta_{\text{ref}} = 1 \times 10^{21}$ Pa s.

Model	Viscosity structure LI/UM/LM w.r.t η_{ref}			Depth of UM/LM boundary [km]	T_{CMB} [K]	CMB heat flow [TW] (% of surface heat flow)
M1	100	1	100	660	2900	1.5 (5)
M2	100	1	100	660	4200	12 (35)
M3	100	0.5	100	660	4000	9 (25)
M4	100	0.5	50	450	3500	10 (30)

contrast between upper and lower mantle is not well known. We therefore chose to test a shallower depth in combination with the reduced overall viscosity in M4. A core heat flux of 10 TW (around 30% of the surface value) results from a CMB temperature of 3500 K in this case. Note that M4 produces a heat flow comparable to M2 and M3 despite its lower CMB temperature. This is a consequence of the reduced viscosity and the correspondingly more vigorous convection in this model. Together, M1–M4 span a reasonable range of mantle viscosity and core heat flux values, which are summarized in Table 4.2.

4.2.3 Results

Lateral Thermal Heterogeneity

Figure 4.8 shows three-dimensional (3-D) views of the temperature distribution in M2. The four view angles are centered on the Atlantic, the Indian Ocean, and the western and eastern Pacific, respectively. The earth-like convective vigor produces a narrow, upper thermal boundary layer with a thickness of about 100 km, and correspondingly thin and elongated downwellings in regions of present day plate convergence (e.g., under the Marianna and Izu-Bonin subduction systems, the Sumatra and Tonga-Kermadec trench). Remnants of the Tethyan subduction are visible in a broad upper and mid-mantle region under Eurasia. Subduction of the old Farallon plate is evident in the deeper mantle under eastern North America and under South America. In the lowermost mantle, prominent hot upwellings are located in the southeast Pacific and under southern Africa up to Europe and Iceland (see top panels in Fig. 4.8). While the upwellings are consistent with the dynamics of flow with strong core heat flux, their morphology and location are entirely due to the model initialization, since the available plate motion history is too short to affect the pattern of deep mantle heterogeneity (see *Bunge et al.* (2002) for a discussion, and *Torsvik et al.* (2008) for efforts to extend plate motion histories to longer time periods in the past).

A remarkable feature is the spontaneous emergence of the asthenosphere as a region of relatively uniform temperature with much less thermal heterogeneity (the thin, almost white band in the upper mantle in Fig. 4.8, bottom panels). Due to the lower viscosity in this layer, material flows laterally over considerable distance (see thermal upwelling under the East Pacific Rise which feeds a broad region of hot asthenosphere in the equatorial Pacific), and as a result thermal variations are effectively equilibrated. This agrees well with petrological studies, which infer only minor melting temperature variations beneath the global mid-ocean ridge system (*McKenzie and Bickle*, 1988; *Presnall and Gudfinnsson*, 2008).

Horizontal sections through M1 and M2 are shown in Figure 4.9. Columns one and two (from left to right) illustrate how thermal structure varies between models with high and low core heat flux. Starting from the top, at 100 km depth, cold downwellings dominate the thermal heterogeneity pattern, as noted before. Continental regions and the oldest parts of the oceans are also colder than average, while hot material beneath oceanic regions follows the global distribution of spreading centers. Slabs control the thermal structure also at 340 km depth. Deeper down at 800 km depth, prominent cold downwellings are located around the Pacific, but their position differs from shallower depth levels because they reflect earlier stages

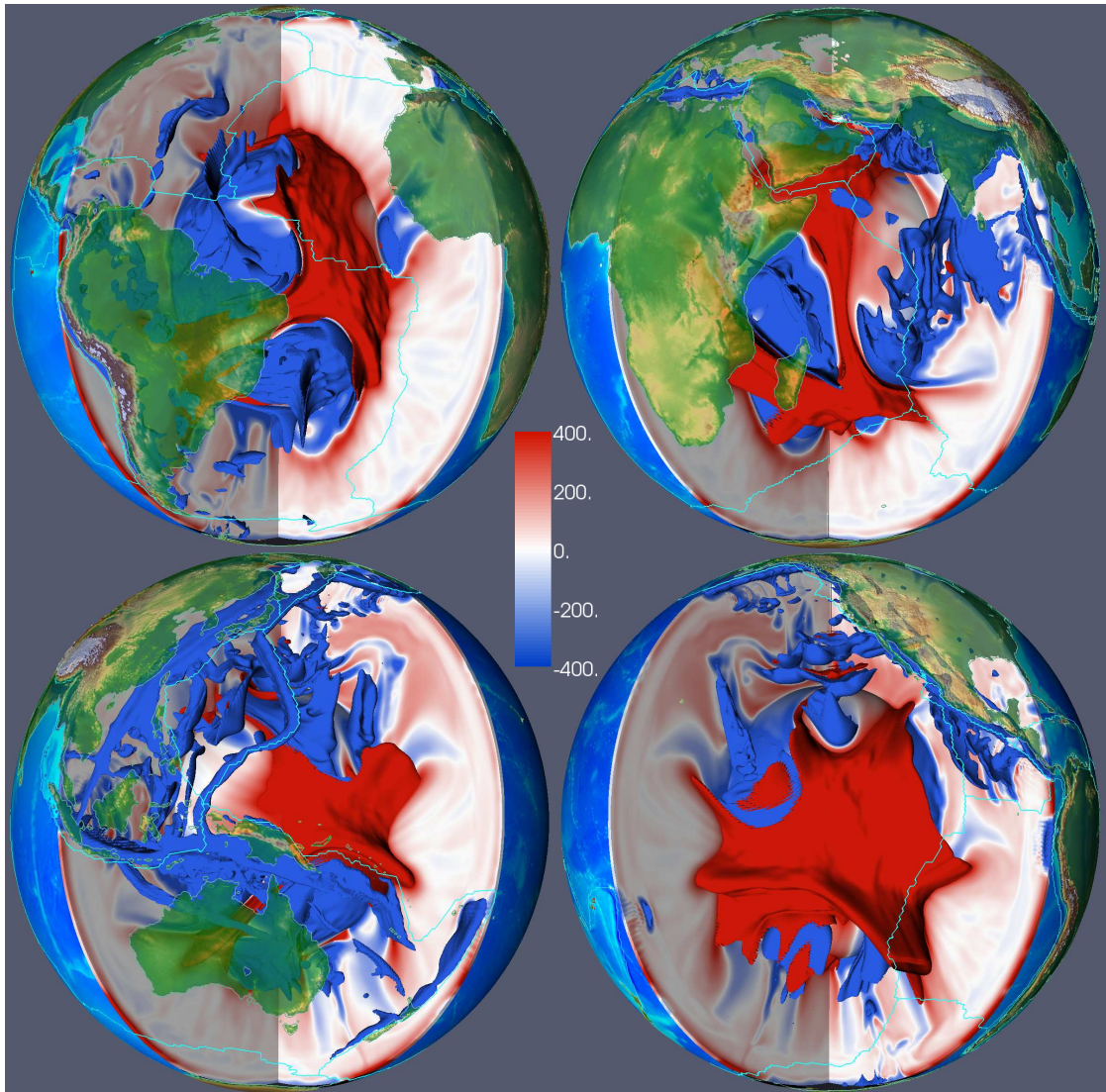


Figure 4.8: Three-dimensional representation of temperature variations in model M2 with strong core heat flux (see text). The four adjacent cross sections are centered on 35 (upper left), 125 (lower right), 215 (lower left) and 305 (upper right) degrees longitude. The color scale is saturated at -400 K and $+400$ K, and continents with color-coded topography and plate boundaries (cyan lines) are overlain for geographic reference. Isosurfaces of temperature are displayed for -600 K and $+400$ K. The $+400$ K isosurface is clipped in the uppermost 500 km to allow views into the mantle underneath the mid-ocean ridge system, which spans large parts of the oceanic upper mantle. The reduced thermal heterogeneity in the upper mantle (thin, almost white band best visible in the views centered on 125 and 215 degrees longitude) is a consequence of the lower viscosity, there. Note also the prominent thermal upwelling in the Eastern and Central Pacific not far from the SOPITA anomaly identified on thermal and geochemical grounds by *Staudigel et al.* (1991).

of plate subduction (e.g., cold material associated with subduction of the Farallon plate east of North America's West Coast, and remnants of the Tethys Ocean as a distinct cold feature beneath Africa, Arabia and India). A hot thermal anomaly in M2 is located in the southeast Pacific.

There is little overall change in the mid mantle, at 1450 km depth, except for the location of downwellings. Here, the Farallon slab lies east of North America, and remnants of subduction exist under central America. The feature with the largest thermal amplitude is a group of downwelling slabs corresponding to the broad collision of India and Eurasia. Cold material exists also under the north Pacific, which can be traced back to the convergence of the North American and Kula plate 50–70 Ma ago according to the reconstructions. Significant differences between M1 and M2 appear between 2000 km and the CMB. M2 is dominated by prominent hot upwellings under the South Pacific Ocean and (to a lesser extent) in the Indian Ocean, while cold material spreads laterally in both models as it approaches the lowermost mantle and the CMB. Near the CMB at 2800 km depth, hot upwellings in M2 give rise to large lateral temperature variations, reaching maximum positive values of up to +1500 K (see also Figure 4.11), while in model M1 there are much smaller variations on the order of +200–250 K.

Thermal vs. Elastic 3-D Heterogeneity

We return to Figure 4.9 where relative variations in S- and P-wave velocity derived from model M2 are shown in columns three and four. The elastic heterogeneity is inferred by converting absolute model temperatures to absolute values of S- and P-wave velocity using the mineralogical model SLB for a pyrolite composition. Relative variations are then computed with respect to the mean seismic velocity at each depth. The main effect of the conversion is to amplify heterogeneity in the uppermost mantle, while there is a trend toward less heterogeneity with depth. Note that shear velocity variations are much stronger throughout the mantle than variations in compressional velocity.

Spectral heterogeneity maps (SHM) (*Jordan et al.*, 1993), which are contour plots of spectral amplitude *vs.* depth, for all four MCMs are shown in Figure 4.10. In the following, we consider temperatures together with shear wave velocities based on the mineralogical model SLB. Radial profiles of the root-mean-square (RMS) power of the spherical harmonics expansion are also shown. Spectral power σ_l per degree l is computed at each depth level and for spherical harmonics degrees $l = 1, \dots, 20$ by (*Dahlen and Tromp*, 1998, B.8)

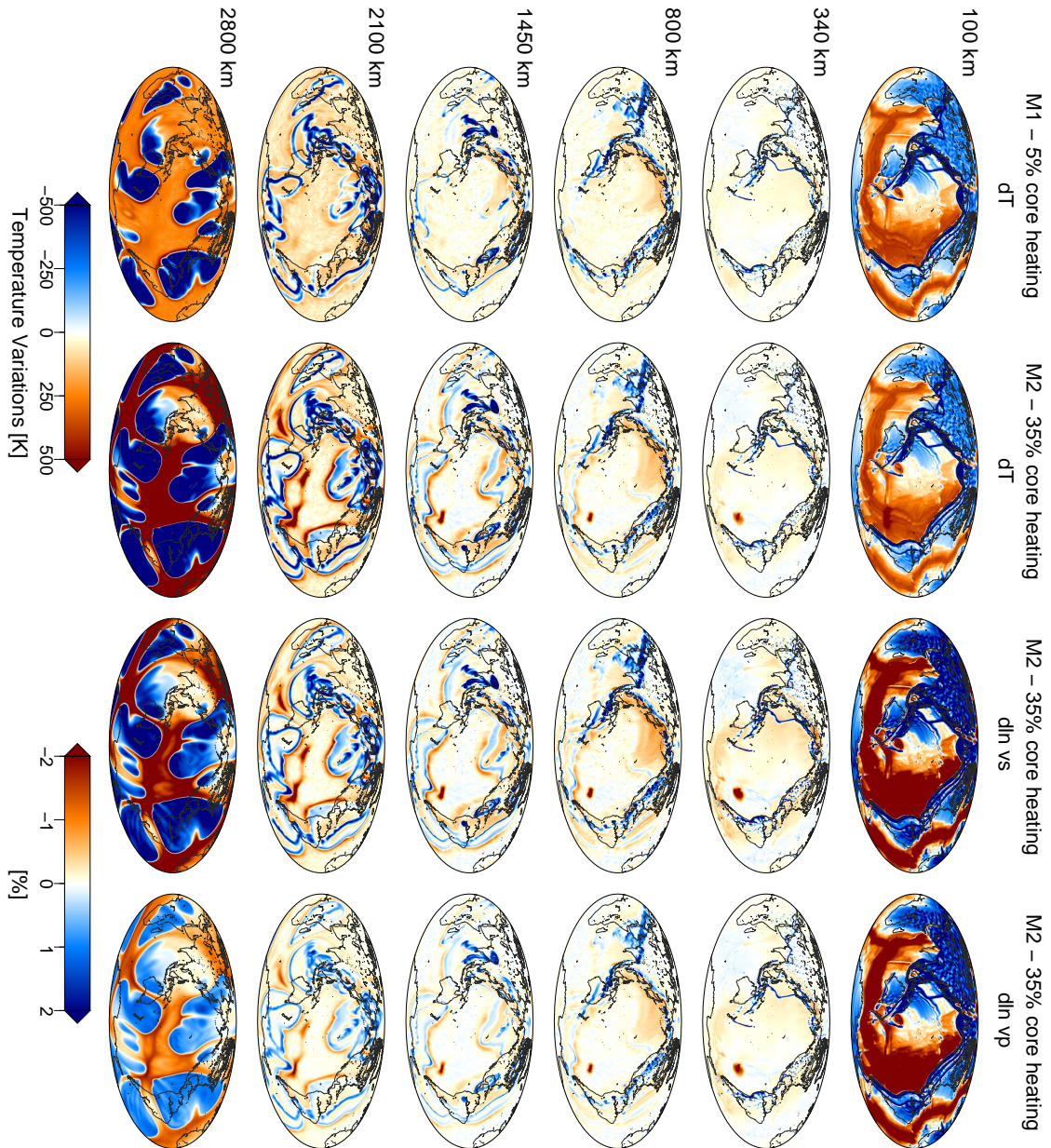


Figure 4.9: Depth slices through mantle circulation models M1 and M2 with weak and strong core heat flux, respectively. (left) Temperature variations in M1 and M2 and (right) elastic structure in M2 (strong core heating) for variations of shear, as well as compressional wave velocity relative to their radial average. Absolute values of seismic velocities are obtained from absolute values of temperature using the mineralogical model SLB (*Sticrrude and Lithgow-Bertelloni, 2005, 2007*).

$$\sigma_l = \sqrt{\frac{1}{2l+1} \left[a_{l0}^2 + \sum_{m=1}^l (a_{lm}^2 + b_{lm}^2) \right]}, \quad (4.1)$$

where a_{lm} and b_{lm} are the coefficients of the expansion and the RMS power is given by:

$$\delta\hat{v} = \sqrt{\frac{1}{\sqrt{4\pi}} \sum_{l=1}^{l_{\max}} (2l+1)\sigma_l^2}. \quad (4.2)$$

Spectral power of thermal heterogeneity (Fig. 4.10 a–d) is concentrated in the upper and lower thermal boundary layers of all MCMs, i.e., in the lithosphere and in the lowermost mantle. Thermal variations in the lithosphere exist on a broad range of spatial scales as indicated by strong spectral power in all spherical harmonic degrees. In the low-viscosity upper mantle, by comparison, there is much less thermal heterogeneity. The strength of heterogeneity increases again at the top of the lower mantle due to the higher viscosity there. Starting at around 750 km depth, pronounced heterogeneity at the largest length scale (spherical harmonic degree two) exists in all models, with a further increase in heterogeneity amplitude from the mid mantle (1500 km) downward. This low order pattern is due to the dominant long wavelength planform of the oldest stages of assimilated plate motion history from 80 to 120 Ma ago, and reflects the combined effects of plate motion and viscosity stratification (*Bunge and Richards, 1996*). In the deepest mantle, and approaching the lower thermal boundary layer, heterogeneity can also be found in higher degrees. Note that the weak mid mantle heterogeneity in M4 (Fig. 4.10 d) reflects the lower viscosities in this model. The overall distribution of heterogeneity, with maxima near the top and bottom thermal boundary layers, is also reflected in the radial profiles of RMS spectral power in all four MCMs.

The spectral heterogeneity maps for v_s , displayed in Figures 4.10 e–h, look rather different compared to those of temperature, which reveals the strong effects of mantle mineralogy. They only show similarities in the overall characteristics (strong heterogeneity in the lithosphere and the lowermost mantle, dominated by long wavelength structure). The biggest difference in spectral power between v_s and thermal variations exists in the upper mantle, where narrow bands of spectral power up to degree 20 are visible for v_s . These correspond to the major phase transformations in the transition zone at 410 km, 520 km and 660 km depth.

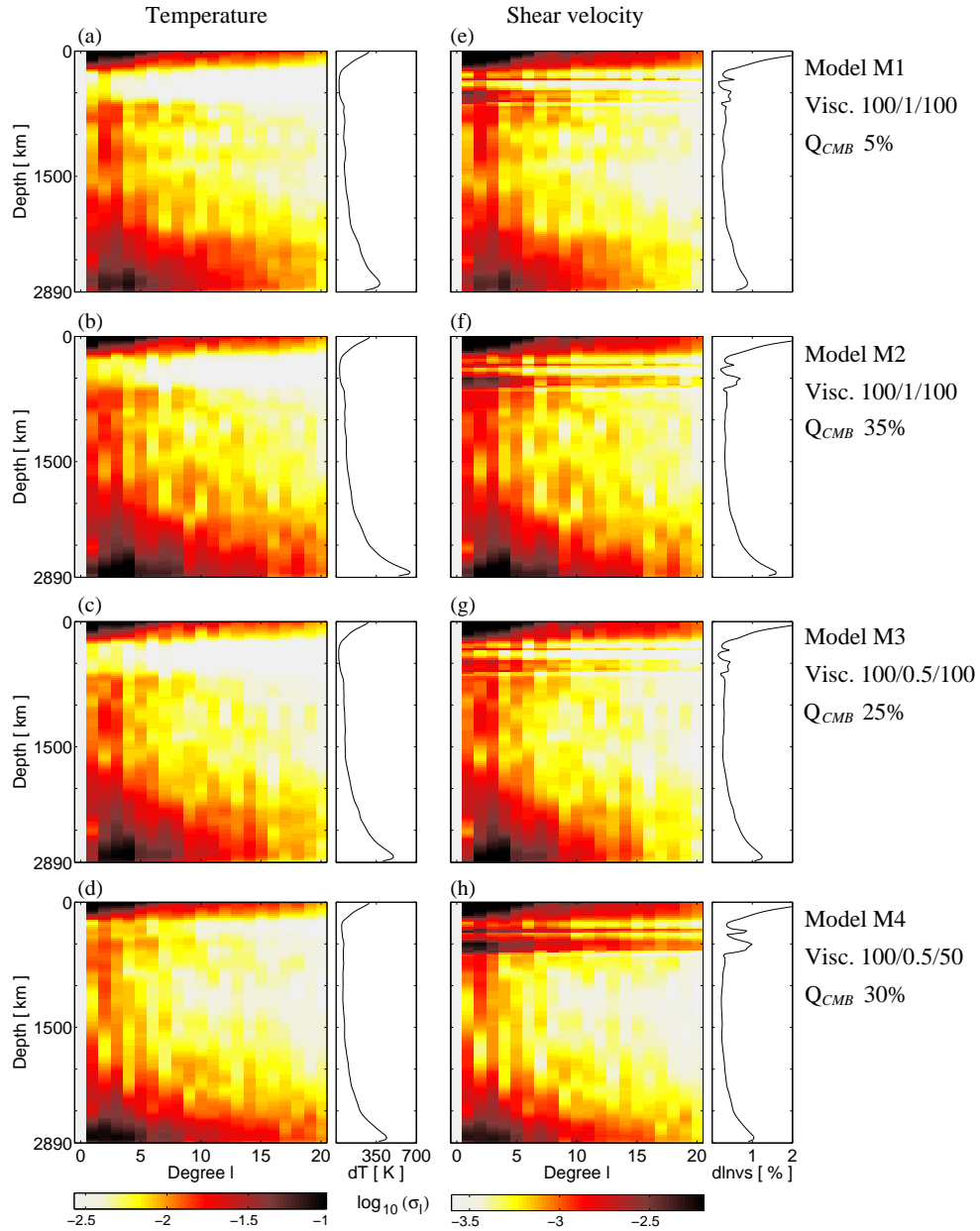


Figure 4.10: Spectral power of heterogeneity in (a–d) temperature and (e–h) shear wave velocity for mantle circulation models M1–M4 (see text). Spectral power is plotted on a logarithmic scale as a function of spherical harmonics degree and depth. Subplots on the right of each spectral heterogeneity map show the root-mean-square amplitudes of temperature and v_s perturbations as a function of depth, respectively. Relative variations of shear wave velocity are derived from the mantle circulation models using the mineralogical model SLB (*Stixrude and Lithgow-Bertelloni, 2005, 2007*). Note the differences between thermal and seismic heterogeneity. For example, the change in spectral power from the upper to the lower mantle is of opposite sense. The narrow bands of strong power in v_s in the upper mantle are a consequence of the mineralogy in the transition zone (see text), even though there is reduced thermal heterogeneity in these depth levels. Note the overall increase in spectral amplitude of temperature and v_s in the lowermost mantle.

Variations in the amount of CMB heat flow influence the power distribution less than the differences in radial viscosity profiles (compare e.g., Figs. 4.10 e, f and h), as the radial viscosity structure primarily controls the speed of flow and therefore the depth of subducted material. A higher CMB heat flux instead increases the amplitude of lower mantle heterogeneity, e.g., more heterogeneity is present in the lowermost mantle in model M2 compared to M1 and also in higher degrees.

The difference in spectral heterogeneity between temperature and shear wave velocity in the upper mantle can be explained by the increased sensitivity of shear wave velocity to temperature at the upper mantle discontinuities. This sensitivity is the result of two combined effects: On the one hand temperature directly influences the elastic properties of a fixed phase assemblage. On the other hand, temperature also affects the stable phase assemblage, which in turn strongly changes the elastic properties of the bulk rock (*Ricard et al.*, 2005; *Stixrude and Lithgow-Bertelloni*, 2007). The latter effect is most significant in the upper mantle, leading to the fine scale heterogeneity observed in v_s in the transition zone.

The change in pattern between thermal and elastic spectral heterogeneity suggests caution in the geodynamic interpretation of tomographic models (v_s or v_p). For example, from the spectral characteristics of v_s in Figures 4.10 e–h one may argue for a change in the convective style between the upper and lower mantle. The underlying thermal variations in the geodynamic models, however, show an increase in the power of heterogeneity from the upper to the lower mantle, opposite to what is seen in the elastic parameters. As noted before, this is the result of an increase in viscosity at the upper mantle/lower mantle boundary, which however, does not inhibit mass exchange.

4.2.4 Discussion

We have investigated the thermal and elastic structure of high-resolution mantle circulation models and find that whole mantle flow with strong core heating is compatible with a variety of quantitative measures inferred from tomography: histograms, RMS amplitudes, and spectral power of variations in shear wave velocity. In particular, the hot lower mantle thermal anomalies on the order of 1000 K and the corresponding reduction in shear wave velocity of up to -4% , which we infer using published models of mantle mineralogy (*Piazzoni et al.*, 2007; *Stixrude and Lithgow-Bertelloni*, 2005, 2007), agrees remarkably well with shear wave anomalies mapped in low seismic velocity regions of the deeper mantle (see histograms in Figures 4.11 e–h and 4.12). Apart from the isochemical, pyrolitic nature of our models, we have made three basic assumptions in the construction of global geodynamic mantle heterogeneity: 1) a large-scale flow structure related to

past plate motion, 2) a radial viscosity profile that agrees with post-glacial rebound and geoid observations, and 3) a significant vertical temperature change across the CMB of ~ 1000 K corresponding to a large core heat flow of 9–12 TW.

An important argument in support of chemical heterogeneity is the morphology, or shape, of deep mantle upwellings, taken either from direct observations of seismic data (*Ni et al.*, 2002), or from laboratory (*Jellinek and Manga*, 2004) and numerical studies (*McNamara and Zhong*, 2004). Unfortunately, the shape of lower mantle structure is poorly constrained by mantle circulation models relying on the sequential assimilation of past plate motions (*Bunge et al.*, 2002; *McNamara and Zhong*, 2005). The difficulty arises from lack of information on the initial condition (*Bunge et al.*, 2003) and uncertainties in models of plate motion history, which grow larger as one goes back in time. As an example of the latter, we compare Figures 4.9 and 4.7. The hot upwelling structure under southern Africa is predicted too far south by our MCM approach (see also the cold downwelling structure under Northeast Africa in Figs. 4.8 and 4.9), probably as a result of uncertainties in the convergence history of the African and Eurasian plates. This interpretation is supported by the recent reconstructions of *Müller et al.* (2008), which place the convergent margin farther north than the plate motion history used in our study (*Lithgow-Bertelloni and Richards*, 1998). Efforts are currently underway to extend models of past plate motions further back in time (*Torsvik et al.*, 2008), and to explore adjoint techniques in geodynamic simulations to better constrain the temporal evolution of the mantle (*Bunge et al.*, 2003; *Ismail-Zadeh et al.*, 2004, 2007; *Liu and Gurnis*, 2008).

4.2.5 Conclusions

We have presented global models of thermal and elastic mantle heterogeneity derived from high-resolution mantle circulation modeling involving 80 million finite elements. Variations in seismic velocities are obtained by converting absolute temperatures into elastic heterogeneity using recently published thermodynamically self-consistent models of mantle petrology and elasticity. We find significant differences in the characteristics of thermal and seismic heterogeneity, which warrant a careful geodynamic interpretation of tomographic models. Most importantly, our models make a number of quantitative predictions for statistical properties such as spectral power, histograms and RMS amplitudes, all of which are found in good agreement with tomography. A key observation is the magnitude of lower mantle thermal anomalies (on the order of 1000 K). The corresponding strong reduction in shear wave velocity, which we infer for hot upwelling regions in our models, agrees

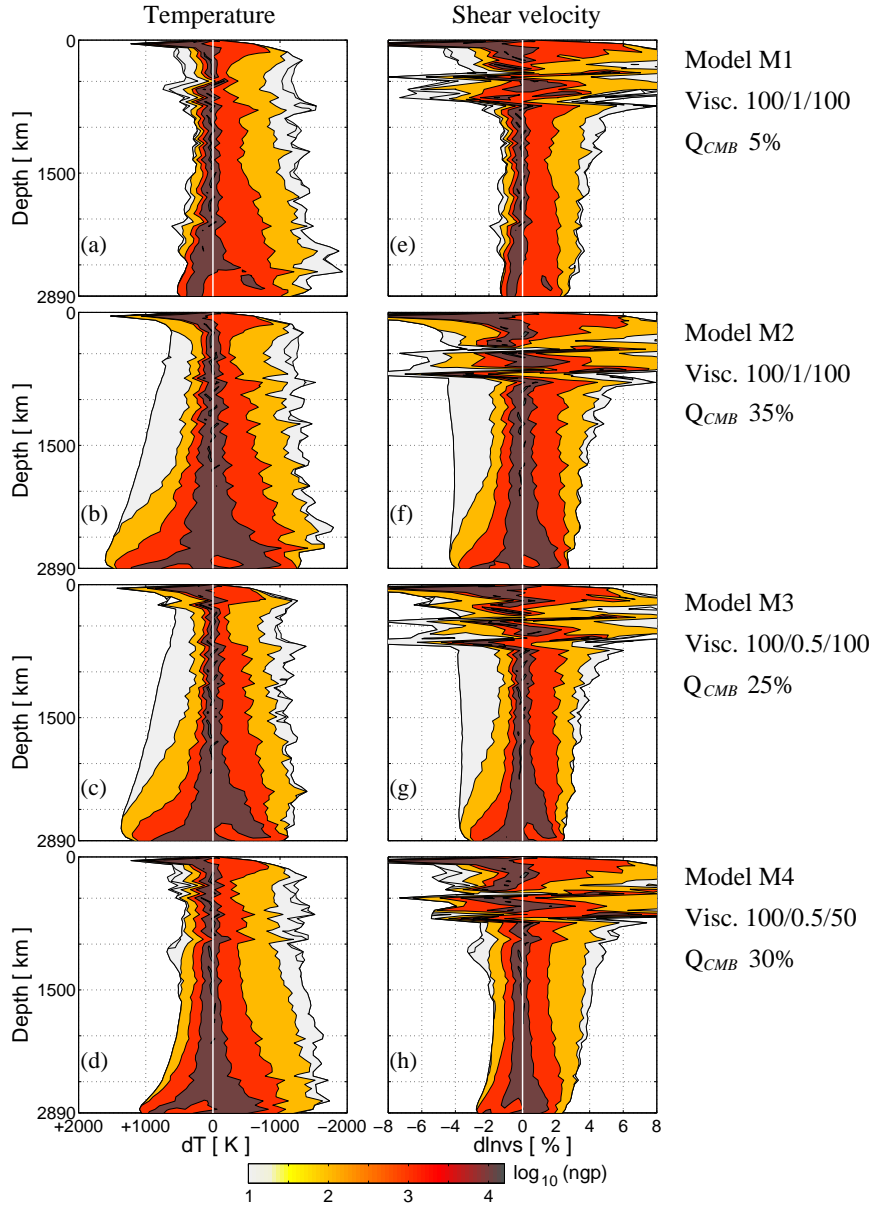


Figure 4.11: (a–d) Histograms of temperature variations in mantle circulation models M1–M4. Color scale and contours represent number of grid points (ngp) on a logarithmic scale as a function of temperature perturbation and depth. Contour lines are plotted for $\log_{10}(ngp) = 1, 2, 3$ and 4 . Note: The x axis (dT) of the temperature histograms has been flipped in consequence of the negative sensitivity of v_s to temperature to ease the comparison with the histograms for v_s . (e–h) Same as (a–d) for variations of shear wave velocity obtained from mantle circulation models M1–M4 using the mineralogical model SLB (*Stixrude and Lithgow-Bertelloni, 2005, 2007*). Comparison of thermal and elastic structures reveals the general decrease in sensitivity of v_s to temperature with depth. Maximum thermal variations on the order of -1000 K from cold slabs and more than $+1000$ K from hot upwellings in the lowermost mantle (M2–M4) result in maximum v_s anomalies of $+2\%$ and -4% . In contrast to these models with strong core heating, model M1 has much lower negative v_s amplitudes of around -1% resulting from positive thermal anomalies of only up to $+500$ K.

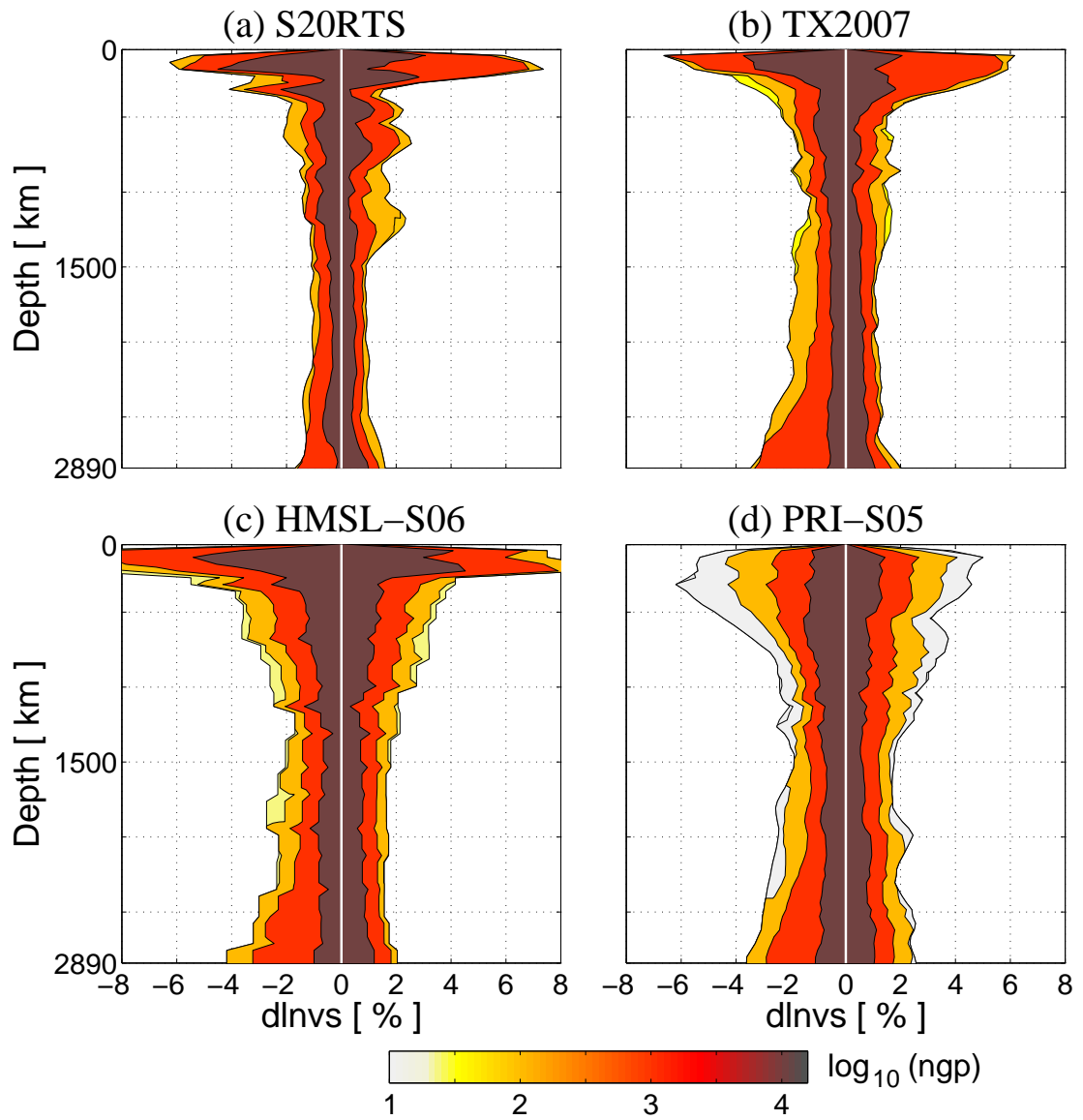


Figure 4.12: Histograms of relative variations of shear wave velocity in tomographic models S20RTS (*Ritsema et al.*, 2004), TX2007 (*Simmons et al.*, 2007), HMSL-S06 (*Houser et al.*, 2008) and PRI-S05 (*Montelli et al.*, 2006). Color scale and contour lines are the same as in Figure 4.11. The tomographic histograms are normalized to the number of grid points in our MCMs to allow for a direct comparison with Figure 4.11.

well with the magnitude of shear wave anomalies mapped by tomography in low velocity regions of the deeper mantle.

Our results suggest that simple isochemical mantle circulation models are capable of explaining some first-order observations from tomography when combined with strong heat flux from the core on the order of 9–12 TW. This number is supported by many recent studies on core and mantle dynamics, related material properties, as well as by seismological observations. Uncertainties in plate tectonic reconstructions and the unknown initial condition of mantle general circulation, however, limit our capabilities of constraining the geographic pattern of heterogeneity in the lowermost mantle.

The models presented here may be improved in various ways. For example, updated models of plate motion history will help to better constrain the location and morphology of deeper mantle structure. Also, we have not included the effects of horizontal viscosity variations, which are particularly important in the lithosphere in generating shear localisation and plate like behavior through temperature dependent viscosities and plastic yielding (*Trompert and Hansen, 1998; Richards et al., 2001*), although a combination of neotectonic and mantle convection modeling appears effective in modeling the complexities of plate motion (*Iaffaldano et al., 2006; Iaffaldano and Bunge, 2008*).

Furthermore, the mineralogical models currently do not account for the potential presence of post-perovskite, thus limiting conclusions on structure in D". Moreover, we have also excluded any additional complexity arising from chemical variations, choosing to study simple isochemical models first and to isolate thermal effects. Work by *Hutko et al. (2008)* and *Hernlund and Houser (2008)* suggests that at least part of the observed anti-correlation of v_s and v_ϕ , which is difficult to explain from a uniform composition, could be related to the occurrence of post-perovskite. With respect to sharp gradients in seismic structures observed in the lower mantle, and the possibility to explain these by a purely thermal origin, our high-resolution MCMs with their strong lateral variations will have to be filtered to the resolution of tomography for further comparisons.

Finally, tomographic models as well have to be refined, especially in terms of resolving the amplitudes and gradients of heterogeneity. In this respect, various improvements in tomographic imaging techniques are currently investigated, such as finite frequency tomography including waveform amplitude information (*Sigloch et al., 2008*) or full waveform inversion using adjoint techniques (*Tromp et al., 2005; Fichtner et al., 2006a,b*).

4.3 Differences between Plate Reconstructions and their Effects on Mantle Circulation Simulations

The study described in section 4.2 has used the widely adopted plate reconstruction model of *Lithgow-Bertelloni and Richards* (1998). Some shortcomings of this plate reconstruction are directly visible in the results. For example, the coarse time stepping of this reconstruction causes subduction zones to jump over time, instead of a smooth transition; this creates fragmented slabs. An example of such an artifact is clearly visible in fig. 4.8 (lower right globe): The Farallon slab is torn into three parallel stripes, which is incompatible with high-resolution tomographic observations such as *Sigloch et al.* (2008).

A further assessment of this plate reconstruction has been done by *Schaber et al.* (2009). They use the same mantle circulation model for computing the resulting geoid. In their analysis, the Western Pacific geoid low has been strongly overestimated; they explain this by comparing the plate reconstruction of *Lithgow-Bertelloni and Richards* (1998) qualitatively with the competing and more advanced reconstruction of *Müller et al.* (2008) (fig. 4.13): The reconstruction of *Müller et al.* (2008) suggest the presence of a mid-ocean ridge, and thus the subduction of very young ocean floor under Eastern Asia as recent as 70 Ma, whereas there is much older and thus less buoyant ocean floor offshore this region in the plate model of *Lithgow-Bertelloni and Richards* (1998). Furthermore, *Schaber et al.* (2009) observe a model misfit for the African geoid high, and explain this with the very different position and polarity of the Tethys subduction between Africa and Eurasia.

These results indicate that with the more sophisticated plate reconstructions described in section 4.1.1 that are now available or being produced, substantially better mantle circulation models will be possible.

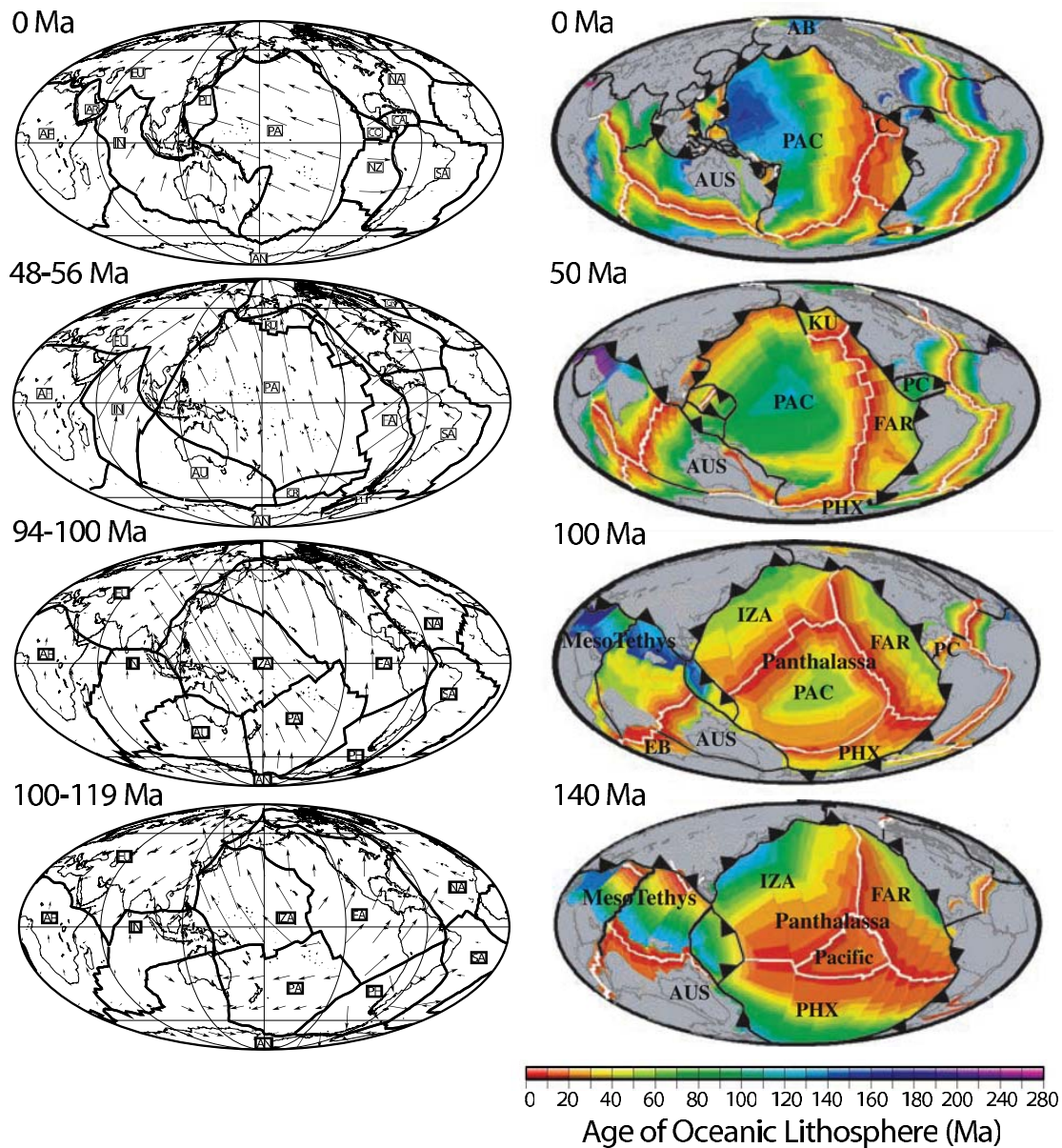


Figure 4.13: Comparison of the plate reconstructions of *Lithgow-Bertelloni and Richards* (1998) (left) and *Müller et al.* (2008) (right). Note the remarkable differences in the plate boundaries (left: thick lines; right: black and white lines) in the reconstructions earlier than 70 Ma: The reconstruction of *Müller et al.* (2008) puts the ridge between the Pacific plate (PA/PAC) and the Izanagi plate (IZA) far further to the North, which leads to a subduction of much younger material under Eurasia (EU). Furthermore, the Tethys subduction between Africa (AF) and Eurasia is in this model lies ca. 20° north compared to the model of *Lithgow-Bertelloni and Richards* (1998). (Map center: 0°N 180°E)

A Bibliography

- Amante, C., and B. W. Eakins (2009), ETOPO1 1 arc-minute global relief model: Procedures, data sources and analysis, *NOAA technical memorandum NESDIS NGDC-24*, NOAA.
- Anderson, E. (1942), *The dynamics of faulting and dyke formation with application to Britain*, 191 pp., Oliver and Boyd, Edinburgh.
- Angelier, J., et al. (2001), Le séisme de Chichi (1999) et sa place dans l'orogène de Taiwan, *Comptes Rendus de l'Académie des Sciences — Series IIA — Earth and Planetary Science*, *333*(1), 5–21, doi:10.1016/S1251-8050(01)01563-4.
- Axen, G. J. (2007), Research focus: Significance of large-displacement, low-angle normal faults, *Geology*, *35*(3), 287–288, doi:10.1130/0091-7613(2007)35[287:RFSOLL]2.0.CO;2.
- Baumgardner, J. R. (1988), *Application of supercomputers to 3-D mantle convection.*, pp. 199–231, John Wiley and Sons.
- Becker, T. W., and R. J. O'Connell (2001), Predicting plate velocities with mantle circulation models, *Geochem. Geophys. Geosyst.*, *2*(12), doi:10.1029/2001GC000171,2001.
- Bennett, R. A., B. P. Wernicke, N. A. Niemi, A. M. Friedrich, and J. L. Davis (2003), Contemporary strain rates in the northern basin and range province from GPS data, *Tectonics*, *22*(2), 1008, doi:10.1029/2001TC001355.
- Bilotti, F., and J. H. Shaw (2005), Deep-water Niger delta fold and thrust belt modeled as a critical-taper wedge: The influence of elevated basal fluid pressure on structural styles, *AAPG Bulletin*, *89*(11), 1475–1491, doi:10.1306/06130505002.
- Bird, P. (1989), New finite element techniques for modeling deformation histories of continents with stratified temperature-dependent rheology, *J. Geophys. Res.*, *94*(B4), 3967–3990, doi:10.1029/JB094iB04p03967.
- Bird, P. (1998), Testing hypotheses on plate-driving mechanisms with global lithosphere models including topography, thermal structure, and faults, *J. Geophys. Res.*, *103*(B5), 10,115–10,129, doi:10.1029/98JB00198.

- Bird, P. (1999), Thin-plate and thin-shell finite-element programs for forward dynamic modeling of plate deformation and faulting, *Computers & Geosciences*, 25(4), 383–394, doi:10.1016/S0098-3004(98)00142-3.
- Bird, P. (2003), An updated digital model of plate boundaries, *Geochem. Geophys. Geosyst.*, 4(3), 1027, doi:10.1029/2001GC000252.
- Bird, P., and X. Kong (1994), Computer simulations of California tectonics confirm very low strength of major faults, *Geological Society of America Bulletin*, 106(2), 159–174, doi:10.1130/0016-7606(1994)106<0159:CSOCTC>2.3.CO;2.
- Bird, P., and Z. Liu (1999), Global finite-element model makes a small contribution to intraplate seismic hazard estimation, *Bulletin of the Seismological Society of America*, 89(6), 1642–1647.
- Bird, P., Y. Y. Kagan, and D. D. Jackson (2002), Plate tectonics and earthquake potential of spreading ridges and oceanic transform faults, in *Plate Boundary Zones*, vol. 30, edited by S. Stein and J. T. Freymueller, geodynamics series ed., pp. 203–218, AGU, Washington, DC.
- Bird, P., Z. Liu, and W. K. Rucker (2008), Stresses that drive the plates from below: Definitions, computational path, model optimization, and error analysis, *J. Geophys. Res.*, 113(B11), B11,406, doi:10.1029/2007JB005460.
- Brace, W. F., and D. L. Kohlstedt (1980), Limits on lithospheric stress imposed by laboratory experiments, *J. Geophys. Res.*, 85(B11), 6248–6252, doi:10.1029/JB085iB11p06248.
- Bulatov, V. V. (2008), Crystal plasticity from dislocation dynamics, in *Materials Issues for Generation IV Systems*, edited by V. Ghetta, D. Gorse, D. Mazière, and V. Pontikis, NATO Science for Peace and Security Series B: Physics and Biophysics, pp. 275–284, Springer Netherlands, doi: 10.1007/978-1-4020-8422-5_14.
- Bunge, H., and J. Baumgardner (1995), Mantle convection modeling on parallel virtual machines, *Computers in Physics*, 9, 207–215.
- Bunge, H. P. (1996), Global mantle convection models, Ph.D. thesis, University of California, Berkeley.
- Bunge, H.-P. (2005), Low plume excess temperature and high core heat flux inferred from non-adiabatic geotherms in internally heated mantle circulation models, *Physics of The Earth and Planetary Interiors*, 153(1–3), 3–10, doi: 10.1016/j.pepi.2005.03.017.
- Bunge, H.-P., and M. Richards (1996), The origin of large-scale structure in mantle convection: effects of plate motions and viscosity stratification, *Geophys. Res. Lett.*, 23, 2987–2990.

- Bunge, H.-P., M. Richards, and J. Baumgardner (1996), The effect of depth-dependent viscosity on the planform of mantle convection, *Nature*, *379*, 436–438, doi:10.1038/379436a0.
- Bunge, H.-P., M. A. Richards, and J. R. Baumgardner (1997), A sensitivity study of three-dimensional spherical mantle convection at 10^8 rayleigh number: Effects of depth-dependent viscosity, heating mode, and an endothermic phase change, *J. Geophys. Res.*, *102*(B6), 11,991–12,007, doi:10.1029/96JB03806.
- Bunge, H.-P., M. A. Richards, C. Lithgow-Bertelloni, J. R. Baumgardner, S. P. Grand, and B. A. Romanowicz (1998), Time scales and heterogeneous structure in geodynamic Earth models, *Science*, *280*(5360), 91–95, doi:10.1126/science.280.5360.91.
- Bunge, H. P., Y. Ricard, and J. Matas (2001), Non-adiabaticity in mantle convection, *Geophys. Res. Lett.*, *28*(5), 879–882.
- Bunge, H.-P., M. Richards, and J. Baumgardner (2002), Mantle circulation models with sequential data-assimilation: Inferring present-day mantle structure from plate motion histories, *Royal Society of London Philosophical Transactions Series A*, *360*(1800), 2545–2567, doi:10.1098/rsta.2002.1080.
- Bunge, H.-P., C. R. Hagelberg, and B. J. Travis (2003), Mantle circulation models with variational data-assimilation: Inferring past mantle flow and structure from plate motion histories and seismic tomography, *Geophys. J. Int.*, *2*(152), 280–301, doi:10.1046/j.1365-246X.2003.01823.x.
- Byerlee, J. (1978), Friction of rocks, *Pure and Applied Geophysics*, *116*, 615–626, doi:10.1007/BF00876528.
- Bürgmann, R., and G. Dresen (2008), Rheology of the lower crust and upper mantle: Evidence from rock mechanics, geodesy, and field observations, *Annual Review of Earth and Planetary Sciences*, *36*(1), 531–567, doi:10.1146/annurev.earth.36.031207.124326.
- Cammarano, F., S. Goes, P. Vacher, and D. Giardini (2003), Inferring upper-mantle temperatures from seismic velocities, *Phys. Earth Planet. Inter.*, *138*(3–4), 197–222, doi:10.1016/S0031-9201(03)00156-0.
- Carena, S., and C. Moder (2009), The strength of faults in the crust in the western United States, *Earth and Planetary Science Letters*, *287*(3–4), 373–384, doi:10.1016/j.epsl.2009.08.021.
- Carena, S., J. Suppe, and H. Kao (2002), Active detachment of Taiwan illuminated by small earthquakes and its control of first-order topography, *Geology*, *30*(10), 935–938, doi:10.1130/0091-7613(2002)030<0935:ADOTIB>2.0.CO;2.

- Carena, S., J. Suppe, and Y.-M. Wu (2010), Lithospheric structure of Taiwan from seismicity and crustal tomography, in *Program with abstracts, GSA Denver Annual Meeting*, vol. Paper #24-5.
- Central Geological Survey, MOEA (2004), Geologic provinces of Taiwan, http://www.moeacgs.gov.tw/english2/twgeol/twgeol_generalgeol.jsp.
- Chang, C. (2000), Origin and evolution of a mélangé: the active plate boundary and suture zone of the Longitudinal Valley, Taiwan, *Tectonophysics*, *325*, 43–62, doi:10.1016/S0040-1951(00)00130-X.
- Christensen, U. R., and A. W. Hofmann (1994), Segregation of subducted oceanic-crust in the convecting mantle, *J. Geophys. Res.*, *99*(B10), 19,867–19,884.
- Cogné, J.-P., and E. Humler (2004), Temporal variation of oceanic spreading and crustal production rates during the last 180 My, *Earth and Planetary Science Letters*, *227*(3–4), 427–439, doi:10.1016/j.epsl.2004.09.002.
- Conrad, C. P., and C. Lithgow-Bertelloni (2002), How mantle slabs drive plate tectonics, *Science*, *298*(5591), 207–209, doi:10.1126/science.1074161.
- Cuthill, E., and J. McKee (1969), Reducing the bandwidth of sparse symmetric matrices, in *ACM '69: Proceedings of the 1969 24th national conference*, pp. 157–172, ACM, New York, NY, USA, doi:10.1145/800195.805928.
- Dahlen, F. A., and J. Tromp (1998), *Theoretical Global Seismology*, Princeton University Press, Princeton, New Jersey.
- d'Alessio, M. A., I. A. Johanson, R. Bürgmann, D. A. Schmidt, and M. H. Murray (2005), Slicing up the San Francisco Bay Area: Block kinematics and fault slip rates from GPS-derived surface velocities, *J. Geophys. Res.*, *110*(B6), B06,403.1–B06,403.19.
- Davaille, A. (1999), Simultaneous generation of hotspots and superswells by convection in a heterogenous planetary mantle, *Nature*, *402*(6763), 756–760, doi:10.1038/45461.
- Davaille, A., F. Girard, and M. L. Bars (2002), How to anchor hotspots in a convecting mantle?, *Earth Planet. Sci. Lett.*, *203*(2), 621–634, doi:10.1016/S0012-821X(02)00897-X.
- Davies, G. F. (1988), Ocean bathymetry and mantle convection 1. Large-scale flow and hotspots, *J. Geophys. Res.*, *93*(B9), 10,467–10,480.
- Deschamps, F., and J. Trampert (2003), Mantle tomography and its relation to temperature and composition, *Phys. Earth Planet. Inter.*, *140*(4), 277–291, doi:10.1016/j.pepi.2003.09.004.

- Deschamps, F., and J. Trampert (2004), Towards a lower mantle reference temperature and composition, *Earth Planet. Sci. Lett.*, *222*(1), 161–175, doi:10.1016/j.epsl.2004.02.024.
- Di Toro, G., D. L. Goldsby, and T. E. Tullis (2004), Friction falls towards zero in quartz rock as slip velocity approaches seismic rates, *Nature*, *427*(6973), 436–439, doi:10.1038/nature02249.
- Dixon, T. H., S. Robaudo, J. Lee, and M. C. Reheis (1995), Constraints on present-day basin and range deformation from space geodesy, *Tectonics*, *14*(4), 755–772, doi:10.1029/95TC00931.
- Engebretson, D. C., A. Cox, and R. G. Gordon (1984), Relative motions between oceanic plates of the Pacific basin, *J. Geophys. Res.*, *89*(B12), 10,291–10,310.
- England, P., and G. Houseman (1985), Role of lithospheric strength heterogeneities in the tectonics of Tibet and neighbouring regions, *Nature*, *315*(6017), 297–301, doi:10.1038/315297a0.
- Farnetani, C. G., and H. Samuel (2005), Beyond the thermal plume paradigm, *Geophys. Res. Lett.*, *32*(7), L07,311, doi:10.1029/2005GL022360.
- Fialko, Y. (2006), Interseismic strain accumulation and the earthquake potential on the southern San Andreas fault system, *Nature*, *441*(7096), 968–971, doi:10.1038/nature04797.
- Fichtner, A., H.-P. Bunge, and H. Igel (2006a), The adjoint method in seismology: I — Theory, *Phys. Earth Planet. Inter.*, *157*(1–2), 86–104, doi:10.1016/j.pepi.2006.03.016.
- Fichtner, A., P. Bunge, and H. Igel (2006b), The adjoint method in seismology: II — Applications: traveltimes and sensitivity functionals, *Phys. Earth Planet. Inter.*, *157*(1–2), 105–123, doi:10.1016/j.pepi.2006.03.018.
- Fuis, G. S., and W. D. Mooney (1990), Lithospheric structure and tectonics from seismic-refraction and other data, *United States Geological Survey, Professional Paper*, *1515*, 207–236.
- Genrich, J. F., Y. Bock, and R. G. Mason (1997), Crustal deformation across the imperial fault: Results from kinematic GPS surveys and trilateration of a densely spaced, small-aperture network, *J. Geophys. Res.*, *102*(B3), 4985–5004, doi:10.1029/96JB02854.
- Glatzmaier, G. A. (1988), Numerical simulations of mantle convection — time-dependent, 3-dimensional, compressible, spherical-shell, *Geophysical And Astrophysical Fluid Dynamics*, *43*(2), 223–264, doi:10.1080/03091928808213626.
- GPlates development team (2010), GPlates interactive plate-tectonic reconstructions and visualisations, <http://gplates.org/>.

- Grand, S., R. van der Hilst, and S. Widiyantoro (1997), Global seismic tomography: A snapshot of mantle convection in the earth, *GSA Today*, 7, 1–7.
- Graymer, R., D. Ponce, R. Jachens, R. Simpson, G. Phelps, and C. Wentworth (2005), Three-dimensional geologic map of the Hayward fault, northern California: Correlation of rock units with variations in seismicity, creep rate, and fault dip, *Geology*, 33(6), 521–524, doi:10.1130/G21435.1.
- Hackl, M., and R. Malservisi (2008), Strain pattern from geodetic measurements, in *Geophys. Res. Abstracts 10*, no. EGU2008-A-07579 in EGU General Assembly.
- Hager, B. H., and R. J. O’Connell (1979), Kinematic models of large-scale flow in the Earth’s mantle, *J. Geophys. Res.*, 84(B3), 1031–1048, doi:10.1029/JB084iB03p01031.
- Hager, B. H., and M. A. Richards (1989), Long-wavelength variations in Earth’s geoid — physical models and dynamical implications, *Phil. Trans. Roy. Soc. A*, 328(1599), 309–327, doi:10.1098/rsta.1989.0038.
- Haines, E. (1994), Point in polygon strategies, in *Graphics Gems IV*, edited by P. Heckbert, pp. 24–46, Academic Press.
- Han, R., T. Shimamoto, T. Hirose, J.-H. Ree, and J.-i. Ando (2007), Ultralow friction of carbonate faults caused by thermal decomposition, *Science*, 316(5826), 878–881, doi:10.1126/science.1139763.
- Hansen, U., and D. A. Yuen (1989), Dynamical influences from thermal-chemical instabilities at the core-mantle boundary, *Geophys. Res. Lett.*, 16(7), 629–632.
- Hansen, U., and D. A. Yuen (1994), Effects of depth-dependent thermal expansivity on the interaction of thermal-chemical plumes with a compositional boundary, *Phys. Earth Planet. Inter.*, 86(1–3), 205–221, doi:10.1016/0031-9201(94)05069-4.
- Hansen, U., and D. A. Yuen (2000), Extended-Boussinesq thermal-chemical convection with moving heat sources and variable viscosity, *Earth Planet. Sci. Lett.*, 176(3–4), 401–411, doi:10.1016/S0012-821X(00)00009-1.
- Hardebeck, J. L., and E. Hauksson (2001), Crustal stress field in southern California and its implications for fault mechanics, *J. Geophys. Res.*, 106(B10), 21,859–21,882, doi:10.1029/2001JB000292.
- Hardebeck, J. L., and A. J. Michael (2004), Stress orientations at intermediate angles to the San Andreas fault, California, *J. Geophys. Res.*, 109(B11), B11,303, doi:10.1029/2004JB003239.

- Heard, H. C., A. E. Abey, B. P. Bonner, and R. N. Schock (1974), Mechanical behavior of dry Westerly granite at high pressure, *Tech. rep.*, California Univ., Livermore (USA). Lawrence Livermore Lab.
- Heidbach, O., M. Tingay, A. Barth, J. Reinecker, D. Kurfeß, and B. Müller (2008), The 2008 release of the World Stress Map, <http://www.world-stress-map.org>.
- Heney, T. (1968), Heat flow near major strike-slip faults in central and southern California, Ph.D. thesis, California Institute of Technology, Pasadena, CA.
- Hernlund, J. W., and C. Houser (2008), On the statistical distribution of seismic velocities in Earth's deep mantle, *Earth Planet. Sci. Lett.*, *265*(3–4), 423–437, doi:10.1016/j.epsl.2007.10.042.
- Hickman, S., and M. Zoback (2004), Stress orientations and magnitudes in the SAFOD pilot hole, *Geophys. Res. Lett.*, *31*(15), L15S12, doi:10.1029/2004GL020043.
- Horsman, E., R. W. Graymer, R. J. McLaughlin, R. C. Jachens, and D. S. Scheirer (2008), Examining the evolution of the peninsula segment of the San Andreas fault, northern California, using a 4-D geologic model, *AGU Fall Meeting Abstracts*, pp. A1933+.
- Houseman, G., and P. England (1986), Finite strain calculations of continental deformation I: Methods and general results for convergent zones, *J. Geophys. Res.*, *91*(B3), 3651–3663, doi:10.1029/JB091iB03p03651.
- Houseman, G., and P. England (1993), Crustal thickening versus lateral expulsion in the Indian–Asian continental collision, *J. Geophys. Res.*, *98*(B7), 12,233–12,249, doi:10.1029/93JB00443.
- Houser, C., G. Masters, P. Shearer, and G. Laske (2008), Shear and compressional velocity models of the mantle from cluster analysis of long-period waveforms, *Geophys. J. Int.*, *174*(1), 195–212, doi:10.1111/j.1365-246X.2008.03763.x.
- Hsu, Y.-J., J.-P. Avouac, S.-B. Yu, C.-H. Chang, Y.-M. Wu, and J. Woessner (2009), Spatio-temporal slip, and stress level on the faults within the western foothills of taiwan: Implications for fault frictional properties, *Pure and Applied Geophysics*, *166*, 1853–1884, doi:10.1007/s00024-009-0510-5.
- Hull, D., and D. Bacon (1984), *Introduction to Dislocations, Third Edition*, Pergamon Press Ltd., Oxford.
- Humphreys, E. D., and D. D. Coblenz (2007), North American dynamics and western U.S. tectonics, *Rev. Geophys.*, *45*(3), RG3001, doi:10.1029/2005RG000181.

- Hutko, A. R., T. Lay, J. Revenaugh, and E. J. Garnero (2008), Anticorrelated seismic velocity anomalies from post-perovskite in the lowermost mantle, *Science*, *320*(5879), 1070–1074, doi:10.1126/science.1155822.
- Iaffaldano, G., and H.-P. Bunge (2008), Strong plate coupling along the Nazca–South America convergent margin, *Geology*, *36*(6), 443–446, doi:10.1130/G24489A.1.
- Iaffaldano, G., and H.-P. Bunge (2009), Relating rapid plate-motion variations to plate-boundary forces in global coupled models of the mantle/lithosphere system: Effects of topography and friction, *Tectonophysics*, *474*(1–2), 393–404, doi:10.1016/j.tecto.2008.10.035, TOPO-EUROPE: The Geoscience of coupled Deep Earth–surface processes.
- Iaffaldano, G., H.-P. Bunge, and T. H. Dixon (2006), Feedback between mountain belt growth and plate convergence, *Geology*, *34*(10), 893–896, doi:10.1130/G22661.1.
- International Heat Flow Commission (2005), The global heat flow database, <http://www.heatflow.und.edu/index2.html>.
- Irifune, T. (1987), An experimental investigation of the pyroxene garnet transformation in a pyrolite composition and its bearing on the constitution of the mantle, *Phys. Earth Planet. Inter.*, *45*(4), 324–336, doi:10.1016/0031-9201(87)90040-9.
- Ishii, M., and J. Tromp (1999), Normal-mode and free-air gravity constraints on lateral variations in velocity and density of Earth’s mantle, *Science*, *285*(5431), 1231–1236, doi:10.1126/science.285.5431.1231.
- Ishii, M., and J. Tromp (2001), Even-degree lateral variations in the Earth’s mantle constrained by free oscillations and the free-air gravity anomaly, *Geophys. J. Int.*, *145*(1), 77–96, doi:10.1111/j.1365-246X.2001.00385.x.
- Ismail-Zadeh, A., G. Schubert, I. Tsepelev, and A. Korotkii (2004), Inverse problem of thermal convection: numerical approach and application to mantle plume restoration, *Phys. Earth Planet. Inter.*, *145*(1–4), 99–114, doi:10.1016/j.pepi.2004.03.006.
- Ismail-Zadeh, A., A. Korotkii, G. Schubert, and I. Tsepelev (2007), Quasi-reversibility method for data assimilation in models of mantle dynamics, *Geophys. J. Int.*, *170*(3), 1381–1398, doi:10.1111/j.1365-246X.2007.03496.x.
- Jachens, R., R. Simpson, R. Graymer, V. Langenheim, C. Wentworth, R. Stanley, and J. Colgan (2009), Construction of a three-dimensional geologic, tectonic, kinematic crustal model of coastal central California, *Seismol. Res. Lett.*, *80*(2), 323.

- Jackson, J. (2002), Strength of the continental lithosphere: time to abandon the jelly sandwich?, *GSA Today*, *12*, 4–10.
- Jarvis, G. T., and D. P. McKenzie (1980), Convection in a compressible fluid with infinite Prandtl number, *Journal Of Fluid Mechanics*, *96*, 515–583, doi:10.1017/S002211208000225X.
- Jeanloz, R., and S. Morris (1987), Is the mantle geotherm subadiabatic, *Geophys. Res. Lett.*, *14*(4), 335–338.
- Jellinek, A. M., and M. Manga (2004), Links between long-lived hot spots, mantle plumes, D", and plate tectonics, *Rev. Geophys.*, *42*, RG3002, doi:10.1029/2003RG000144.
- Jordan, T. H., P. Puster, G. A. Glatzmaier, and P. J. Tackley (1993), Comparisons between seismic earth structures and mantle flow models based on radial correlation-functions, *Science*, *261*(5127), 1427–1431, doi:10.1126/science.261.5127.1427.
- Karato, S.-I. (2010), Rheology of the deep upper mantle and its implications for the preservation of the continental roots: A review, *Tectonophysics*, *481*(1–4), 82–98, doi:10.1016/j.tecto.2009.04.011.
- Kellogg, L. H., B. H. Hager, and R. D. van der Hilst (1999), Compositional stratification in the deep mantle, *Science*, *283*(5409), 1881–1884, doi:10.1126/science.283.5409.1881.
- Kennett, B. L. N., S. Widiyantoro, and R. D. van der Hilst (1998), Joint seismic tomography for bulk sound and shear wave speed in the earth's mantle, *J. Geophys. Res.*, *103*(B6), 12,469–12,493.
- King, G. C. P. (1986), Speculations on the geometry of the initiation and termination processes of earthquake rupture and its relation to morphology and geological structure, *Pure and Applied Geophysics*, *124*, 567–585, doi:10.1007/BF00877216.
- Kirby, S. H. (1983), Rheology of the lithosphere, *Rev. Geophys.*, *21*(6), 1458–1487, doi:10.1029/RG021i006p01458.
- Kirby, S. H., and A. K. Kronenberg (1987), Rheology of the lithosphere: Selected topics, *Rev. Geophys.*, *25*(6), 1219–1244, doi:10.1029/RG025i006p01219.
- Kolossos (2005), <http://commons.wikimedia.org/wiki/File:Viskositaet1.svg>.
- Kong, X., and P. Bird (1995), SHELLS: A thin-shell program for modeling neotectonics of regional or global lithosphere with faults, *J. Geophys. Res.*, *100*(B11), 22,129–22,131, doi:10.1029/95JB02435.

- Lachenbruch, A., and J. Sass (1973), Thermomechanical aspects of the San Andreas fault system, in *Proceedings of the conference on tectonic problems of the San Andreas fault system*, vol. 13, edited by R. Kovach and A. Nur, pp. 192–205, Stanford University Publications in the Geological Sciences.
- Lachenbruch, A. H., and J. H. Sass (1992), Heat flow from Cajon Pass, fault strength, and tectonic implications, *J. Geophys. Res.*, *97*(B4), 4995–5015, doi:10.1029/91JB01506.
- Laidler, K. J. (1984), The development of the Arrhenius equation, *Journal of Chemical Education*, *61*(6), 494, doi:10.1021/ed061p494.
- Lay, T. (2008), Sharpness of the D” discontinuity beneath the Cocos Plate: Implications for the perovskite to post-perovskite phase transition, *Geophys. Res. Lett.*, *35*, L03,304, doi:10.1029/2007GL032465.
- Lee, C., and W. Cheng (1986), Preliminary heat flow measurements in Taiwan, presented at Circum-Pac. Energy and Miner. Resour. Conf.
- Li, X. D., and B. Romanowicz (1996), Global mantle shear velocity model developed using nonlinear asymptotic coupling theory, *J. Geophys. Res.*, *101*(B10), 22,245–22,272.
- Li, Y. (1976), Denudation of Taiwan island since the Pliocene epoch, *Geology*, *4*, 105–+, doi:10.1130/0091-7613(1976)4<105:DOTIST>2.0.CO;2.
- Lin, C.-H. (2000), Thermal modeling of continental subduction and exhumation constrained by heat flow and seismicity in Taiwan, *Tectonophysics*, *324*(3), 189–201, doi:10.1016/S0040-1951(00)00117-7.
- Lithgow-Bertelloni, C., and M. A. Richards (1998), The dynamics of Cenozoic and Mesozoic plate motions, *Rev. Geophys.*, *36*(1), 27–78.
- Liu, L. J., and M. Gurnis (2008), Simultaneous inversion of mantle properties and initial conditions using an adjoint of mantle convection, *J. Geophys. Res.*, *113*(B8), B08,405, doi:10.1029/2008JB005594.
- Liu, Z., and P. Bird (2002), Finite element modeling of neotectonics in New Zealand, *J. Geophys. Res.*, *107*(B12), 2328, doi:10.1029/2001JB001075.
- Lundgren, P., E. A. Hetland, Z. Liu, and E. J. Fielding (2009), Southern San Andreas–San Jacinto fault system slip rates estimated from earthquake cycle models constrained by GPS and interferometric synthetic aperture radar observations, *J. Geophys. Res.*, *114*(B2), B02,403, doi:10.1029/2008JB005996.
- Mallet, J. (2002), *Geomodeling*, 593 pp., Oxford University Press, New York.
- Mansinha, L., and D. E. Smylie (1967), Effect of earthquakes on the Chandler wobble and the secular polar shift, *JGR*, *72*, 4731–+, doi:10.1029/JZ072i018p04731.

- Masters, G., S. Johnson, G. Laske, H. Bolton, and J. H. Davies (1996), A shear-velocity model of the mantle, *Phil. Trans. Roy. Soc. A*, *354*(1711), 1385–1410, doi:10.1098/rsta.1996.0054.
- Masters, G., G. Laske, H. Bolton, and A. M. Dziewonski (2000), *Earth's Deep Interior — Mineral Physics and Tomography From the Atomic to the Global Scale*, chap. The Relative Behavior of Shear Velocity, Bulk Sound Speed, and Compressional Velocity in the Mantle: Implications for Chemical and Thermal Structure, pp. 63–87, American Geophysical Union, Washington D.C.
- Matas, J., J. Bass, Y. Ricard, E. Mattern, and M. S. T. Bukowinski (2007), On the bulk composition of the lower mantle: predictions and limitations from generalized inversion of radial seismic profiles, *Geophys. J. Int.*, *170*, 764–780, doi:10.1111/j.1365-246X.2007.03454.x.
- Mattern, E., J. Matas, Y. Ricard, and J. Bass (2005), Lower mantle composition and temperature from mineral physics and thermodynamic modelling, *Geophys. J. Int.*, *160*(3), 973–990, doi:10.1111/j.1365-246X.2004.02549.x.
- Matyska, C., and D. A. Yuen (2000), Profiles of the Bullen parameter from mantle convection modelling, *Earth Planet. Sci. Lett.*, *178*(1–2), 39–46, doi:10.1016/S0012-821X(00)00060-1.
- McCaffrey, R. (2005), Block kinematics of the Pacific–North America plate boundary in the southwestern United States from inversion of GPS, seismological, and geologic data, *J. Geophys. Res.*, *110*(B7), B07,401, doi:10.1029/2004JB003307.
- McGill, S. F., M. E. Barley, J. E. Hams, K. Hobart, J. Ramirez, J. E. Fryxell, G. A. Lyzenga, and J. D. McGill (2003), Modeling of geodetic crustal motion velocities in southern California: Undergraduate research, *AGU Fall Meeting Abstracts*, pp. ED41B–1162.
- McKenzie, D., and M. J. Bickle (1988), The volume and composition of melt generated by extension of the lithosphere, *J. Petrology*, *29*(3), 625–679.
- McNamara, A., and S. Zhong (2005), Thermochemical structures beneath Africa and the Pacific Ocean, *Nature*, *437*, 1136–1139, doi:10.1038/nature04066.
- McNamara, A. K., and S. J. Zhong (2004), Thermochemical structures within a spherical mantle: Superplumes or piles?, *J. Geophys. Res.*, *109*(B7), B07,402, doi:10.1029/2003JB002847.
- McNamara, A. K., P. E. van Keken, and S. I. Karato (2002), Development of anisotropic structure in the earth's lower mantle by solid-state convection, *Nature*, *416*(6878), 310–314, doi:10.1038/416310a.
- Meade, B. J., and B. H. Hager (2005), Block models of crustal motion in southern

- California constrained by GPS measurements, *J. Geophys. Res.*, *110*(B3), B03,403, doi:10.1029/2004JB003209.
- Miller, M. M., D. J. Johnson, T. H. Dixon, and R. K. Dokka (2001), Refined kinematics of the eastern California shear zone from GPS observations, 1993–1998, *J. Geophys. Res.*, *106*(B2), 2245–2263, doi:10.1029/2000JB900328.
- Mitrovica, J. X. (1996), Haskell [1935] revisited, *J. Geophys. Res.*, *101*(B1), 555–569, doi:10.1029/95JB03208.
- Mittelstaedt, E., and P. J. Tackley (2006), Plume heat flow is much lower than cmb heat flow, *Earth Planet. Sci. Lett.*, *241*(1–2), 202–210, doi:10.1016/j.epsl.2005.10.012.
- Monnereau, M., and D. A. Yuen (2002), How flat is the lower-mantle temperature gradient?, *Earth Planet. Sci. Lett.*, *202*(1), 171–183, doi:10.1016/S0012-821X(02)00756-2.
- Montague, N. L., and L. H. Kellogg (2000), Numerical models of a dense layer at the base of the mantle and implications for the geodynamics of D”, *J. Geophys. Res.*, *105*(B5), 11,101–11,114.
- Montelli, R., G. Nolet, F. A. Dahlen, G. Masters, E. R. Engdahl, and S.-H. Hung (2004), Finite-frequency tomography reveals a variety of plumes in the mantle, *Science*, *303*(5656), 338–343, doi:10.1126/science.1092485.
- Montelli, R., G. Nolet, F. A. Dahlen, and G. Masters (2006), A catalogue of deep mantle plumes: New results from finite-frequency tomography, *Geochem. Geophys. Geosyst.*, *7*, Q11,007, doi:10.1029/2006GC001248.
- Mount, V. S., and J. Suppe (1987), State of stress near the San Andreas fault: Implications for wrench tectonics, *Geology*, *15*(12), 1143–1146, doi:10.1130/0091-7613(1987)15<1143:SOSNTS>2.0.CO;2.
- Murnaghan, F. (1951), *Finite Deformation of an Elastic Solid*, Wiley, New York.
- Müller, R., M. Sdrolias, C. Gaina, and W. Roest (2008), Age, spreading rates and spreading asymmetry of the world’s ocean crust, *Geochem. Geophys. Geosyst.*, *9*(4), doi:10.1029/2007GC001743.
- Müller, R. D., J.-Y. Royer, and L. A. Lawver (1993), Revised plate motions relative to the hotspots from combined Atlantic and Indian Ocean hotspot tracks, *Geology*, *21*(3), 275–278, doi:10.1130/0091-7613(1993)021<0275:RPMRTT>2.3.CO;2.
- Nakagawa, T., and P. J. Tackley (2004), Thermo-chemical structure in the mantle arising from a three-component convective system and implications for geochemistry, *Phys. Earth Planet. Inter.*, *146*(1–2), 125–138, doi:10.1016/j.pepi.2003.05.006.

- National Geophysical Data Center (2006), *Digital relief of the surface of the Earth*, Boulder, Colorado, national oceanic and atmospheric administration data announcement 88-MGG-02 ed.
- Ni, S., and D. V. Helmberger (2003), Further constraints on the African superplume structure, *Phys. Earth Planet. Inter.*, *140*(1–3), 243–251, doi:10.1016/j.pepi.2003.07.011.
- Ni, S. D., E. Tan, M. Gurnis, and D. V. Helmberger (2002), Sharp sides to the African superplume, *Science*, *296*, 1850–1852, doi:10.1126/science.1070698.
- Oeser, J., H. P. Bunge, and M. Mohr (2006), Cluster design in the earth sciences — Tethys, *High Performance Computing And Communications, Proceedings, 4208*, 31–40.
- O’Neill, C., D. Müller, and B. Steinberger (2005), On the uncertainties in hot spot reconstructions and the significance of moving hot spot reference frames, *Geochem. Geophys. Geosyst.*, *6*(4), Q04,003, doi:10.1029/2004GC000784.
- Paulson, A., S. J. Zhong, and J. Wahr (2007), Inference of mantle viscosity from GRACE and relative sea level data, *Geophys. J. Int.*, *171*(2), 497–508, doi:10.1111/j.1365-246X.2007.03556.x.
- Pekaje (2007), http://commons.wikimedia.org/wiki/File:Maxwell_diagram.svg.
- Piazzoni, A. S., G. Steinle-Neumann, H.-P. Bunge, and D. Dolejš (2007), A mineralogical model for density and elasticity of the Earth’s mantle, *Geochem. Geophys. Geosyst.*, *8*, doi:10.1029/2007GC001697.
- Plesch, A., et al. (2007), Community Fault Model (CFM) for southern California, *Bulletin of the Seismological Society of America*, *97*(6), 1793–1802, doi:10.1785/0120050211.
- Poirier, J. (1985), *Creep of Crystals*, Cambridge University Press, Cambridge, UK.
- Pollack, H. N., S. J. Hurter, and J. R. Johnson (1993), Heat flow from the Earth’s interior: Analysis of the global data set, *Rev. Geophys.*, *31*(3), 267–280, doi:10.1029/93RG01249.
- Presnall, D. C., and G. H. Gudfinnsson (2008), Origin of the oceanic lithosphere, *Journal Of Petrology*, *49*(4), 615–632, doi:10.1093/petrology/egm052.
- Provost, A.-S., and H. Houston (2003), Stress orientations in northern and central California: Evidence for the evolution of frictional strength along the San Andreas plate boundary system, *J. Geophys. Res.*, *108*(B3), 2175, doi:10.1029/2001JB001123.

- Reinecker, J., O. Heidbach, M. Tingay, B. Sperner, and M. Müller (2005), The 2005 release of the World Stress Map, <http://www.world-stress-map.org>.
- Resovsky, J., and J. Trampert (2003), Using probabilistic seismic tomography to test mantle velocity–density relationships, *Earth Planet. Sci. Lett.*, *215*(1–2), 121–134, doi:10.1016/S0012-821X(03)00436-9.
- Ricard, Y., E. Mattern, and J. Matas (2005), *Earth's Deep Mantle: Structure, Composition, and Evolution*, chap. Synthetic Tomographic Images of Slabs From Mineral Physics, pp. 285–302, American Geophysical Union.
- Richards, M. A., and D. C. Engebretson (1992), Large-scale mantle convection and the history of subduction, *Nature*, *355*(6359), 437–440, doi:10.1038/355437a0.
- Richards, M. A., W.-S. Yang, J. R. Baumgardner, and H.-P. Bunge (2001), Role of a low-viscosity zone in stabilizing plate tectonics: Implications for comparative terrestrial planetology, *Geochem. Geophys. Geosyst.*, *2*(8), doi:10.1029/2000GC000115.
- Ringwood, A. E. (1975), *Composition and Petrology of the Earth's Mantle*, McGraw–Hill Company, New York, bb55.
- Ritsema, J., and H. J. van Heijst (2000), Seismic imaging of structural heterogeneity in Earth's mantle: Evidence for large-scale mantle flow, *Science Progress*, *83*, 243–259.
- Ritsema, J., and H. J. van Heijst (2002), Constraints on the correlation of P- and S-wave velocity heterogeneity in the mantle from P, PP, PPP and PKPab traveltimes, *Geophys. J. Int.*, *149*(2), 482–489, doi:10.1046/j.1365-246X.2002.01631.x.
- Ritsema, J., H. J. van Heijst, and J. H. Woodhouse (1999), Complex shear velocity structure imaged beneath Africa and Iceland, *Science*, *286*, 1925–1928, doi:10.1126/science.286.5446.1925.
- Ritsema, J., H. J. van Heijst, and J. H. Woodhouse (2004), Global transition zone tomography, *J. Geophys. Res.*, *109*(B2), doi:10.1029/2003JB002610.
- Rivera, L., and H. Kanamori (2002), Spatial heterogeneity of tectonic stress and friction in the crust, *Geophys. Res. Lett.*, *29*(6), 1088, doi:10.1029/2001GL013803.
- Rutter, E., and K. Brodie (1991), Lithosphere rheology — a note of caution, *Journal of Structural Geology*, *13*(3), 363–367, doi:10.1016/0191-8141(91)90136-7.

- Savage, J. C. (1983), A dislocation model of strain accumulation and release at a subduction zone, *J. Geophys. Res.*, *88*(B6), 4984–4996, doi:10.1029/JB088iB06p04984.
- Schaber, K., H. P. Bunge, B. S. A. Schuberth, R. Malservisi, and A. Horbach (2009), Stability of the rotation axis in high-resolution mantle circulation models: Weak polar wander despite strong core heating, *Geochem. Geophys. Geosyst.*, *10*(11), Q11W04, doi:10.1029/2009GC002541.
- Scholz, C. H. (2000a), Evidence for a strong San Andreas fault, *Geology*, *28*(2), 163–166, doi:10.1130/0091-7613(2000)28<163:EFASSA>2.0.CO;2.
- Scholz, C. H. (2000b), A fault in the ‘weak San Andreas’ theory, *Nature*, *406*(6793), 234–234, doi:10.1038/35018740.
- Schuberth, B. S. A., H. P. Bunge, G. Steinle-Neumann, C. Moder, and J. Oeser (2009), Thermal versus elastic heterogeneity in high-resolution mantle circulation models with pyrolite composition: High plume excess temperatures in the lowermost mantle, *Geochem. Geophys. Geosyst.*, *10*(1), Q01W01, doi:10.1029/2008GC002235.
- Shen, Z., and D. Jackson (2005), Southern California tectonic deformation modeling, *Tech. rep.*, SCEC.
- Sigloch, K., N. McQuarrie, and G. Nolet (2008), Two-stage subduction history under North America inferred from multiple-frequency tomography, *Nature Geoscience*, doi:10.1038/ngeo231.
- Simmons, N. A., A. M. Forte, and S. P. Grand (2007), Thermochemical structure and dynamics of the African superplume, *Geophys. Res. Lett.*, *34*, L02,301, doi:10.1029/2006GL028009.
- Sleep, N. H. (1990), Hotspots and mantle plumes — some phenomenology, *J. Geophys. Res.*, *95*(B5), 6715–6736.
- Sleep, N. H. (2003), Simple features of mantle-wide convection and the interpretation of lower-mantle tomograms, *Comptes Rendus Geoscience*, *335*(1), 9–22, doi:10.1016/S1631-0713(03)00008-7.
- Southern Methodist University (2007), Regional geothermal database of U.S.
- Staudigel, H., K. H. Park, M. Pringle, J. L. Rubenstone, W. H. F. Smith, and A. Zindler (1991), The longevity of the South-Pacific isotopic and thermal anomaly, *Earth Planet. Sci. Lett.*, *102*(1), 24–44, doi:10.1016/0012-821X(91)90015-A.
- Stegman, D. R., M. A. Richards, and J. R. Baumgardner (2002), Effects of depth-dependent viscosity and plate motions on maintaining a relatively uniform mid-

- ocean ridge basalt reservoir in whole mantle flow, *J. Geophys. Res.*, *107*(B6), 2116, doi:10.1029/2001JB000192.
- Stein, C. A., and S. Stein (1992), A model for the global variation in oceanic depth and heat flow with lithospheric age, *Nature*, *359*, 123–129, doi:10.1038/359123a0.
- Steinberger, B. (2000), Slabs in the lower mantle - results of dynamic modelling compared with tomographic images and the geoid, *Phys. Earth Planet. Inter.*, *118*(3–4), 241–257, doi:10.1016/S0031-9201(99)00172-7.
- Stixrude, L., and C. Lithgow-Bertelloni (2005), Thermodynamics of mantle minerals — I. Physical properties, *Geophys. J. Int.*, *162*(2), 610–632, doi:10.1111/j.1365-246X.2005.02642.x.
- Stixrude, L., and C. Lithgow-Bertelloni (2007), Influence of phase transformations on lateral heterogeneity and dynamics in Earth's mantle, *Earth Planet. Sci. Lett.*, *263*, 45–55, doi:10.1016/j.epsl.2007.08.027.
- Su, W.-j., and A. M. Dziewonski (1997), Simultaneous inversion for 3-D variations in shear and bulk velocity in the mantle, *Phys. Earth Planet. Inter.*, *100*(1–4), 135–156, doi:10.1016/S0031-9201(96)03236-0.
- Suppe, J. (1981), Mechanics of mountain building and metamorphism in Taiwan, *Memoir of the Geological Society of China*, *4*, 67–89.
- Suppe, J. (2007), Absolute fault and crustal strength from wedge tapers, *Geology*, *35*(12), 1127–1130, doi:10.1130/G24053A.1.
- Tackley, P. J. (2000), Mantle convection and plate tectonics: Toward an integrated physical and chemical theory, *Science*, *288*(5473), 2002–2007, doi:10.1126/science.288.5473.2002.
- Tackley, P. J. (2002), Strong heterogeneity caused by deep mantle layering, *Geochem. Geophys. Geosyst.*, *3*, 1024, doi:10.1029/2001GC000167.
- Talagrand, O. (1997), Assimilation of observations, an introduction, *Journal Of The Meteorological Society Of Japan*, *75*(1B), 191–209.
- Tanikawa, W., and T. Shimamoto (2009), Frictional and transport properties of the Chelungpu fault from shallow borehole data and their correlation with seismic behavior during the 1999 Chi-Chi earthquake, *J. Geophys. Res.*, *114*(B1), B01,402, doi:10.1029/2008JB005750.
- Tapponnier, P., G. Peltzer, and R. Armijo (1986), On the mechanics of the collision between India and Asia, *Geological Society, London, Special Publications*, *19*(1), 113–157, doi:10.1144/GSL.SP.1986.019.01.07.
- Thatcher, W. (1995), Microplate versus continuum descriptions of active tectonic deformation, *J. Geophys. Res.*, *100*(B3), 3885–3894, doi:10.1029/94JB03064.

- Thatcher, W., and F. Pollitz (2008), Temporal evolution of continental lithospheric strength in actively deforming regions, *GSA Today*, 18, 4–11.
- Titus, S. J., C. DeMets, and B. Tikoff (2005), New slip rate estimates for the creeping segment of the San Andreas fault, California, *Geology*, 33(3), 205–208, doi:10.1130/G21107.1.
- Torsvik, T. H., R. D. Müller, R. van der Voo, B. Steinberger, and C. Gaina (2008), Global plate motion frames: Toward a unified model, *Rev. Geophys.*, 46, RG3004, doi:10.1029/2007RG000227.
- Townend, J., and M. D. Zoback (2004), Regional tectonic stress near the San Andreas fault in central and southern California, *Geophys. Res. Lett.*, 31(15), L15S11, doi:10.1029/2003GL018918.
- Trampert, J., F. Deschamps, J. Resovsky, and D. Yuen (2004), Probabilistic tomography maps chemical heterogeneities throughout the lower mantle, *Science*, 306(5697), 853–856, doi:10.1126/science.1101996.
- Tromp, J., C. Tape, and Q. Y. Liu (2005), Seismic tomography, adjoint methods, time reversal and banana–doughnut kernels, *Geophys. J. Int.*, 160(1), 195–216, doi:10.1111/j.1365-246X.2004.02453.x.
- Trompert, R., and U. Hansen (1998), Mantle convection simulations with rheologies that generate plate-like behaviour, *Nature*, 395(6703), 686–689.
- Urey, H. C. (1956), The cosmic abundances of potassium, uranium, and thorium and the heat balances of the earth, the moon, and mars, *Proceedings Of The National Academy Of Sciences Of The United States Of America*, 42(12), 889–891.
- U.S. Geological Survey (2006), Quaternary fault and fold database for the United States, <http://earthquake.usgs.gov/regional/>, accessed Oct. 2007.
- U.S. Geological Survey (2007), USGS heat flow database for California, <http://earthquake.usgs.gov/heatflow/>, accessed May 2007.
- van der Hilst, R. D., and H. Karason (1999), Compositional heterogeneity in the bottom 1000 kilometers of earth’s mantle: Toward a hybrid convection model, *Science*, 283(5409), 1885–1888, doi:10.1126/science.283.5409.1885.
- van der Hilst, R. D., S. Widiyantoro, and E. R. Engdahl (1997), Evidence for deep mantle circulation from global tomography, *Nature*, 386(6625), 578–584, doi:10.1038/386578a0.
- van der Hilst, R. D., M. V. de Hoop, P. Wang, S.-H. Shim, P. Ma, and L. Tenoerio (2007), Seismostratigraphy and thermal structure of Earth’s core-mantle boundary region, *Science*, 315(5820), 1813–1817, doi:10.1126/science.1137867.

- Wang, Y., and L. Wen (2004), Mapping the geometry and geographic distribution of a very low velocity province at the base of the earth's mantle, *J. Geophys. Res.*, *109*(B10), B10,305, doi:10.1029/2003JB002674.
- Wen, L. X., P. G. Silver, D. James, and R. Kuehnel (2001), Seismic evidence for a thermo-chemical boundary at the base of the Earth's mantle, *Earth Planet. Sci. Lett.*, *189*, 141–153, doi:10.1016/S0012-821X(01)00365-X.
- Wernicke, B. (1995), Low-angle normal faults and seismicity: A review, *J. Geophys. Res.*, *100*(B10), 20,159–20,174, doi:10.1029/95JB01911.
- Working Group on California Earthquake Probabilities (1999), Earthquake probabilities in the San Francisco Bay region: 2000 to 2030 — a summary of findings, *Tech. rep.*, U.S. Geological Survey, open file report 99-517.
- Zhong, S. J. (2006), Constraints on thermochemical convection of the mantle from plume heat flux, plume excess temperature, and upper mantle temperature, *J. Geophys. Res.*, *111*(B4), B04,409, doi:10.1029/2005JB003972.
- Zoback, M. (2000), Strength of the San Andreas, *Nature*, *405*(6782), 31–32, doi:10.1038/35011181.
- Zoback, M. D., et al. (1987), New evidence on the state of stress of the San Andreas fault system, *Science*, *238*(4830), 1105–1111, doi:10.1126/science.238.4830.1105.

B Schematic Program Flow of SHELLS

This is a verbal description of the neotectonic fault simulation program SHELLS (in the most current version from 2006-08-14). Although the source code of the program is publicly available and remarkably well commented and although some of its key concepts have been explained in several publications (*Bird*, 1989; *Bird and Kong*, 1994; *Kong and Bird*, 1995; *Bird*, 1998; *Bird and Liu*, 1999; *Bird et al.*, 2008), a detailed high-level description is missing. This description tries to bridge the gap between the sometimes very abstract descriptions of the key concepts in the publications and the low-level implementation. The level of indentation corresponds to the depth in the call graph.

- *subroutine GETNET*: The grid file is read; it contains the coordinates of the grid points, the triangular connectivity and the fault geometry. Additionally, there is for each grid point the topography, surface heat flow, thickness of the crust and thickness of the lithospheric mantle (and, if desired, density anomaly and cooling curvature), and for each fault element the dip angle (for both endpoints) and the amount of total slip.
- *subroutine READPM*: The input parameter file is read. It contains the fault friction coefficient, the Biot coefficient (giving the efficacy of pore fluid pressure), the five parameters for the power law describing dislocation creep (each parameter twice, for crust and mantle), slope and intercept of the upper mantle adiabat, plate reference frame, driving mechanism, several upper limits (basal traction, subduction zone traction, temperatures in crust and mantle), thermal parameters (surface temperature, thermal conductivity in crust/mantle, radioactive heat production rate in crust/mantle, thermal expansion coefficient in crust/mantle) and convergence criteria.
- *subroutine SQUARE*: Here, the grid geometry is checked.
 - If all grid points are connected to triangles or fault elements.
 - If the point pairs at the ends of the faults are at the same locations; if not, they are replaced by the average positions of all grid points closer than 10% of the fault length.

- If the area of all triangular grid elements (computed via *subroutine DERIV*) is positive — which is not the case for excessively distorted elements. (Additionally, several partial derivatives *DXS*, *DYS*, *DXSP*, *DYSP*, vector nodal functions *FPSFER* and colatitudes *SITA* are computed.)
 - The length of all fault elements is computed and stored.
 - For all triangle elements, the neighboring elements are determined; a neighbor is missing, the triangle element and the two nodes defining the affected side are marked as model boundaries.
 - If the grid has boundary nodes, it is checked whether they are all connected (by adjacent triangular elements, fault elements or duplicated nodes at faults) and form one closed loop.
 - The fault types of both ends of each fault and for all seven integration points on the fault are compared; they have to be all near vertical (allowing only strike-slip motion) or all shallower (allowing also oblique motion).
 - The azimuth of each fault is computed.
 - For near vertical faults: if there is a neighboring fault and if it is also near-vertical, then the azimuth of both faults are averaged.
- *subroutine GETPBX*: Reads the plate polygons (usually in the file *PB2002_plates.dig*).
 - *subroutine ASSIGN*: Determines for each grid point to which plate it belongs, by summing up the angles between the grid point and two successive plate polygon points (incl. a projection of the spherical surface onto a planar surface). If the sum is larger than 180° , the grid point is assumed to be inside that polygon. Points in fault elements are moved away from the fault trace (inside the continuum element that they belong to), so they end up in different plates if the fault is located on a plate boundary.
 - *subroutine TRACT*: If the driving mechanism (variable *ICONVE* in the input parameter file) is 6, read the traction file and assign the basal traction for every grid point; otherwise, set the tractions to zero. For certain plates with attached slabs (AU, CL, CO, IN, JF, NA, PA, PS, RI, SS), the basal traction of their grid points are also set to zero.
 - *subroutine DOWNER*: If the grid is global, it determines the grid nodes on subduction zones that require boundary conditions — on faults with a dip angle smaller than *SLIDE* and where the fault nodes are duplicated, the footwall node.

- *subroutine OLDVEL*: If there is a file with old velocity solutions, it is read, otherwise the velocities are initialized to zero.
- *subroutine READBC*: Reads a file with velocity boundary conditions for those nodes that are either model boundaries (determined by *subroutine SQUARE*) or have subducting slabs attached (determined by *subroutine DOWNER*, for global grids without boundaries). Depending on the type of boundary conditions, the velocities and directions are read from the file (*ICOND* 1, 2) or computed from the built-in Euler poles of the plates (*subroutine EULER*, for *ICOND* 5) or determined using *subroutine EDGEVS* (for *ICOND* 3 and 4).
 - *subroutine EDGEVS*: Computes the middle of the associated fault surface for every boundary node, reads the coordinates from the plate boundary file (usually *PB2002_boundaries.dig*) and determines the closest plate boundary point (global model: the one on the subducting plate, otherwise always the second plate). If the plate boundary is closer than 0.01 radians (approx. 0.5 degrees or 64 km) and the subducting plate is not the reference plate, the subduction velocity and direction is computed from the Euler pole of the plate.
- *subroutine SANDER*: For non-global models, the arguments of adjacent fault elements at the model boundary are averaged — but only if two consecutive boundary nodes are at the same position, if they are on two distinct strike-slip (i.e. near-vertical) faults and if their boundary conditions (*ICOND*) are equal and 2 or 4 or 5 and have the same velocity.
- *subroutine KSIZE*: Computes the bandwidth of the stiffness matrix. It starts with a diagonal matrix and determines then the band widening; for this, it traverses all continuum and all fault elements and determines for each node the furthest distance to other nodes in the same element to both sides of the main diagonal of the matrix. The largest distances of all nodes to the left and to the right of the main diagonal yield the lower and upper bandwidth of the stiffness matrix. Since there are two degrees of freedom per node (the two velocity components), the bandwidth has to be doubled. The total memory required for the stiffness matrix is two times the lower bandwidth plus the upper bandwidth plus one element.
- *subroutine FILLIN*: precomputes several arrays.
 - *subroutine CONVEC*: Computes the velocity field in the asthenosphere which creates basal drag via viscous coupling.
 - * *ICONVE* = 0: sets velocity field to zero
 - * *ICONVE* = 1: *Hager and O'Connell (1979)*; the velocity vectors (every 10°, from 10° E to 360° E and from -80° N to +80° N)

- are read from the file in *IUNITM* (usually *HOC79II.DIG*) and interpolated onto the velocity field of the finite element grid.
- * *ICONVE* = 2: *Baumgardner* (1988) Figure 7, parts A-F; the velocity vectors are read from the file in *IUNITM* (usually *BAUM887.DIG*) and for each grid point the closest velocity vector is chosen.
 - * *ICONVE* = 3, 4: The velocity field is computed from the built-in Euler vectors.
 - * *ICONVE* = 5: Polygons of the plate outlines at depth are read and the velocity field is computed from the corresponding Euler poles. Interestingly, a different algorithm to the one in the *subroutine ASSIGN* is used in order to determine if a point lies within a polygon.
- *subroutine FLOW*: Interpolates the nodal velocity field onto the seven integration points of a triangular continuum element.
 - *subroutine INTERP*: Interpolates a nodal scalar value onto the seven integration points of a triangular continuum element. This routine is used to interpolate:
 - * the elevation (*ELEV*)
 - * the heat flow (*DQDTDA*)
 - * the density anomaly (*density_anomaly*) and
 - * the vertical stress anomaly at the base of the plate (*SIGZZB*, see below)
 - * and its vertical integral (*TAUZZ*, see below).
 - The cooling curvature is not interpolated using *subroutine INTERP* since the nonlinearities are too great.
 - * Instead, the geotherm is computed (from surface heat flow, thermal conductivity and radiogenic heat), and the coefficients of the polynomial are stored in the arrays *GEOTHC* (crust) and *GEOTHM* (mantle).
 - * Then, the temperature at the base of the lithosphere is computed and compared with the temperature from the upper mantle adiabat in 100 km depth (computed from slope *GRADIE* and intercept *TADIAB* of the adiabat).
 - * From the difference a correction factor to the quadratic term of the geotherm (= the radiogenic heat production) is computed and included in the geotherms of crust and mantle.
 - *subroutine SQUEEZ*: Computes the vertical integral of the vertical stress anomaly, from the density anomaly, elevation and thickness of crust/mantle lithosphere.

- * First, a reference density and pressure profile is created. The density profile reaches from the surface down to a depth of 300 km (*NDREF*), in steps of 1 km; it assumes 2.7 km of ocean on top (= density of water), then 5 km crust (= density of crustal rock), and mantle rock below. The pressure profile is the lithostatic pressure of this density profile.
 - * Then, the plate is traversed vertically in steps of 1 km; in each step the densities at the top and at the bottom are determined (either computed from the average rock density *RHOBAR*, the thermal expansion coefficient *ALPHAT* and the temperature from the geotherm, and the given density anomaly *density_anomaly_kgpm3*; or, if the elevation is negative, the density of water for the part above).
 - * The differential pressures caused by the density difference within each step are added to the reference pressure profile (result: *SIGZZB*) and summed up vertically (result: *TAUZZ*).
 - * These two variables are finally interpolated on the seven integration points using *subroutine INTERP*, see above.
- *subroutine ONEBAR*:
- * Determines for all integration points in all continuum elements the shear stress required to create unit relative horizontal velocity across the depth of the model (= lithosphere + asthenosphere until depth *ZBASTH* specified in input parameter file)
 - * Lithosphere and asthenosphere are traversed in steps of one kilometer.
 - * In each depth layer, the geotherm temperature and the temperature of the upper mantle adiabat are determined; the smaller value is chosen, but at least 200 K.
 - * The velocity gradient due to dislocation creep within that layer is computed and summed up.
 - * The coupling coefficient *GLUE* is then the inverse of the total velocity to the power of *ECREEP*.
 - * If the driving mechanism *ICONVE* = 5 (see above), *GLUE* is set to a very large value, so the shear tractions end up to be the largest allowed values.
- The flag *PULLED* (indicating that there are horizontal shear tractions at the base of the plate) is set for all integration points in all continuum elements: If the driving mechanism *ICONVE* is 3, 4 or 6 (see above; i.e. mantle is neither static nor an external velocity field is used), it is set to true if the maximum traction *TRHMAX* (defined in

the parameter file) is nonzero. For $ICONVE = 5$ only if the temperature at the base of the lithosphere is below 1000 °C.

- *subroutine LIMITS*: Sums up the area of the triangles, computes the volume by summing up the triangle areas with the local lithosphere thickness and determines the average thickness, the typical width of the model, and several limits ($CONSTR$, $ETAMAX$, $FMUMAX$, $VISMAX$).
- *subroutine FIXED*: Precomputes the fixed part of the linear system.
 - The fixed part of the forcing vector $FBASE$ is initialized with the interpolated vertically-integrated topographic stress (if $DOFB1 = \text{true}$) and horizontal components of basal traction anomalies (if $DOFB2 = \text{true}$), weighted by the element area.
 - If $DOFB3 = \text{true}$: For boundary elements that are not ridges, additional vertical traction is added, as if the adjacent material had the same thickness, but zero strength. However, these forces are normally overwritten by velocity boundary conditions.
 - For all fault elements, the continuum elements on both sides of each fault element are determined, if existing.
 - Then, the average fault dip is computed and determined, to which side the fault dips.
 - If the current fault is on the grid boundary (i.e., no continuum element on that side), the average vertical integral of the vertical stress anomaly of the two fault nodes is taken.
 - Otherwise, a down-dip integration is performed; in each iteration, the *subroutine LOOKUP* is used to determine under which continuum element the current integration point on the fault plane is. Then, all relevant informations (elevation, heat flow, thickness of crust and lithospheric mantle, density anomaly) are interpolated from the nodes of the continuum element, the geotherm coefficients are computed, and all this is fed into *subroutine SQUEEZ*, see above, in order to compute the vertical integral of the vertical stress anomaly.
 - If $DOFB4 = \text{true}$: additional correction to $FBASE$
 - Torques due to lithostatic pressure anomaly in fault are added.
 - * *subroutine LOOKUP*: Searches for a point, given by coordinates X (longitude) and Y (colatitude), in all continuum elements, by comparing its coordinates with the coordinates of a test point in the center of the current continuum element. If the distance between the point and the test point is small, the internal coordinates of the test point are adjusted and compared again, otherwise a different continuum element is tested. The return values are the number

of the continuum element and the internal coordinates of the best test point inside this element.

- *subroutine PURE*: The actual simulation is performed here.
 - *subroutine EDOT*: Computes the strain rate for each integration point of each continuum element from the gradients of the velocities between the three grid nodes of the element.
 - The horizontal traction *SIGHB* on the base of the plate (2 components) and the vertical integral of the stress anomaly *TAUMAT* (3 components) are initialized to zero for every integration point of every continuum element.
 - *subroutine VISCOS*: Computes the linearized viscosity *ALPHA* and the prestress component *TOFSET* for all integration points of all continuum elements from strain rate tensor *ERATE* and the vertical integrals of the horizontal principle stresses *PT1* and *PT2*. If the strain rate is zero, use a default viscosity, derived from the maximum viscosity *VISMAX*. Furthermore, the scores that are printed at each iteration step are computed.
 - * *subroutine DIAMND*: Computes the vertical integrals of the horizontal principal stresses *PT1* and *PT2* for one layer of the lithosphere (crust or mantle) from the continuum friction coefficient *CFRIC* (= the friction coefficient for newly formed microfractures) and the creep parameters *xCREEP*. First, the brittle–ductile transition depth is determined (which depends on the stress direction in unfaulted material), and then the creeping part is numerically integrated, like in the *subroutine MOHR* for faults. The temperature needed for the creep law is derived from the heat flow as usual.
 - *subroutine TAUDEF*: Computes the vertical integral of stress anomalies for all integration points of all continuum elements; from strain rate *ERATE* and linearized viscosity *ALPHA*, plus a prestress component *TOFSET*.
 - The brittle–ductile transition depths are initialized to 1/6 of the thickness of the crust/mantle lithosphere, respectively.
 - *subroutine MOHR*: This subroutine computes the fault strength and writes it into the stiffness matrix.
 - * If the fault is near-vertical, the gradient of excess normal pressure width depth *DDPNDZ* is determined from the spreading rate *SPREAD* divided by the transition depth *ZTRANF* and constrained by the frictional limits *THRUST* and *NORMAL* given by

- the Mohr circle. For oblique faults, this gradient is set to zero.
- * For every integration point of every fault element, several auxiliary variables are computed (depths, temperatures, densities, lithostatic pressure gradient, slip rate etc.) and finally the brittle shear force gradient with depth *DSFDZ*.
 - * Then, the brittle–ductile transition depth is determined (both for crust and mantle lithosphere), using nested intervals: For the mean depth between the upper and lower end of the interval, the brittle shear force *SHEARF* (from shear force gradient *DSFDZ* and depth *Z*) and ductile shear force *SHEARC* (from temperature *T*, depth *Z* and creep constants *xCREEP*) are computed. Depending on which one is bigger, the upper or lower end of the interval is set to the current depth, and the process is repeated 15 times.
 - * Next, the shear force is integrated over depth; result = *FIMUDZ*.
 - The integral over the brittle part is simply 0.5 times the shear force at the transition depth *SHEART* times the transition depth *ZTRANS*. (Additional effort is necessary to limit the shear force to the maximum value rocks can support *DCREEP*.)
 - For the integration of the nonlinear dislocation creep part, the parabolic rule (Simpson’s rule) is used. The ductile part is divided into *NSTEP* intervals, for each one the shear force is computed in the middle *SCHALF* and at both ends *SCFULL* (from temperatures *THALF/TFULL*, depth *ZHALF/ZFULL* and creep constants *xCREEP*), multiplied with their respective weights, and summed up.
 - * The integrated shear traction is limited on subduction zones.
 - * For non-vertical faults, values are assigned to the stiffness matrix *FC* and the traction vector *FTSTAR*.
 - * The transition depth *ZTRANF* and the shear force there *FPEAKS* are saved only at the midpoints of faults.
- Then follows the main loop of the program, where the solution is iteratively approached. In each step, a velocity field is computed, using the viscosities and tractions derived from the previous velocity field. The loop ends when the differences to the previous step are sufficiently small (convergence criteria are specified in the input parameter file).
- * *subroutine THONB*: Computes the shear tractions *SIGHB* on the base of the plate.
 - The velocity difference between the plate and the basal velocity field is computed.

- The shear traction is the smallest of either *GLUE* (see above, *ONEBAR*) times the velocity difference to the power of *ECREEP*, or the velocity difference times the maximum coupling coefficient *ETAMAX* or the maximum shear traction *TRHMAX* — if the flag *PULLED* (see above, *ONEBAR*) is set; otherwise zero.
- If *ICONVE* is 6, i.e. the shear tractions *SIGHB* are given directly, only *ETA* is computed (shear traction divided by velocity difference).
- * *subroutine VISCOS*: see above
- * *subroutine MOHR*: see above
- * *subroutine FEM*: Performs the finite element method.

- *subroutine BUILDF*: Computes the forcing vector *FORCE* (or *F*).

First, the basal driving force *FBASE* is assigned to the vector. Then, the horizontal gradient of the vertical integral of pre-stress *TOFSET* is computed, multiplied by the element area and weight factor of the integration point, and summed up for all integration points of a continuum element and added to the force vector.

The same is done for the basal shear stresses, which are computed from the basal velocity field *OVB* and the viscosity *ETA*.

Finally, the initial traction *FTSTAR* of non-vertical faults is added in a similar way.

- *subroutine BUILDK*: Computes the stiffness matrix *STIFF* (or *K*). Basically, the viscosities *ALPHA* and *ETA* of the integration points are written into the stiffness matrix, weighted by the solid angle of the continuum element.
- *subroutine ADDFST*: Adds fault stiffness to the linear system. For near-vertical faults, the contribution to the stiffness matrix is computed from *FIMUDZ*, otherwise from *FC* and the dip angle.
- *subroutine VCBS*: Imposes the velocity boundary conditions. For all nodes that require boundary conditions, the velocity components (multiplied by the highest diagonal element of the stiffness matrix *TOPONE*) are assigned to the corresponding entry of the forcing vector *F*, and the corresponding elements of the stiffness matrix *K* are set to *TOPONE*. If the boundary condition type *ICOND* is such that only the velocity compo-

ment parallel to the velocity boundary condition should be affected, then *ROTOR* is used to rotate the entries of the affected node in the force vector and in the stiffness matrix such that they are parallel/perpendicular to the direction of the velocity boundary condition.

- *subroutine SOLVER*: Is a wrapper that calls the solver routine from the numerical library (e.g. LAPACK: *DGBSV*). The equation that is solved is $\mathbf{K} \mathbf{X} = \mathbf{F}$ (with the stiffness matrix \mathbf{K} and the forcing vector \mathbf{F}). The resulting velocity field X is written into F , so both K and F are destroyed in this subroutine. After the subroutine, the old velocity field is still in V , and the new one is in F .
- Scoring of the results: The differential velocity field DV of F and V is computed and the maximum value $SCOREA$ of its magnitude and the ratio $SCOREB$ of the sums of the differential and the absolute velocity fields are determined. (If $SCOREB$ is less than $OKTOQT$, the iteration is stopped and the simulation ends.)
- The new velocity field F is copied into V .
- *subroutine EDOT*: computes strain rate, see above
- *subroutine TAUDEF*: computes the vertical integral of stress anomalies, see above
- * Output of the iteration status: RMS velocity $VRMS$, $SCOREA$, $SCOREB$ and correlation with last iteration $DVCORR$.
- *subroutine BALANC*: Computes the balance of nodal forces; for a detailed explanation see appendix of *Bird et al.*, 2008. For this, the *subroutine FIXED* is used twice (with different settings in $DOFBx$) and then *subroutine FLOW*. The resulting force balance is written into a file.
- *subroutine RESULT*: Writes the results into the log file, velocities into the velocity file and tractions into the traction file.
 - Velocities: E/N component, magnitude, azimuth
 - Triangle properties: azimuth of velocity, horizontal strain rate components, isostatic uplift rate, vertical stress integrals, brittle–ductile transition depths in crust and mantle, magnitude and azimuth of basal shear stress
 - Fault properties: azimuth and plunge of slip, total (= oblique) slip rate, several slip rate components (horizontal, right lateral, perpendicular shortening), shear traction (peak value and down-dip integral), brittle–ductile transition depths (crust and mantle)

- Torque summaries for all plates: mantle drag, velocity boundary conditions, fault strength etc. (each as xyz components and magnitude/azimuth)

C Program Listings

C.1 Plate Polygons to TERRA Plate Maps



Listing C.1: Script that converts plate polygons to TERRA grid

```

1  #!/usr/bin/perl -wanl
2
3  # USAGE:
4  # $0 polygons.xy [nt] > cfile [3> paraviewfile.vtk]
5
6  use constant NT => ( $ARGV[-1] =~ /^[2468]|[1-9][0-9]*[02468]$/ ? pop( @ARGV ) : 256 );
   # number of grid subdivisions; default value = 256, or specified as second
   parameter on command line
7  use constant NR => NT / 2; # number of radial layers, usually NT/2
8  use constant PI => atan2(0, -1);
9
10 sub is_point_in_on_out_counter {
11     my @point = @_[0..1];
12     my $count_north = $_[2];
13     my $count_south = $_[3];
14     my @polygon = @_[4..$#_];
15     my $polypoints = scalar( @polygon );
16
17     my ($W, $E, $S, $N, $x_lat, $dlon, $lon, $lon1, $lon2);
18
19     # re-set number of crossings
20     $$count_south = 0;
21     $$count_north = 0;
22
23     # Compute meridian through P and count all the crossings with
24     # segments of polygon boundary
25
26     for( my $i = 0; $i <= $#polygon; $i++ ) {
27         @v1 = @{$polygon[$i]};
28         @v2 = @{$polygon[($i + 1) % $polypoints]};
29
30         # Copy the two vertex longitudes since we need to mess with them
31         $lon1 = $v1[0];
32         $lon2 = $v2[0];
33
34         $dlon = $lon2 - $lon1;
35
36         # Jumped across Greenwich going westward or eastward
37         ( ( $dlon > 180.0 ) and $lon2 -= 360.0 ) or ( ( $dlon < -180.0 ) and $lon1 -=
           360.0 );

```

```

38
39 # set lon limits for this segment
40 if ($lon1 <= $lon2) {
41     # segment goes W to E (or N-S)
42     $W = $lon1;
43     $E = $lon2;
44 } else {
45     # segment goes E to W
46     $W = $lon2;
47     $E = $lon1;
48 }
49
50 # Local copy of longitude
51 $lon = $point[0];
52
53 # Make sure we rewind way west for starters
54 $lon -= 360.0 while ($lon > $W);
55
56 # Then make sure we wind to inside the lon range or way east
57 $lon += 360.0 while ($lon < $W);
58
59 # Not crossing this segment
60 next if ($lon > $E); # to next vertex
61
62 # Special case of N-S segment: does P lie on it?
63 if ($dlon == 0.0) {
64     if ( $v2[1] < $v1[1] ) {
65         # Get N and S limits for segment
66         $S = $v2[1];
67         $N = $v1[1];
68     } else {
69         $N = $v2[1];
70         $S = $v1[1];
71     }
72
73     # P is not on this segment
74     next if ( $point[1] < $S || $point[1] > $N ); # to next vertex
75
76     # P is on segment boundary; we are done
77     return (1);
78 }
79
80 # Calculate latitude at intersection
81 $x_lat = $v1[1] + ( ($v2[1] - $v1[1]) / ($lon2 - $lon1) ) * ($lon - $lon1);
82
83 # P is on S boundary
84 return 1 if ( $x_lat == $point[1] );
85
86 # Only allow cutting a vertex at end of a segment
87 # to avoid duplicates
88 next if ($lon == $lon1);
89
90 # Is cut is north or south of P?
91 ($x_lat > $point[1]) and ++$$count_north or ++$$count_south;
92
93 } # end of loop over vertices
94
95 return (0);
96 }
97
98 sub rad2deg {
99     return ($_[0] * 180 / PI);

```

```

100 }
101
102 sub acos {
103     return atan2( sqrt(1 - $_[0] * $_[0]), $_[0] );
104 }
105
106 sub grdgen {
107     my $a = 2 * acos( 1 / (2 * sin( PI / 5 ) ) );
108     my $lvt = int( 1.45 * log( NT ) );
109     my @ip = ( -1, 1, 3, 5, -3, 0, 2, 4, -4, -2 );
110
111     for( my $diamond = 0; $diamond < $nd; $diamond++ ) {
112         my $sgn = (4.5 - $diamond <=> 0); # upper or lower hemisphere
113         my $phi = $ip[$diamond] * PI / 5; # longitude shift
114
115         # coordinates of the four corners of the diamond
116         # first corner: pole (e.g. N)
117         # second corner: south east of N pole
118         # third corner: south west of N pole
119         # fourth corner: south of N pole
120         $xg[$diamond][0][0][0] = 0;
121         $xg[$diamond][0][0][1] = 0;
122         $xg[$diamond][0][0][2] = $sgn;
123
124         $xg[$diamond][NT][0][0] = sin( $a ) * cos( $phi + 2 * PI / 5 );
125         $xg[$diamond][NT][0][1] = sin( $a ) * sin( $phi + 2 * PI / 5 );
126         $xg[$diamond][NT][0][2] = cos( $a ) * $sgn;
127
128         $xg[$diamond][0][NT][0] = sin( $a ) * cos( $phi );
129         $xg[$diamond][0][NT][1] = sin( $a ) * sin( $phi );
130         $xg[$diamond][0][NT][2] = cos( $a ) * $sgn;
131
132         $xg[$diamond][NT][NT][0] = sin( $a ) * cos( $phi + PI / 5 );
133         $xg[$diamond][NT][NT][1] = sin( $a ) * sin( $phi + PI / 5 );
134         $xg[$diamond][NT][NT][2] = -cos( $a ) * $sgn;
135
136         # the diamond is iteratively subdivided
137         # i1 direction: from pole to point xv[1] = row
138         # i2 direction: from pole to point xv[2] = column
139         # diagonal: between xv[1] and xv[2] = horizontal diagonal
140         for( my $k = 0; $k < $lvt; $k++ )
141         {
142             my $m = 2**$k;
143             my $l = NT / $m;
144
145             # rows of diamond
146             for( my $j1 = 0; $j1 <= $m; $j1++ ) {
147                 for( my $j2 = 0; $j2 < $m; $j2++ ) {
148                     my $i1 = $j1 * $l;
149                     my $i2 = $j2 * $l + $l / 2;
150
151                     # for x, y, z coordinates: interpolate from previous grid resolution
152                     $xg[$diamond][$i1][$i2][$_] = $xg[$diamond][$i1][$i2 - $l / 2][$_] + $xg
153                         [$diamond][$i1][$i2 + $l / 2][$_] for( 0..2 );
154
155                     # compute radius of new grid point
156                     my $xnorm = 1 / sqrt( $xg[$diamond][$i1][$i2][0]**2 + $xg[$diamond][$i1
157                         ][$i2][1]**2 + $xg[$diamond][$i1][$i2][2]**2 );
158
159                     # project back onto sphere
160                     $xg[$diamond][$i1][$i2][$_] *= $xnorm for( 0..2 );
161                 }
162             }
163         }
164     }
165 }

```

```

160     }
161
162     # columns of diamond
163     for( my $j1 = 0; $j1 <= $m; $j1++ ) {
164         for( my $j2 = 0; $j2 < $m; $j2++ ) {
165             my $i1 = $j2 * $l + $l / 2;
166             my $i2 = $j1 * $l;
167
168             # for x, y, z coordinates: interpolate from previous grid resolution
169             $xg[$diamond][$i1][$i2][$_] = $xg[$diamond][$i1 - $l / 2][$i2][$_] + $xg[
170                 [$diamond][$i1 + $l / 2][$i2][$_] for( 0..2 );
171
172             # compute radius of new grid point
173             my $xnorm = 1 / sqrt( $xg[$diamond][$i1][$i2][0]**2 + $xg[$diamond][$i1
174                 ][$i2][1]**2 + $xg[$diamond][$i1][$i2][2]**2 );
175
176             # project back onto sphere
177             $xg[$diamond][$i1][$i2][$_] *= $xnorm for( 0..2 );
178         }
179     }
180
181     # diagonals of diamond
182     for( my $j1 = 0; $j1 < $m; $j1++ ) {
183         for( my $j2 = 0; $j2 < $m; $j2++ ) {
184             my $i1 = $j1 * $l + $l / 2;
185             my $i2 = $j2 * $l + $l / 2;
186
187             # for x, y, z coordinates: interpolate from previous grid resolution
188             $xg[$diamond][$i1][$i2][$_] = $xg[$diamond][$i1 - $l / 2][$i2 + $l / 2][
189                 $_] + $xg[$diamond][$i1 + $l / 2][$i2 - $l / 2][$_] for( 0..2 );
190
191             # compute radius of new grid point
192             my $xnorm = 1 / sqrt( $xg[$diamond][$i1][$i2][0]**2 + $xg[$diamond][$i1
193                 ][$i2][1]**2 + $xg[$diamond][$i1][$i2][2]**2 );
194
195             # project back onto sphere
196             $xg[$diamond][$i1][$i2][$_] *= $xnorm for( 0..2 );
197         }
198     }
199 }
200
201 # adjusts the minimum or maximum value if the given value is below or above
202 sub minmax {
203     ( ( $_[2] < $_[0] ) and ( $_[0] = $_[2] ) ) or ( ( $_[2] > $_[1] ) and ( $_[1] = $_[
204         2] ) );
205 }
206
207 # read polygons; new plate: extract id
208 if (/^> /) {
209     $current_plate = ( /;.+?_(\d{3})_ / )[0]; # behind first semicolon: three digits
210     # between underscores, then space
211     $bbox{$current_plate}->{'minlat'} = 90;
212     $bbox{$current_plate}->{'maxlat'} = -90;
213     $bbox{$current_plate}->{'minlon'} = 180;
214     $bbox{$current_plate}->{'maxlon'} = -180;
215     $bbox{$current_plate}->{'pole'} = 0;
216     $bbox{$current_plate}->{'lonsum'} = 0;
217     undef $prev_lon;
218 }
219
220 # coordinates: store them in array, determine min/max

```

```

216 elseif( $#F == 1 ) {
217     push( @{ $polygons{$current_plate} }, [ $F[0], $F[1] ] );
218
219     minmax( $bbox{$current_plate}->'minlat', $bbox{$current_plate}->'maxlat', $F[1]
220         );
221     minmax( $bbox{$current_plate}->'minlon', $bbox{$current_plate}->'maxlon', $F[0]
222         );
223     # we know that first and last point in the polygon is identical
224     if( defined( $prev_lon ) ) {
225         $dlon = $prev_lon - $F[0];
226
227         $dlon = abs( 360.0 - abs( $dlon ) ) * ( -$dlon <=> 0 ) if( abs( $dlon ) > 180.0 );
228
229         $bbox{$current_plate}->'lonsum' += $dlon;
230     }
231     $prev_lon = $F[0];
232 }
233 END {
234     $point = 0;
235     $plate = 0;
236     $nd = 10; # number of diamonds
237
238     print STDERR "polygons read";
239     $numberofgridpoints = (NT + 1)**2 * $nd;
240
241     # determine if the platepolygon contains the pole
242     ( abs( abs( $bbox{$_}->'lonsum' ) ) - 360 ) < 1.0e-8 ) and $bbox{$_}->'pole' = ( (
243         abs( $bbox{$_}->'maxlat' ) > abs( $bbox{$_}->'minlat' ) ) ) ? ( $bbox{$_}->{
244             'maxlat' } <=> 0 ) : ( $bbox{$_}->'minlat' } <=> 0 ) ) for ( keys %polygons );
245
246     # write TERRA header
247
248     # first: grid resolution (radial layers, diamond subdivisions)
249     printf( "%5d%5d\n", NR, NT );
250
251     # four lines of comment, for the case name
252     print "comment 1";
253     print "comment 2";
254     print "comment 3";
255     print "comment 4";
256
257     # radial layer depth
258     printf( "%15.8E%s", 0, ( $_ % 10 ? "" : "\n" ) ) for( 1..(NT / 2 + 1) );
259
260     print "";
261
262     # property array
263     printf( "%15.8E%s", 0, ( $_ % 10 ? "" : "\n" ) ) for( 1..20 );
264
265     # generate grid
266     grdgen();
267     print STDERR "grid generated";
268
269     # open Paraview output, write header
270     open( PARAVIEW, ">&3" ) or open( PARAVIEW, ">", "/dev/null" );
271     print PARAVIEW "# vtk DataFile Version 3.0";
272     print PARAVIEW "TERRA plate map";
273     print PARAVIEW "ASCII";
274     print PARAVIEW "DATASET POLYDATA";
275     print PARAVIEW "POINTS $numberofgridpoints float";

```

```

274
275 # write paraview grid
276 for( my $diamond = 0; $diamond < $nd; $diamond++ ) {
277     for( my $i = 0; $i <= NT; $i++ ) {
278         for( my $j = 0; $j <= NT; $j++ ) {
279             print PARAVIEW "@{$xg[$diamond][$i][$j]}";
280         }
281     }
282 }
283
284 # write connectivity
285 print PARAVIEW "POLYGONS " . (10 * NT**2 * 2) . " " . (4 * (10 * NT**2 * 2));
286 for( my $diamond = 0; $diamond < $nd; $diamond++ ) {
287     for( my $i = 0; $i < NT; $i++ ) {
288         for( my $j = 0; $j < NT; $j++ ) {
289             local $, = " ";
290             my $offset = $diamond * (NT + 1)**2 + $i * (NT + 1) + $j;
291             print PARAVIEW 3, $offset, $offset + 1, $offset + (NT + 1);
292             print PARAVIEW 3, $offset + 1, $offset + (NT + 1) + 1, $offset + (NT + 1);
293         }
294     }
295 }
296 print PARAVIEW "POINT_DATA $numberofgridpoints";
297 print PARAVIEW "SCALARS plate_id float";
298 print PARAVIEW "LOOKUP_TABLE default";
299
300 # do the actual work: assign plate ids to grid points
301 for( my $diamond = 0; $diamond < $nd; $diamond++ ) {
302     for( my $i = 0; $i <= NT; $i++ ) {
303         for( my $j = 0; $j <= NT; $j++ ) {
304             my $lon = rad2deg( atan2( $xg[$diamond][$i][$j][1], $xg[$diamond][$i][$j]
305                 ][0] ) );
306             my $length = sqrt( $xg[$diamond][$i][$j][0]**2 + $xg[$diamond][$i][$j]
307                 ][1]**2 );
308             my $lat = rad2deg( atan2( ( $length ), ( $xg[$diamond][$i][$j][2] ) ) );
309             $lat += 180 if( $lat < 0 );
310             $lat = 90 - $lat;
311
312             $prev_plate = $plate;
313             $plate = 0; # not found
314
315             # test all plates; first: the one of the previous grid point; then: plates
316             # with few polygon points first, so the expensive tests with many
317             # polygon points can be avoided if possible
318             for $current_plate ( sort { $a == $prev_plate ? -1 : $b == $prev_plate ? +1
319                 : scalar(@{$polygons{$a}}) <=> scalar(@{$polygons{$b}}) } keys %
320                 polygons ) {
321                 #counters for the number of crossings of a meridian through p and and
322                 # the segments of this polygon
323                 my $count_north = 0;
324                 my $count_south = 0;
325
326                 if( $bbox{$current_plate}->{'pole'} ) {
327                     # N polar cap
328                     if( $bbox{$current_plate}->{'pole'} == 1 ) {
329                         # South of a N polar cap
330                         next if( $lat < $bbox{$current_plate}->{'minlat'} );
331
332                         # Clearly inside of a N polar cap
333                         $plate = $current_plate and last if( $lat > $bbox{$current_plate}
334                             ->{'maxlat'} );
335                     }
336                 }
337             }
338         }
339     }
340 }

```

```

328
329     # S polar cap
330     if( $bbox{$current_plate}->{'pole'} == -1 ) {
331         # North of a S polar cap
332         next if( $lat > $bbox{$current_plate}->{'maxlat'} );
333
334         # North of a S polar cap
335         $plate = $current_plate and last if( $lat < $bbox{$current_plate
336             }->{'minlat'} );
337     }
338
339     # Tally up number of intersections between polygon
340     # and meridian through p
341
342     $plate = $current_plate and last if( is_point_in_on_out_counter( $lon
343         , $lat, $count_north, $count_south, @{$polygons{$current_plate
344             }}) ); # Found P is on S; return (POINT_ON_POLYGON);
345
346     $plate = $current_plate and last if( $bbox{$current_plate}->{'pole'}
347         == 1 and $count_north % 2 == 0);
348
349     $plate = $current_plate and last if( $bbox{$current_plate}->{'pole'}
350         == -1 and $count_south % 2 == 0);
351
352     next;
353 }
354
355     # First check latitude range
356     next if( $lat < $bbox{$current_plate}->{'minlat'} or $lat > $bbox{
357         $current_plate}->{'maxlat'} );
358
359     # Longitudes are trickier and are tested with the tallying of
360     # intersections
361
362     $plate = $current_plate and last if( is_point_in_on_out_counter( $lon,
363         $lat, $count_north, $count_south, @{$polygons{$current_plate}}) );
364     # Found P is on S; return (POINT_ON_POLYGON);
365     $plate = $current_plate and last if( $count_north % 2 ); # point
366     # inside polygon
367
368     # Nothing triggered the tests; we are outside
369 }
370
371     $plate = $prev_plate unless( $plate ); # use previous plate id if none
372     # has been found
373
374     printf( "%10.3f%s", $plate, (++$point % 15 ? " " : "\n") );
375     print PARAVIEW $plate;
376
377     # print progress in percent on STDERR
378     print STDERR int( $point / $numberofgridpoints * 100 + 0.5) . "% " unless(
379         $point % ($numberofgridpoints / 100) );
380 }
381 }

```

C.2 Wrapper Script



Listing C.2: Wrapper script that starts the above script C.1 in parallel (one instance per CPU) and remaps the plate IDs in both the plate maps and in the Euler pole file. Entries in the Euler pole file which do not correspond to closed plate polygons are omitted.

```

1  #!/bin/bash
2
3  # CONFIGURATION
4  POLYGONPATH="platepolygons/."
5  PLATE_BORDER_WIDTH=2  # width of the border zone (in grid points) where the velocity
   is reduced
6  NT=256  # TERRA grid resolution
7  TOTAL_TIME=250  # in Ma; if no polygons are available, the last plate configuration is
   used for the remaining time
8  DUMP_INTERVAL=10  # write dump after this many time steps
9  CFILE_PATH="platemaps/"
10 EULER_POLE_PATH="$CFILE_PATH"
11 VTK_BASENAME="visualized-platemap"  # specify file name root ("_time.vtk" will be
   added) or leave empty if no VTK output desired
12
13
14 # OTHER VARIABLES
15 PLATE_IDS=`mktemp`
16 PROCESSORS=`grep '^processor' /proc/cpuinfo | wc -l`
17 TOTAL_NUMBER_OF_PLATES=$(perl -wnle '/(> [^;]+;.+?_(\d{3})_ /) and $c{$1} = 1; }{
   print for( sort keys %c );' "$POLYGONPATH"/Polygons.platepolygons.*.xy | tee "
   $PLATE_IDS" | wc -l)
18 PARAMS=$(ls "$POLYGONPATH"/Polygons.platepolygons.*.xy | sed -e 's/^.*/Polygons\
   .platepolygons\.([0-9]\+)\.*/\1/' | sort -n | sed -n -e '1p; ${ p; =;}')
19 START_TIME=${PARAMS[0]}  # age of the youngest polygon in Ma
20 END_TIME=${PARAMS[1]}  # age of the oldest polygon in Ma
21 NUMBER_TIMESTEPS=${PARAMS[2]}  # number of polygon time steps
22 TIMESTEP=$((($END_TIME - $START_TIME) * 1000000 / ($NUMBER_TIMESTEPS - 1))  #
   interval between two polygons in years
23
24 function clean_up {
25     rm -f "$PLATE_IDS"
26     exit
27 }
28
29 trap clean_up SIGHUP SIGINT SIGTERM
30
31 # write header
32 echo -e "$NUMBER_TIMESTEPS\t$total_time\t$START_TIME\t(($END_TIME * $TIMESTEP))\
   \t$total_number_of_plates\t4.1\t$PLATE_BORDER_WIDTH" > "$EULER_POLE_PATH/
   euler_poles.dat"
33
34 IFS=$'\n'
35
36 {
37
38 for i in $(ls "$POLYGONPATH"/equivalent_stage_rotation_tab_*.csv | sed -e 's/^.*/
   equivalent_stage_rotation_tab\_([0-9.]\+)\.csv/\1/' | sort -n); do
39     echo "Processing time step $i" >&2

```

```

40
41 VTK_FILE=${VTK_BASENAME:+"${VTK_BASENAME}_$i.vtk"}
42 CFILE="$CFILE_PATH/cstage.mt$(printf '%04d' $NT).$(printf '%03d' ${i/.*/})"
43
44 # Does an output file with the right resolution exist? Then use it, and create only
45 # the Euler pole file.
46 if [ -s "$CFILE" ] && sed -e "1{/ $NT\$/Q;Q 1}" < "$CFILE" ; then
47     INPUT_CFILE="$CFILE"
48     OUTPUT_CFILE="/dev/null"
49 else
50     INPUT_CFILE=""
51     OUTPUT_CFILE="$CFILE"
52 fi
53
54 ( {
55     { if [ -z "$INPUT_CFILE" ] ; then
56         "$(cd "$(dirname "$0")"; pwd)/findplate_xy_gplates_generate-grid.pl "
57         $POLYGONPATH"/Polygons.platepolygons.${i/.00/}.*xy $NT 2> "/dev/null" 3>
58         "${VTK_FILE:=}/dev/null)"
59     else
60         cat "$INPUT_CFILE"
61     fi; } |
62
63     perl -anle '
64     use POSIX fmod;
65
66     $" = "\t";
67
68     $b = 6370e5 / 1e6; # rad/year to cm/Ma
69
70     if( $f == 2 ) # are we in the rotations file?
71     {
72         if( $x++ ) # are we after the first line?
73         {
74             # remap plate ids, calculate velocities
75             if( $n[$M[$F[0]]] )
76             {
77                 $output[$i++] = join( "\t", ( $age, ($i + 1), $M[$F[0]], $F[1] * $F[4]
78                 * $b, $F[2] * $F[4] * $b, $F[3] * $F[4] * $b, $F[0] ) );
79             }
80         }
81     }
82     elsif( $f == 1 ) # in the second file (plate map file): compute header length,
83     # map lines after header
84     {
85         $h ||= 8 + int( $F[1] / 20 ); # compute header length
86
87         if( $. > $h ) # remap plate ids
88         {
89             print map { $n[$m[int]++] sprintf( "%10.3f", $m[int] ); } @F; # if the
90             # line number is above $h (header length), record all ids in the array
91             @n
92         }
93         else # print header
94         {
95             print;
96         }
97     }
98 }

```

```

94     }
95     else # in the first file (plate_ids.txt)
96     {
97         $M[$_] = $.; # remapping for rotation files: plate ids to sequential numbers
98         $m[ ("'"$INPUT_CFILE"' " ? $. : $_) ] = $.; # remapping for plate maps:
99             depending on if they are already remapped
100     }
101     eof and ($. = 0, $f++); # end of file: count $f up, reset line counter
102
103     }{
104
105     print STDERR "$age\t0\t$age\t"$TIMESTEP"\t" . scalar( @output ) . "\t" . ( fmod
106         ( $age, "$DUMP_INTERVAL" ) == 0 ? 1 : 0 );
107     print STDERR join( "\n", @output );
108     ' "$PLATE_IDS" - "$POLYGONPATH"/equivalent_stage_rotation_tab_$i.csv 2>&1 > "
109         $OUTPUT_CFILE"; } & )
110
111     # wait if there are enough processes running
112     while( [ $(ps ux | grep '[f]indplate_xy_gplates' | wc -l) -ge $PROCESSORS ] ); do
113         sleep 5; done
114
115     done
116
117     # wait for the remaining processes to finish
118     while( [ $(ps ux | grep '[f]indplate_xy_gplates' | wc -l) -gt 0 ] ); do sleep 5; done
119
120     # sort Euler pole output and remove first columns used for sorting
121     } | sort -k1n -k2n | cut -f1,2 --complement >> "$EULER_POLE_PATH/euler_poles.dat"
122
123     # remove temporary files
124     clean_up

```